IMPROVING MULTIPLE SURFACE RANGE ESTIMATION OF A 3-DIMENSIONAL FLASH LADAR IN THE PRESENCE OF ATMOSPHERIC TURBULENCE

DISSERTATION

Brian J. Neff, Major, USAF

AFIT-ENG-DS-13-J-01

DEPARTMENT OF THE AIR FORCE
AIR UNIVERSITY

AIR FORCE INSTITUTE OF TECHNOLOGY

Wright-Patterson Air Force Base, Ohio

AFIT-ENG-DS-13-J-01

IMPROVING MULTIPLE SURFACE RANGE ESTIMATION OF A

3-DIMENSIONAL FLASH LADAR IN THE PRESENCE OF ATMOSPHERIC

TURBULENCE

DISSERTATION

Presented to the Faculty

Graduate School of Engineering and Management

Air Force Institute of Technology

Air University

Air Education and Training Command

in Partial Fulfillment of the Requirements for the

Degree of Doctor of Philosophy

Brian J. Neff, BS, MS

Major, USAF

June 2013

AFIT-ENG-DS-13-J-01

IMPROVING MULTIPLE SURFACE RANGE ESTIMATION OF A 3-DIMENSIONAL FLASH LADAR IN THE PRESENCE OF ATMOSPHERIC TURBULENCE

Brian J. Neff, BS, MS
Major, USAF

Approved:

//signed//	March 28, 2013
Stephen C. Cain, PhD (Chairman)	Date
//signed//	March 28, 2013
Richard K. Martin, PhD (Member)	Date
//signed//	March 28, 2013
Christine M. Schubert Kabban, PhD (Member)	Date
//signed//	April 9, 2013
Lt Col Timothy R. Jorris, PhD (Member)	Date

Accepted:

//signed//	May 2, 2013
Heidi R. Ries, PhD Interim Dean, Graduate School of Engineering and Management	Date

AFIT-ENG-DS-13-J-01

Abstract

Laser Radar sensors can be designed to provide two-dimensional (2-D) and three-dimensional (3-D) images of a scene from a single laser pulse. Currently, there are various data recording and presentation techniques being developed for 3-D sensors. While the technology is still being proven, many applications are being explored and suggested. As technological advancements are coupled with enhanced signal processing algorithms, it is possible that this technology will present exciting new military capabilities for sensor designers and end users.

The goal of this work is to develop an algorithm to enhance the utility of 3-D Laser Radar sensors through accurate ranging to multiple surfaces per image pixel while minimizing the effects of diffraction. Via a new 3-D blind deconvolution algorithm, it will be possible to realize numerous enhancements over both traditional Gaussian mixture modeling and single surface range estimation. While traditional Gaussian mixture modeling can effectively model the received pulse, we know that its shape is likely altered due to optical aberrations from the imaging system and the medium through which it is imaging. Simulation examples show that the multi-surface ranging algorithm derived in this work improves range estimation over standard Gaussian mixture modeling and frame-by-frame deconvolution by up to 89% and 85% respectively.

For my wife and children. Your support is what made this endeavor possible.

Acknowledgments

I would like to express my sincere appreciation for my advisor, Dr. Stephen Cain, for the advice and guidance you have offered during this program. Our first meeting was truly impromptu, but lasted nearly two hours where we discussed a myriad of potential research ideas. You always offered me complete latitude to explore topics of interest and your command of this body of knowledge has always been an inspiration to keep me on task.

I am also thankful for the diversity of expertise within my research committee. Each of you provided me unique tools to succeed, and instilled a level of understanding I previously could not have imagined.

Brian J. Neff

Table of Contents

List of Figures

List of Tables

List of Abbreviations

IMPROVING MULTIPLE SURFACE RANGE ESTIMATION OF A
3-DIMENSIONAL FLASH LADAR IN THE PRESENCE OF ATMOSPHERIC
TURBULENCE

I. Introduction

Three dimensional FLASH LAser Detection and Ranging (LADAR) sensors are
a special class of LIght Detection and Ranging (LIDAR) sensors that are able to
provide precise range measurements for every pixel in an imaged scene. Interest in
Three-Dimensional (3-D) FLASH LADAR systems is increasing for both military
and civilian applications over the more traditional scanning LADAR system. This
increase in popularity is due to the fact that 3-D FLASH LADAR systems can obtain
an entire 3-D image or data cube with a single laser pulse. In an ideal environment,
the spatial resolution that this class of sensors can achieve is limited only by the ability
to design and manufacture components with precision. However, in an operational
environment, the images may be distorted not only by system limitations, but also
by the atmosphere through which the light must pass.

1.1   Motivation

The motivation for this research initially stemmed from an inquiry from the De-
partment of Homeland Security (DHS) about imaging through obscurations. Current
state-of-the-art tactical sensors such as the AN/AAQ 33 - SNIPER targeting pod
shown in Figure 1.1, rely on passive target illumination. While this type of illumi-
nation has many inherent advantages, it does introduce several limitations as well.
Like all passive Electro Optical / Infra-Red (EO/IR) sensors, SNIPER suffers from

Figure 1.1: AN/AAQ 33 - SNIPER targeting pod integrated onto the B-1B.

thermal-crossover associated with the natural heating and cooling of the earth's surface. Further, EO/IR sensors rely on the addition of an active illumination designator to perform ranging to a target. In addition to tactical sensors, a study produced by Forecast International in 2011 estimated that nearly $17 billion dollars will be spent on new remote sensing satellite technology between 2012 and 2021 [1]. LADAR technology is one of the relatively new imaging technologies that will likely be employed on the next generation of remote sensing satellite platforms.

The aforementioned are just a sampling of the justification for employing 3-D LADAR technology on future generation remote sensors. Unfortunately, due to constraints such as low spatial resolution and limits on laser power, the current state of FLASH LADAR technology would yield limited, if any improvement in total capability over the currently fielded passive sensors. However, it may be possible to develop algorithms that limit the negative impacts of the operational environment and couple them with technological advances in sensor resolution and sensitivity to yield vast improvements in future imaging/targeting sensors.

Due to the employment of active illumination, 3-D FLASH LADAR sensors can gather ranging information for every point within a targeted scene nearly simulta-

neously. Further, depending on the detection methodology employed, the possibility of imaging through obscurations becomes a reality. Imaging through obscurations has numerous civilian and military applications. For instance, Advanced Scientific Concepts (ASC), the manufacturer of the sensor that will be utilized throughout this research effort is currently interested in demonstrating the ability to detect targets obscured by smoke, fog or dust. One particular investigation underway applies to the tracking of a refueling drogue by an autonomous aerial vehicle [13]. The images in Figure 1.2 demonstrate a valuable capability inherent with 3-D FLASH LADAR.

(a) Original Image

(b) Target Visually Obscured by Smoke
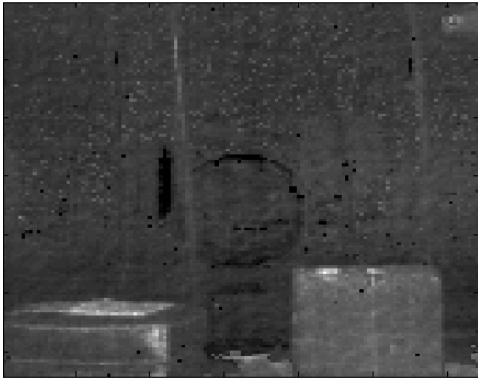
(c) First Return Detection

(d) Second Return Detection

Figure 1.2: In this figure we show a scene visually obscured by smoke. We then show that the 3-D FLASH LADAR system is able to see through the smoke and detect the target of interest.

3

Here we demonstrate that the LADAR system is easily able to detect targets that are visually obstructed by smoke. Figures 1.2(a) and 1.2(b) were taken with a traditional video camera while Figures 1.2(c) and 1.2(d) were taken with a 3-D FLASH LADAR system. The 3-D FLASH LADAR system does receive a return off of the smoke as shown in Figure 1.2(c). However, the multi-surface ranging capability that this dissertation will focus on allows us to detect additional reflections, thus revealing the targets of interest in Figure 1.2(d). Clearly this has numerous military as well as civilian applications. On the civilian side, this technology has applications for vehicles traveling through fog or for firefighters trying to see through a smoky room to rescue trapped personnel. On the military side, this technology would be useful for areas such as landing an aircraft or helicopter in brown out conditions or conducting aerial refueling operations through clouds among others.

Multi-surface ranging with the use of 3-D FLASH LADAR can also be useful in accurately discriminating camouflaged targets of interest. A tactic that is commonly employed on the battlefield is to develop mock targets of low value. These targets are difficult to discern in a tactical environment where the attack may be conducted from miles away in a fast moving vehicle. Thus, it can be an effective tactic because it forces the aggressor to use a potentially high valued weapon on a target of little to no importance. In the visual spectrum it is often easy to generate false targets or hide actual targets with camouflage netting. However, the ability of a 3-D FLASH LADAR system to detect images with range diversity can make it far more difficult to design false targets or effectively camouflage real ones.

Clearly, 3-D FLASH LADAR provides additional useful information to the user. In a traditional 2-D image, we only detect some sort of intensity information in the spatial domain. For 3-D FLASH LADAR images, we not only receive intensity and range information, but depending on the target geometry or physical characteristics,

4

we may also be able to discern information from the width of the reflected pulse. This pulse width information can often be used to discern whether a target is diffuse or solid. Additionally, it may be possible to obtain target orientation based on pulse width expansion [26].

Ultimately, the ability to accurately assess the threat environment is critically important for numerous reasons. Detecting targets that may be concealed by man-made camouflage or natural obscuration has long been a goal of numerous sensor developments, as those targets may pose a threat to the safety of forces or success of a military operation. Optical sensors based on active laser illumination such as FLASH LADAR have the distinct advantage of operating at extremely short wavelengths enabling light to pass through small voids in the obscuration and reflect off of potential surfaces of interest. The ability to finely sample the returned waveform with a high resolution detector array will enable an imaging sensor to produce an accurate representation of the obscured target [50]. In addition to the previously mentioned applications, advancement of this technology has potential application in areas such as terrain mapping, forestry classification and autonomous vehicle navigation.

Current manufacturing limitations for 3-D FLASH LADAR are often centered around sampling rates, detector size and development of optical components that are free from aberration. The dimensions of each pixel in the detector array are currently the primary limiting factor on attainable spatial resolution. As with all emerging camera technologies, we expect this to improve as manufacturing processes are refined. Unfortunately, as a consequence of nonuniform heating and cooling of the Earth's atmosphere, the temperature-induced inhomogeneities of the refractive index of the air may have a significant impact on attainable spatial resolutions [21]. This dissertation will address those problems and reinforce that previously ill-posed problems for 2-D imaging may actually be overdetermined for 3-D imaging [49].

1.2   LADAR Technology
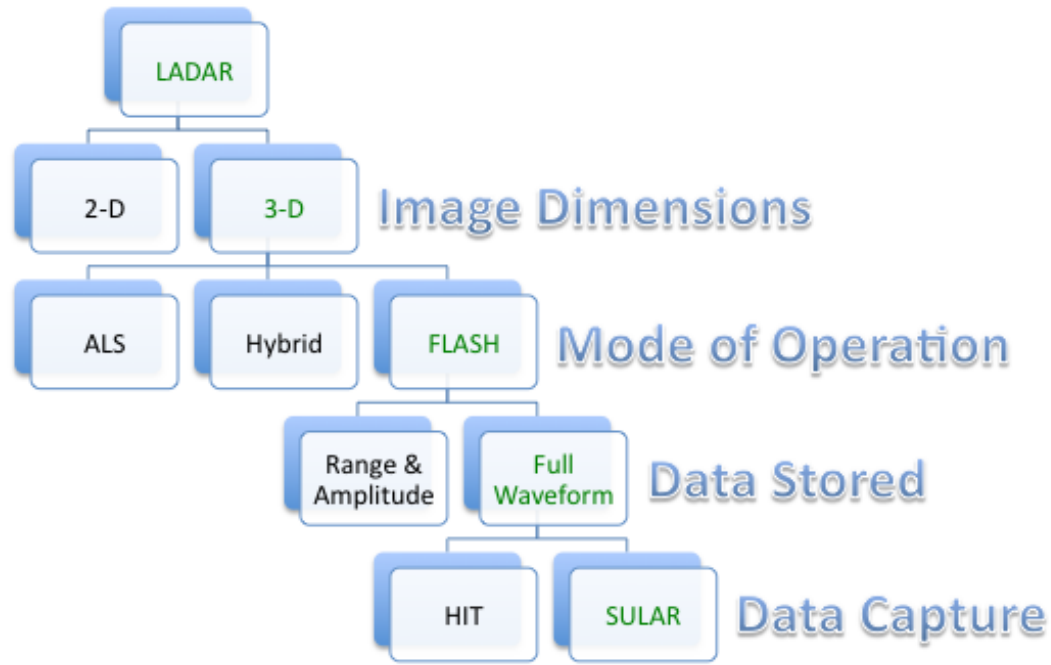
Figure 1.3: LADAR flow chart with the specific technology that the bulk of this research will be concerned with down the right hand side highlighted in green.

LAser Detection and Ranging (LADAR) systems are a subset of LIght Detection and Ranging (LIDAR) systems where the delineation is tied to the type of illumination source. Further exploration of this class of sensor warrants a brief description of the numerous variations on the technology. Figure 1.3 encapsulates many of the numerous variants of LADAR technology. There are currently two widely recognized forms of 3-D LADAR systems. One type is a scanning LADAR system where each pixel in the image is a result of measuring the return from a separate laser pulse. The scanning variant of LADAR has been widely studied, and many algorithms have been developed to process the measured data such as in [31], [32] and [63]. While the Airborne Laser Scanner ALS variants of 3-D LADAR have demonstrated unique capability in remote sensing, they commonly require a significant amount of time to form a complete

6

image. The time delay associated with this technique will likely be unacceptable for employment on a fast moving platform operating in a highly dynamic environment. Fortunately, continuing technical advancements are giving rise to systems known as 3-D FLASH LADAR systems.

Unlike scanning LADAR systems, a 3-D FLASH LADAR is able to form a complete 3-D image or data cube by simultaneously measuring the returned pulse for every pixel in an image. The 3-D image or data cube is essentially a series of images where an Avalanche Photo Diode (APD) array measures the returning photons for each pixel separated by a constant time interval. Figures 1.4 and 1.5 provide a simplified sketch of a 3-D FLASH LADAR in operation. Commonly, a laser illuminator
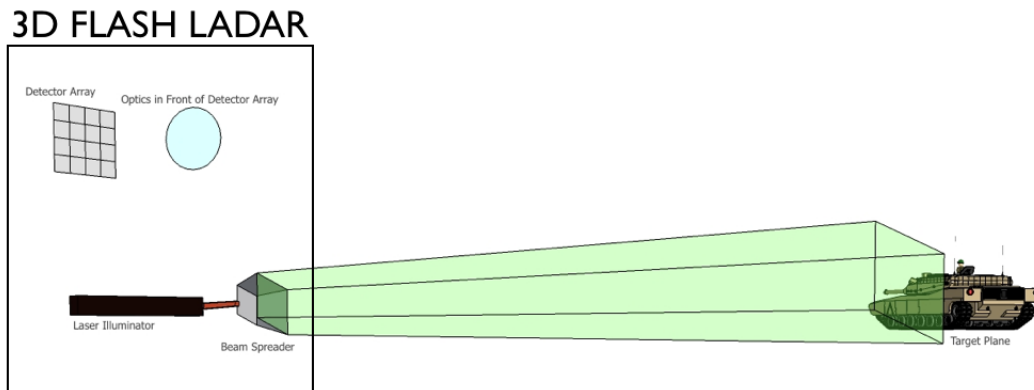
Figure 1.4: Transmit Portion of 3-D FLASH LADAR Operation.
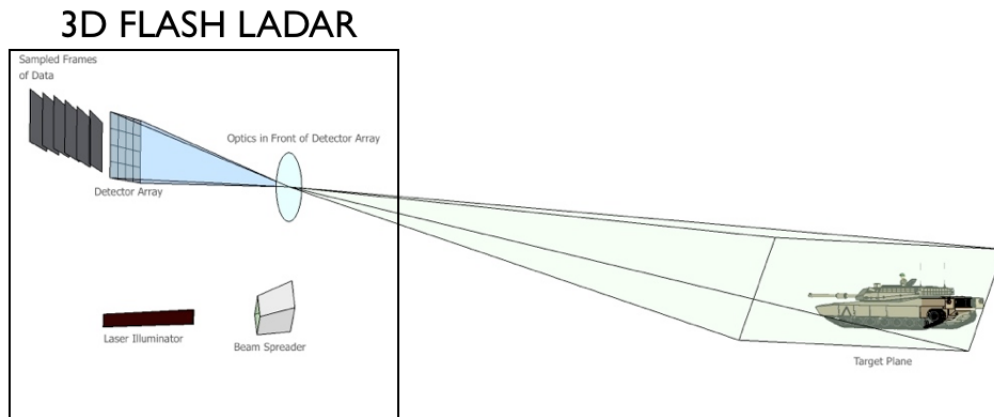
Figure 1.5: Receive Portion of 3-D FLASH LADAR Operation.

will fire a short pulse of light through some sort of beam spreader to achieve the desired illumination of the target area. In a full-waveform system, the APD array will then simultaneously sample the reflected pulse for each pixel in the detector array at a predetermined rate. A separate 2-D image will be formed for each sampling of the reflected laser pulse. Based on this methodology, accurate ranging will be highly dependent upon the ability to precisely account for the time of flight of the laser pulse.

The sampling rate and number of samples within the range gate will be largely system/mission dependent; however, it is worthwhile to consider the two common methods for triggering the start and end of the range-gate. The first mode under consideration, Staring Underwater LAser Radar (SULAR) mode, records the first frame of data at a pre-defined time from when the pulse was fired. In this manner, the range gate for a 3-D image will have a fixed window for each detector based on the start time, time between frames and total number of frames in the 3-D image. Another mode of operation is commonly referred to as "HIT mode" where each image pixel may trigger the start of the range gate at a different time based on the received signal level. The bulk of the research presented in this dissertation will focus on 3-D FLASH LADAR operating in SULAR mode.

1.3   Research Contributions

The following subsections offer a brief description of each of the three core areas of research covered in this dissertation as well as their associated contributions.

1.3.1 Parameterized Blind Deconvolution Through Convergence of Variance (Chapter III).

This area of research first revisits algorithms originally presented by MacManus and MacDonald for accomplishing parameterized blind deconvolution of Two - Dimensional (2-D) images in the presence of Poisson and negative binomial noise [41], [45]. The Convergence of Variance (CoV) algorithm developed by MacManus and the Maximum *a-priori* (MAP) estimate developed by MacDonald each offer blind deconvolution methods tailored for implementation in a tactical environment where processing time is extremely important. Initially, a comparison of the two algorithms is offered and several unique conclusions are developed. Ultimately a new explanation is given which reveals that the MAP estimate provides no new capability over the CoV technique. Further, an extension to the CoV algorithm is proposed in order to perform parameterized blind deconvolution on 3-D FLASH LADAR images. The primary goal of this portion of research was to demonstrate the ability to find a parameterized Point Spread Function (PSF) which could be used in the multi-surface ranging algorithm presented in Chapter IV.

1.3.2 Multiple Surface Detection and Estimation (Chapter IV).

The core area of research for this dissertation was the development of a novel iterative algorithm using an Expectation Maximization (EM) strategy which will simultaneously solve for multiple ranges per image pixel and remove the effects of diffraction [14]. Challenges with employing an EM strategy are discussed, and the techniques developed to mitigate those challenges are presented. Additionally, a constraint is proposed and applied to the initially developed multi-surface ranging algorithm which further enhances its capability. Both the constrained and non-constrained multi-surface algorithms which account for the effects of diffraction are then compared

against an algorithm which does not account for diffraction and one that employs traditional 2-D image deconvolution techniques to account for diffraction. This new algorithm is ultimately shown to provide a significant improvement in multi-surface ranging capability. This capability will be critical in employing 3-D FLASH LADAR technology in an environment where the ability to image through obscurations is required.

1.3.3   Imaging Through Turbulence (Chapter V).

Finally, the next step in enhancing the multi-surface detection algorithm presented in Chapter IV is developed. Initially the multi-surface ranging algorithm assumed a known PSF to account for the effects of diffraction. Determining the PSF is a challenging problem known as blind deconvolution that has been the focus of a wealth of research. Traditionally, blind deconvolution problems for 2-D images are ill-posed. However, this research shows that a maximum likelihood approach to estimate the PSF parameterized by Fried's seeing parameter, r_0, is possible with the addition of range diversity from 3-D images. Unlike the MAP estimate proposed by MacDonald and discussed in Chapter III, this technique does not require the introduction of a *prior* distribution for the value of r_0. Alternatively, the CoV technique developed by MacManus could first be used to identify a parameterized PSF before proceeding to use the multi-surface ranging algorithm to develop the surface profile. However, this research will show that both the value for r_0 and the surface profile can be estimated simultaneously. Systems of equations will be provided that highlight the added capability of working this type of problem with 3-D FLASH LADAR images. Finally, the results will be verified through the use of both simulation and experimental data.

1.4 Organization

This document will be organized as follows. Relevant background material on LADAR technology, theoretical models and experimental data collection systems will be presented in Chapter II. Chapter III examines two previously developed parameterized blind deconvolution algorithms, and discusses their application to 3-D FLASH LADAR imagery. Chapter IV will detail the derivation of a multi-surface ranging algorithm that simultaneously develops the range profile and removes the effects of diffraction from a 3-D FLASH LADAR image, given a known PSF. Chapter V presents a joint estimation technique for simultaneously developing the range profile and parameterized PSF. Finally, Chapter VI will summarize the conclusions from this research and present ideas for future research.

II. Background

This chapter presents necessary support material for the research presented in this dissertation. First, a model will be presented for simulation and representation of the data received by a 3-D FLASH LADAR sensor. Additionally, theory will be presented to identify the ill-effects of imaging through a turbid medium in Section 2.1. Common techniques for improving the overall Signal to Noise Ratio (SNR) in the detected images will then be presented in Section 2.2. Section 2.3 will focus on a 2-D and 3-D sensor that will be used throughout the research effort for the collection of measured data. An important concept for any iterative algorithm is how to determine when the algorithm can terminate. This research will employ the convergence of variance as the stopping criteria as discussed in Section 2.4. In simulation, the blur applied to the detected image, or PSF, is known. However, with experimental data, we must be able to measure the PSF for comparison with the estimates obtained from the algorithms developed. Section 2.5 will present the method used for measuring Fried's seeing parameter, r_0, which will be used in the parameterized model for the PSF. Finally, this chapter will present a summary of similar research previously accomplished in Section 2.6.

2.1 3-D FLASH LADAR Theory

Three dimensional FLASH LADAR is fundamentally different from scanning variants in that the entire remote scene is illuminated with a single short pulse of the laser illuminator. On the other hand, the scanning variants only illuminate a narrow Field of View (FOV) corresponding with a single image pixel per pulse of the laser. This narrow beam is then scanned over the target area to compile an entire 3-D image. While scanning systems have been shown to provide extremely detailed images, the

size, complexity, low frame rate and cost of stabilization and beam steering hardware make the technology impractical for tactical use.

This research will utilize some concepts learned through previous research with scanning variants of LADAR; however, the research will focus on the 3-D FLASH LADAR variants. Since the entire remote scene is illuminated with a single pulse of the laser, the resultant data collected will depend on the triggering mechanism employed. As shown in Figure 1.3, the data stored is primarily classified as either Range and Amplitude (R&A) or full waveform. For the R&A data, each pixel in the detector will employ some sort of detection methodology to determine the range and intensity from the reflected waveform. The only data stored for each pixel will be the resultant range and amplitude. In full waveform data, there are various forms of triggering mechanisms worthy of discussion. The ASC systems employ either HIT mode or SULAR mode of triggering. HIT mode allows for each pixel within the detector to have a unique range gate where the start of the range gate is triggered at some intensity threshold. While the HIT mode of operation definitely has application, the techniques presented in this research require that each pixel in the image have the same range gate.

For the SULAR mode of operation, each pixel within the detector will have precisely the same range gate. Each time the detector is sampled, a separate 2-D frame will be stored which contains an intensity representation corresponding with the number of photons received over the detector integration time. Therefore, each 2-D frame will also have a discrete range corresponding to its sample time. This compilation of data frames can then be stacked into a 3-D data cube such that each pixel in the detector will have the reflected waveform corresponding to the target area and the established range gate. Based on this mode of operation, it is possible that certain portions of the scene may not result in a pulse return within the range gate. These

non-illuminated areas of the scene will therefore only measure the detector bias for each sample within the range gate.

Accounting for range once a certain threshold is achieved or where a peak is detected can only provide range accuracy to the nearest sample. Provided the sample rate is high enough, full waveform data storage allows for highly precise ranging capability. Generally we would want to sample the detector at the Nyquist rate. Then, using techniques such as the correlation method presented by Richmond and Cain [58], or the EM algorithm presented in this research, we can achieve sub-sample ranging accuracy.

2.1.1 Pulse Model.

This research will employ the common technique of modeling the transmitted and received pulse for a LADAR system as a Gaussian (single-surface case) or mixture of Gaussians (multi-surface case). While the outgoing waveform will largely dictate the inaccuracy induced by the Gaussian approximation, for many sensors this model is generally considered acceptable [46]. Future work may consider the error introduced; however, the error is likely to be sensor dependent [58]. Using an early variant of the FLASH 3-D LADAR sensor developed by ASC, the Gaussian approximation allowed for accurate single surface ranging algorithms to be developed by Dolce [16] and McMahon [48]. The Gaussian model for the received intensity of the pulse $P(t)$ is

$$P(t) = \frac{A}{\sigma\sqrt{2\pi}} \exp\left[-\frac{t^2}{2\sigma^2}\right] \tag{2.1}$$

where t is time, A is the pulse amplitude and σ is the width parameter.

Using the Gaussian model as our basis, much of this dissertation will consider the

possibility of N surface returns per image pixel according to

$$P(x, y, r_k) = \sum_{n=1}^{N} P^{(n)}(x, y, r_k). \qquad (2.2)$$

Where each of the N individual Gaussian pulses, $P^{(n)}$, reflected by the target at a range of $r^{(n)}$ is

$$P^{(n)}(x, y, r_k) = \frac{A^{(n)}(x, y)}{\sqrt{2\pi}\sigma^{(n)}(x, y)} \exp\left[-\frac{\left(r_k - r^{(n)}(x, y)\right)^2}{2\left(\sigma^{(n)}(x, y)\right)^2}\right]. \qquad (2.3)$$

The indexes x and y indicate the area in the target plane corresponding to the individual pixels in the $M \times M$ detector array, and the index r_k represents the discrete range for the kth frame in the data cube, or in other words, each time the pulse is sampled by the sensor. The nth amplitude, pulse width and range of the pulse mixture are represented by $A^{(n)}$, $\sigma^{(n)}$ and $r^{(n)}$ respectively.

The received pulse is modeled by the intensity function $I(u, v, r_k)$, where the received intensity is found by convolving the pulse and the PSF, h, as shown in

$$I(u, v, r_k) = \sum_{x=1}^{M} \sum_{y=1}^{M} P(x, y, r_k) h(u - x, v - y), \qquad (2.4)$$

where the indexes u and v represent the detector plane coordinates. It has been demonstrated that the number of photons that arrive during the detector's integration time can be modeled with Poisson statistics [21]. Section 2.2 will discuss the choice of Poisson statistics over negative binomial statistics in more detail. In addition to the laser light reflected off of the target, the detector may also receive photons from background lighting, and thermal noise. These additional photon sources will be accounted for as a pulse bias for each detector in the APD array $B(u, v)$. The noise generated by the bias will also follow a Poisson distribution, resulting in a model for

the total intensity measured by the detector of

$$I_{tot}\left(u, v, r_k\right) = \left[\sum_{n=1}^{N}\sum_{x=1}^{M}\sum_{y=1}^{M} P^{(n)}\left(x, y, r_k\right) h\left(u - x, v - y\right)\right] + B\left(u, v\right). \qquad (2.5)$$

In Section 4.1, a method is derived for estimating the pulse bias in conjunction with the amplitude, pulse width and range of the pulse. In reality, the signal bias could be measured by producing an image in the absence of a laser pulse; however, this may not always be possible, thus driving the additional need to estimate this parameter.

If we assume independence of the measurements at each time step and for every pixel in the detector array, we can state the joint probability of the observed data, d, as

$$p\left[D_k(u, v) = d\left(u, v, r_k\right); \forall u, v, k\right] = \prod_{u=1}^{M}\prod_{v=1}^{M}\prod_{k=1}^{K} \frac{I_{tot}\left(u, v, r_k\right)^{d(u,v,r_k)} e^{-I_{tot}(u,v,r_k)}}{d\left(u, v, r_k\right)!}. \qquad (2.6)$$

To minimize confusion in notation, an upper-case P will be used to represent the pulse, and lower-case p will be used in representation of the various probabilities throughout this work. The expected value of the noisy 2-D frame, $D_k(u, v)$, corresponding with a range to target of r_k is $I_{tot}(u, v, r_k)$.

In summary, each 2-D frame is impacted by the effects of diffraction, an additive bias and noise as shown in Figure 2.1. The noisy received 3-D image, d, of a remote object, o, is comprised of a series of 2-D frames. The received intensity for each frame, I_{tot}, is the summation of an additive bias and the blurred image, i.
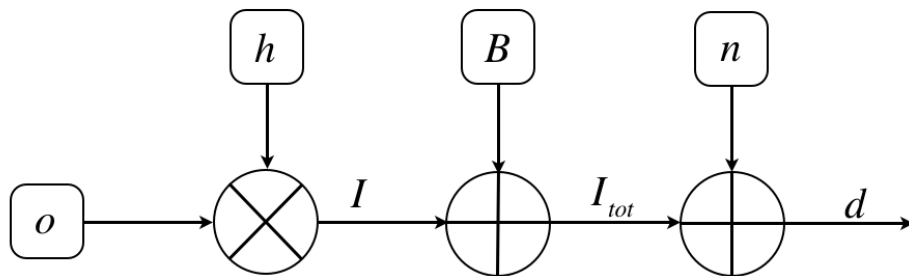
Figure 2.1: Model for received data that is impacted by diffraction and noise.

2.1.2 Spatial Sampling Requirements.

In the diffraction limited case, the maximum achievable spatial frequency, ν_{max}, can be computed by

$$\nu_{\max} = \frac{D}{\lambda f_l},\tag{2.7}$$

where λ is the wavelength of the light of interest and f_l is the focal length of the lens and D is the aperture diameter [22]. According to the Nyquist criterion, the ability to perfectly reconstruct a digitally sampled image, or properly sample, would therefore require a sampling frequency of $2\nu_{\max}$. The importance of properly sampling an image stems from the use of convolution in the model for intensity as shown in (2.5).

Achieving Nyquist sampling is a significant challenge in many optical sensing applications, and especially in the case of 3-D FLASH LADAR. The complexity of the electronics coupled with conventional optics often results in a detector pixel pitch that is much greater than what is required for proper sampling. However, assuming the standard progression of technology, history has shown that the pixel pitch will decrease. The techniques presented in this dissertation are again intended to demonstrate the potential value of the methodology. Future research efforts could be tied to exploring their utility where proper sampling may not be possible.

2.1.3 Sources of Image Blurring and Degradation.

Due to numerous physical phenomena, the images captured by a sensor have imperfections. First, we know that optical imperfections with the system can cause the diffraction of light to neighboring areas. When operating a sensor within the atmosphere, optical imperfections can commonly be binned into those directly related to the manufacturing of the sensor and those that result from atmospheric turbulence. Second, the received image is generally further degraded by the effects of noise. This noise can also result from numerous sources such as read out noise, thermal noise and

noise associated with the illumination source.

The total PSF or spatial impulse response of an optical sensor accounts for the diffraction effects directly attributed to the sensor optics, h_{opt}, and those that can be attributed to atmospheric turbulence, h_{atm}. This total PSF, h_{tot}, is the 2-D convolution of the two primary components as shown in (2.8), where x and y are the spatial coordinates of the individual PSFs.

$$h_{tot}(x, y) = h_{opt}(x, y) \otimes h_{atm}(x, y) \tag{2.8}$$

A direct solution for the impulse response of a non-ideal aperture is difficult to compute; however, it can be found by conducting a propagation experiment using known sensor parameters [58]. In frequency space, the total Optical Transfer Function (OTF), H_{tot}, the optics OTF, H_{opt}, and atmospheric OTF, H_{atm}, are simply the Fourier transforms of their respective PSFs, and the convolution operator is replaced by the multiplication operator

$$\mathcal{F}\{h_{tot}(x, y)\} = H_{tot}(\nu_x, \nu_y) = H_{opt}(\nu_x, \nu_y) H_{atm}(\nu_x, \nu_y), \tag{2.9}$$

where the spatial frequencies in two dimensions are parameterized by (ν_x, ν_y) and $\mathcal{F}$ is the Fourier operator.

Imaging devices have an upper bound on their cutoff frequency dictated by their optical specifications according to (2.7). Imaging through a turbid medium will at best cause no further attenuation to the frequency content of an image, but can often result in significant attenuation. In a 2-D image, this attenuation of frequency content manifests as a spatial blurring of the image. However, since the 3-D FLASH LADAR image is a composition of numerous 2-D frames, this spatial blurring will also cause a temporal distortion as well.

As a general rule of thumb, when collecting images with exposure times of less than $\frac{1}{100}$ of a second we can assume that the atmosphere through which the remote scene is viewed remains constant [21]. While the instantaneous atmosphere is difficult to measure and even more challenging to estimate, models exist to predict its behavior on average. In the short exposure scenario where the total exposure time is less than $\frac{1}{100}$ of a second, we have the average OTF, $\bar{H}_{SE}$,

$$\bar{H}_{SE}\left(\nu_x, \nu_y\right) = \exp\left\{-3.44 \left(\frac{\bar{\lambda}^2 f_l^2 \left(\nu_x^2 + \nu_y^2\right)}{r_0^2}\right)^{5/6} \left[1 - \left(\frac{\bar{\lambda}^2 f_l^2 \left(\nu_x^2 + \nu_y^2\right)}{D^2}\right)^{1/6}\right]\right\}.$$

(2.10)

In the mathematical model for $\bar{H}_{SE}$ as a function of spatial frequency, the mean wavelength of light detected is $\bar{\lambda}$ and r_0 is Fried's seeing parameter. Applying this model essentially has two stipulations of concern. First, we must have a sufficiently short exposure time to satisfy the static atmosphere requirement. Clearly a single image taken with a 3-D FLASH LADAR system falls within this requirement. Second, we must be able to register the images to remove the motion effects of tip / tilt caused by the atmosphere. For purposes of this research, we will substitute $\bar{H}_{SE}$ as our model for the atmospheric OTF, H_{atm}. However, the techniques developed in subsequent chapters could also be demonstrated to work with the simpler long-exposure case where the image frames are averaged without motion compensation. The average long-exposure OTF, $\bar{H}_{LE}$, is

$$\bar{H}_{LE}\left(\nu_x, \nu_y\right) = \exp\left\{-3.44 \left(\frac{\bar{\lambda}^2 f_l^2 \left(\nu_x^2 + \nu_y^2\right)}{r_0^2}\right)^{5/6}\right\}.$$

(2.11)

Even though the individual exposures of the 3-D FLASH LADAR sensor are less than $\frac{1}{100}$ of a second, the use of this model would apply in cases where we chose not to account for the tip / tilt motion caused by the atmosphere.

2.2 Image Variance and Effects of Averaging

Due to the partially coherent nature of the illumination source, the reflected photon distribution is negative binomial. This results in a somewhat complex noise distribution for the composite pixel intensity for each frame. The composite intensity also has noise contributions from background illumination which is commonly modeled with a Poisson distribution. Experience has shown that the negative binomial noise from the reflected laser pulse is commonly the most dominant form of noise. Therefore in regions of relatively high illumination, the other sources of noise are indistinguishable. The negative binomial Probability Mass Function (PMF) model defines the probability that we will receive K photons over the integration time as

$$p\left(K\right) = \frac{\Gamma\left(K + \mathcal{M}\right)}{\Gamma\left(K + 1\right)\Gamma\left(\mathcal{M}\right)}\left[1 + \frac{\mathcal{M}}{\bar{K}}\right]^{-K}\left[1 + \frac{\bar{K}}{\mathcal{M}}\right]^{-\mathcal{M}}, \qquad (2.12)$$

where $\mathcal{M}$ is the coherence parameter of the laser illumination and $\bar{K}$ is the expected number of photons. Due to its complexity, the negative binomial PMF does not lend itself to the algorithms that were developed through the course of this research. Fortunately, the Poisson PMF has been shown to be an adequate substitution based primarily on the similarity between the shapes of the two PMFs given the standard range of coherence parameters [41], [47]. As $\mathcal{M}$ approaches infinity, the variance of a negative binomial random variable collapses to the mean,

$$\sigma_{NB}^2 = \bar{K}\left(1 + \frac{\bar{K}}{\mathcal{M}}\right), \qquad (2.13)$$

thus converging to a Poisson variance. A comparison of the negative binomial and Poisson PMF is shown in Figure 2.2. Here we see that as $\mathcal{M}$ increases, the negative binomial PMF does in fact approach the Poisson PMF.

Motion Compensated Frame Average (MCFA) images are commonly used in imag-
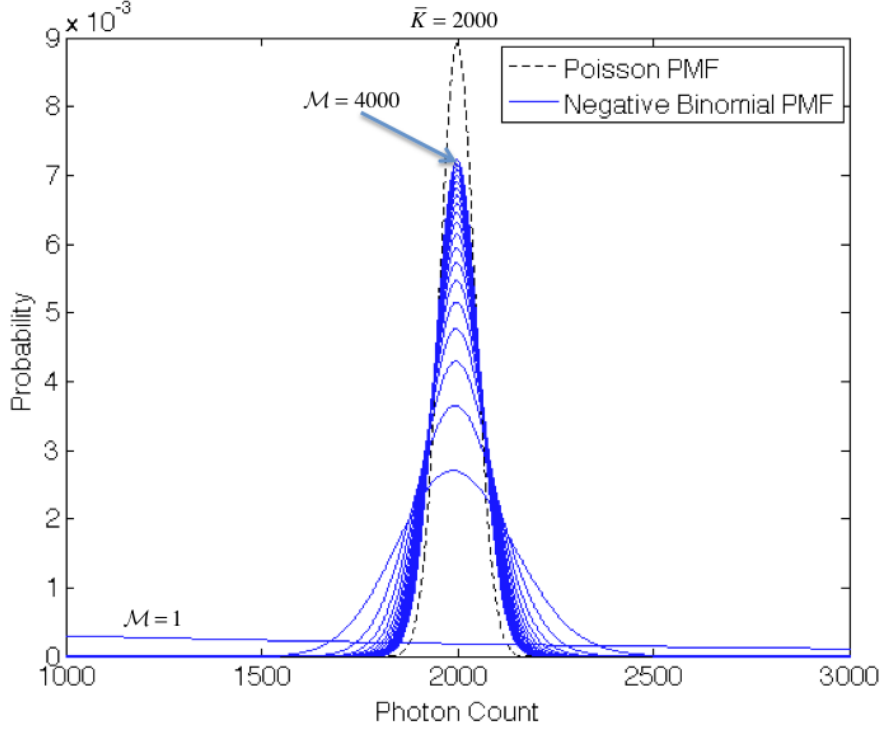
Figure 2.2: Convergence of the negative binomial PMF to the Poisson PMF with increasing $\mathcal{M}$ and $\bar{K} = 2000$.

ing applications to improve the SNR. The value of using an MCFA can best be understood through a simple example. For digital image processing, SNR is commonly modeled as

$$SNR = \frac{\bar{K}}{\sigma}, \tag{2.14}$$

or the ratio of mean photons measured to the standard deviation of the measurement [20]. This definition of SNR is only justified when the mean is always non-negative such as the case with photon counts. For simplicity, we will now consider a Poisson process for which we know the mean is equal to the variance. If our MCFA consists of the summation of two independent measurements, both the mean and variance will increase by a factor of two. However, the standard deviation only increases by a factor of $\sqrt{2}$. Therefore, the SNR also improves by a factor of $\sqrt{2}$ every time we double the number of frames we are averaging. Averaging frames serves to greatly mitigate the

22

ill effects of speckle noise in laser illuminated images [42]. Finally, averaging frames also serves as the catalyst for using the average model for the atmosphere when trying to enhance the spatial and temporal resolution of the 3-D image.

An additional benefit of using MCFA images is that it will also serve to increase $\mathcal{M}$. Given the variance of an individual image as shown in (2.13), the variance of a 2-image MCFA, σ_{NB2}, will be

$$\sigma_{NB2}^2 = 2\bar{K}\left(1 + \frac{\bar{K}}{\mathcal{M}}\right). \tag{2.15}$$

If we can now assume that the expected photons received for each image is constant,

$$\bar{K}_1 = \bar{K}_2 = \bar{K}, \tag{2.16}$$

we can perform a substitution of variables to show that $\mathcal{M}$ doubles for a 2-frame MCFA. The 2-frame MCFA will also have a negative binomial distribution with

$$\sigma_{NB2}^2 = \bar{K}'\left(1 + \frac{\bar{K}}{\mathcal{M}}\right) = \bar{K}'\left(1 + \frac{\bar{K}'}{2\mathcal{M}}\right), \tag{2.17}$$

where

$$\bar{K}' = \bar{K}_1 + \bar{K}_2 = 2\bar{K}. \tag{2.18}$$

Since the shape of the negative binomial PMF is primarily driven by $\mathcal{M}$, this increase in $\mathcal{M}$ will ultimately make our Poisson approximation more accurate.

2.3 Experimental Data Collection Systems

This section will present the two camera configurations that were used to obtain experimental results to support this dissertation. All of the equipment was commercially available, but in some cases modified slightly to perform in accordance the

expectations designed into the algorithms.

2.3.1   2-D Visible Light System.

The optical configuration shown in Figure 2.3 was used to obtain properly sampled 2-D images. The experimental results obtained with this setup were primarily used to verify initial concepts on the impact of turbulence on images, the ability to measure r_0 and in support of the research presented in Chapter III. The specifications for this setup are listed in Table 2.1. The camera used in this configuration allowed for 16-bit

Figure 2.3:   Experimental sensor setup consists of a Celestron® NexStar® 6SE 1.5 m focal length telescope with a mask to reduce the aperture to 5 cm, and an Orion® Starshoot$^{\text{TM}}$ G3 monochrome camera.

Analog to Digital (A/D) conversion and experiments show that it acts as a photon counting device in lower intensity regions. This allows for utilization of the Poisson and negative binomial model assumptions without applying a conversion factor to the digitized images. However, as the detector approached higher intensity thresholds, the conversion between digital counts and photons became non-linear. For that reason, images were taken in low light conditions to ensure the various techniques developed through this research could be applied.

Table 2.1: Optical System Specifications.

Parameter Name	Defined Value
Mean wavelength ($\bar{\lambda}$)	600 nm
Detector array size	582×582
Pixel size	8.3 μm $\times$ 8.6 μm
Sensor focal length (f)	1.5 m
Aperture diameter (D)	5 cm

2.3.2   3-D FLASH LADAR System.

The 3-D FLASH LADAR sensor used for this research was a modified ASC
Portable 3-D FLASH LADAR Camera Kit$^{\text{TM}}$. The sensor used all of the standard
components in this commercially available sensor; however, they were oriented into a
different configuration for the USAF Test Pilot School (TPS) as shown in Figure 2.4.
The system specifications as configured are listed in Table 2.2.

(a) Standard camera configuration   (b) TPS camera configuration
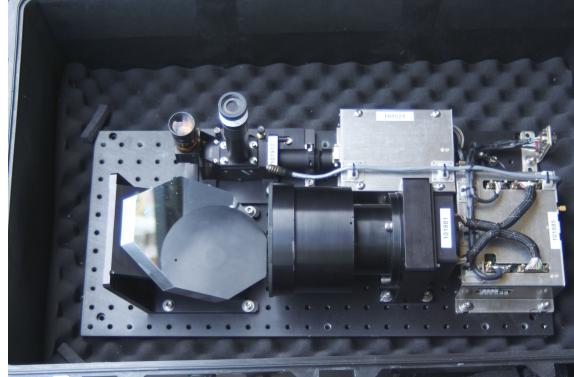
**Figure 2.4:   (a) This is the standard configuration of the camera available from ASC.
(b) In order to meet USAF TPS requirements, the camera components were oriented
into a brassboard design to allow for installation into an airborne pod.**

The experimental 3-D FLASH LADAR sensor possessed a fixed-focus lens, with
focus set to infinity. While this configuration would be advantageous for installation
into an airborne pod where long slant ranges to the target are common, it did create
some challenges in trying to establish suitable experimental target configurations.

Table 2.2: ASC Portable 3-D FLASH LADAR System™Specifications.

Known System Parameters	
Parameter Name	**Defined Value**
Frames per image	20
Mean laser wavelength ($\bar{\lambda}$)	1.57 μm
Measured sample rate	434.5 MHz
Energy per pulse (E_t)	0.025 J
Sensor pulse width	$4.7 \times 10^{-9} s$
Detector array size	128 × 128
Pixel size	100 μm × 100 μm
Lens Parameters	
Parameter Name	**Defined Value**
Sensor focal length (f_l)	250 mm
Aperture diameter (D)	12 cm
Instantaneous Field of View (iFOV)	3°

Each individual 3-D image consisted of 20 2-D frames. In SULAR mode where each pixel within the detector is set to a fixed range gate, this would result in a significant limitation. Based on the sample rate, the range gate would be limited to approximately 6.56 m with each 2-D frame separated by 0.345 m. Fortunately the camera has a mode of operation known as "STOP" mode. In this mode of operation, 3-D images, each with 20 frames, can be taken with various starting points for the range gate. The 3-D image for each subsequent STOP will be formed from a separate laser pulse and will provide an additional 8 frames of data extending the range gate by approximately 2.76 m per STOP. Figure 2.5 illustrates how the composite image is reassembled to achieve a longer range gate. The camera has been tested with a total of 9 additional STOPs for a total range gate of 31 m. In this mode of operation we are truly only limited in the sensor's ability to quickly read and store a significant amount of digitized data. While this research appears somewhat constrained by the requirement of using the SULAR mode of operation, techniques such as STOP mode mitigate this constraint.
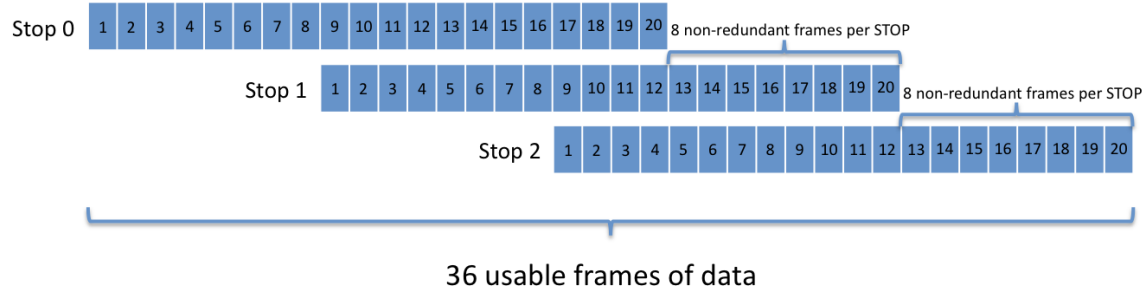
Figure 2.5: Assembly of Composite 3-D Image Using Two Additional STOPS.

2.3.3 Speckle Parameter Estimation and Photon Calibration.

The algorithms developed in this research are based on statistical models for the photon arrival rates of partially coherent and incoherent light. Therefore, a calibration of both experimental sensors was warranted. For instance, the iterative algorithms will use a stopping criteria that depends on a comparison of the variance between the non-noisy estimates and the measured data. Additionally, one of the algorithms depends on the ability to calculate likelihood across a range of parameters. Therefore, we must understand the sources of variation in the measured data, and the overall number of photons received.

Digital cameras commonly produce images by computing a digital count that corresponds with the photons received at the detector plane over the integration period. Unless the camera is a true photon counting device where the digital count is equivalent to the photons received, the statistics will be skewed. The variance of a random variable X is defined as

$$\sigma_X^2 = E\left[(X - \mu_X)^2\right],\tag{2.19}$$

where μ_X is the mean of the random variable X. Modeling the received photons with

27

the random variable Y, a scaling by some factor, c, will yield

$$Y = cX. \tag{2.20}$$

In converting to camera counts, the variance of this scaled value, σ_Y^2, will become

$$\begin{aligned}
\sigma_Y^2 &= E\left[(Y - \mu_Y)^2\right] = E\left[(cX - c\mu_X)^2\right] \\
\sigma_Y^2 &= (c^2) E\left[(X - \mu_X)^2\right] \\
\sigma_Y^2 &= c^2 \sigma_X^2.
\end{aligned} \tag{2.21}$$

By imposing a scaling factor when converting to camera counts, the variance too is scaled by the square of that scaling factor. Therefore, if the distribution of the light received should be Poisson, a scaled representation of the photons received in the form of camera counts will clearly not be Poisson.

For a camera that is measuring natural light, the conversion of camera counts is rather simple. Since a Poisson process will have a mean equal to the variance, we only need to find a scaling factor that allows for this condition to hold. However, caution must be exercised to ensure that conversion is linear for the intensity range of interest, or the non-linearity will need to be addressed. For the experimental configuration presented in Figure 2.3, this calibration was accomplished by first taking a series of images with the lens cap on in order to capture the variance associated with the detector bias. A series of 100 short exposure images was then captured for a uniformly illuminated step target. This step target captured the minimum and maximum intensity range that we expected in our experiments. The mean and variance were then computed for this series of images in an attempt to find the scaling factor as shown in Figure 2.6. Fortunately the mean and variance were found to be approximately equal for the intensity ranges we were concerned with. Given that the

(a) Step Target   (b) Pixel Mean and Variance
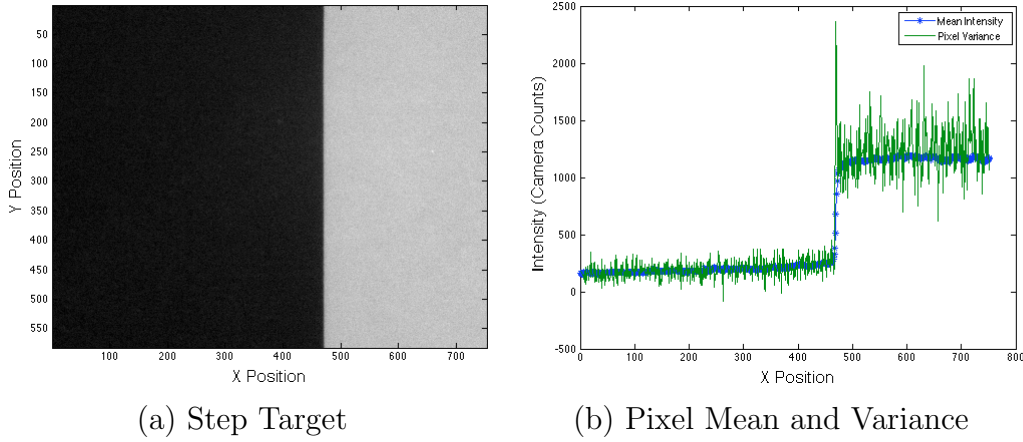
Figure 2.6: **(a) Shows the step target used to capture the minimum and maximum expected intensity. (b) Comparison of pixel mean and variance for a 1-D slice through the middle of the image.**

camera has a 16-bit A/D converter, intensity values can range from 0 - 65535. Our experimentation found that as long as an individual pixel intensity remained below 2,000 camera counts, there was approximately a 1 to 1 ratio for camera counts to photons.

With the calibration for natural light achieved, the calibration for the coherence parameter, $\mathcal{M}$, of the laser illuminator used in the 2-D experiments was possible. Given that the partially coherent light will have a negative binomial distribution we simply needed to find the $\mathcal{M}$ that minimized the Mean Square Error (MSE) between the variance computed from (2.13) and the measured variance. For the 2-D experiments, the remote scene was illuminated using a laser with a wavelength of 630nm and a measured coherence parameter, $\mathcal{M} = 10$.

The calibration of the 3-D FLASH LADAR sensor was more complex. Previous research has relied on a two step calibration process that was similar to what was used for the 2-D experimental setup [47]. However, this technique depends on the ability to collect images that are illuminated by incoherent light. This was accomplished by pointing the sensor at a bright scene, and collecting images with the laser illumina-

29

tor inhibited. Unfortunately, this technique was not possible with the 3-D FLASH LADAR camera used for this research. It is unknown if the lens on this particular setup used a filter to attenuate wavelengths outside of a narrow band around the laser illuminator, as attempts to calibrate the photon to camera count ratio with natural light were inconsistent. Therefore, a scheme was required that allowed for simultaneous calibration of the camera count to photon calibration and coherence parameter. A technique was developed that uses the χ^2 goodness of fit test to allow for this calibration. Finally, the 3-D FLASH LADAR camera has numerous different detector sensitivity settings that will allow the camera count to photon count calibration to vary. Previous work with an ASC LADAR system [7], and information provided by the manufacturer led us to believe that this system was a photon counting device. In other words, we expected the photon to camera count conversion factor to be 1. However, we were looking for a technique to confirm this information to be true for the system used for this research.

Given that we can easily collect dark images with the 3-D FLASH LADAR camera by placing a cover over the lens, it was possible to characterize the variance attributed to the combined camera bias. The remaining variance in the images can primarily be attributed to the collection of the partially coherent illumination. In regions of high intensity returns within the image, the variance will be dominated by speckle noise with a negative binomial distribution. Additionally, it is known that the shape of the distribution is primarily determined by the coherence parameter [21]. Therefore, a technique was derived using the chi-squared goodness of fit, or χ^2 test, under the hypothesis that we could use this test to first identify a likely candidate for the coherence parameter given the shape of the distribution. The χ^2 goodness of fit test statistic, X^2, is

$$\mathrm{X}^2 = \sum_{z=1}^{Z} \frac{(O_z - E_z)^2}{E_z}, \tag{2.22}$$

where we form an expected distribution with Z bins and O_z is the observed number of occurrences and E_z is the expected number of occurrences for a particular bin.

Knowing that the reflected illumination is partially coherent, we seek to find out if the received data are from a particular negative binomial distribution. We still have two unknowns, the photon scaling parameter and $\mathcal{M}$. However, since the shape of the distribution is primarily determined by $\mathcal{M}$, we expected that the χ^2 test would reveal similar results across a range of scaling factors. We could then use the results for $\mathcal{M}$ to directly calculate the scaling based on a comparison with the theoretical variance in (2.13). If our X^2 statistic is high, we can conclude that the data are not a part of the tested distribution and accept the alternate hypothesis, H_1, which states we have a lack of fit. However, if our X^2 statistic is low, we fail to reject the null hypothesis, H_0. Therefore, we are looking for the *non-rejection* region where we fail to reject H_0 in order to identify the most likely value of $\mathcal{M}$. In using the χ^2 test to find the $\mathcal{M}$ that produces the best fit, we test two hypotheses

$$
\begin{aligned}
X^2 &\leq \chi^2 \left(1 - \alpha; DOF\right) : \text{Conclude } H_0 \\
X^2 &> \chi^2 \left(1 - \alpha; DOF\right) : \text{Conclude } H_1,
\end{aligned}
\tag{2.23}
$$

with a level of significance, α, and the degrees of freedom determined by the number of bins selected for the distribution [36].

We first use (2.12) to find the estimated PMF for a given value of $\bar{K}$ and $\mathcal{M}$. We can then form an experimental PMF by first scaling and then taking a histogram of the measured data. Both the scaling factor and $\mathcal{M}$ will be varied over a predetermined range. Our research has shown that the change in the non-rejection region with increasing scale factor values is similar to a decaying exponential. For scale factors below the true value we get high predictions for $\mathcal{M}$. However, as the scale factor approaches and then exceeds the true value, the non-rejection region begins

to stabilize. Upon conducting numerous simulations, our hypothesis appears to be confirmed in that the true value of $\mathcal{M}$ is generally centered within the non-rejection region once it stabilizes. This allows us to narrow down the potential combinations of scale factor and coherence parameter significantly.

It should be noted at this point, that the primary goal of this calibration procedure is to get reasonably close to the true values of photon scaling factor and $\mathcal{M}$. Additionally, we wanted to find an acceptable combination of scale factor and $\mathcal{M}$ that made the collected data appear to have a negative binomial distribution. Depending on the scale factor, some deviation from the truth in the estimates with this technique would be expected due to the error associated with scaling also known as quantization error. Further, as observed in Figure 2.2, as $\mathcal{M}$ grows, minor deviations in $\mathcal{M}$ have little impact on the shape of the distribution. Experimental results demonstrate that minor deviations in both the photon scaling factor and $\mathcal{M}$ have minimal impact on the final results produced by the algorithms presented in this dissertation. Once the likely region for $\mathcal{M}$ is identified, we can compare the scaled variance for the measured data according to (2.21) with the theoretical variance according to (2.13).

The following is a demonstration of the aforementioned calibration technique on simulated data. In each of the three simulations, 1000 independent samples with a negative binomial distribution were generated. The data were then divided by the scale factor to represent simulated camera count data. Table 2.3 presents the true and estimated values for scaling and $\mathcal{M}$ for each of the three trials. Figure 2.7

Table 2.3: Scaling and Coherence Calibration Simulation.

True Parameters vs. Estimates				
Trial #	Scale Factor		Coherence Parameter	
	True	Estimate	True	Estimate
1	3	3	150	150
2	2	2.1	250	235
3	5	5.2	200	200

presents the findings from each of the primary steps listed above. For each of the trials, the hypothesis test was conducted for a range of scale factors from 1 - 20 and a range of $\mathcal{M}$ values from 1 - 500. The true value for $\mathcal{M}$ was then chosen from the center of the stabilized non-rejection region. Using this value for $\mathcal{M}$ we also show the point of intersection between the theoretical variance and the measured variance for observations over a range of scale factors. The estimated scale factor to convert camera counts to photons is the point of intersection.
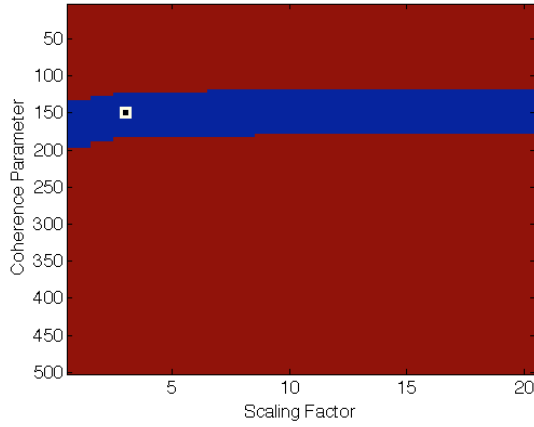
(a) scale factor $= 3$, $\mathcal{M} = 150$
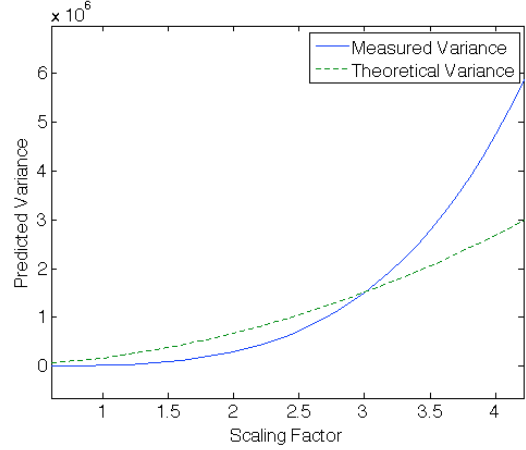
(b) scale factor $= 3$, $\mathcal{M} = 150$
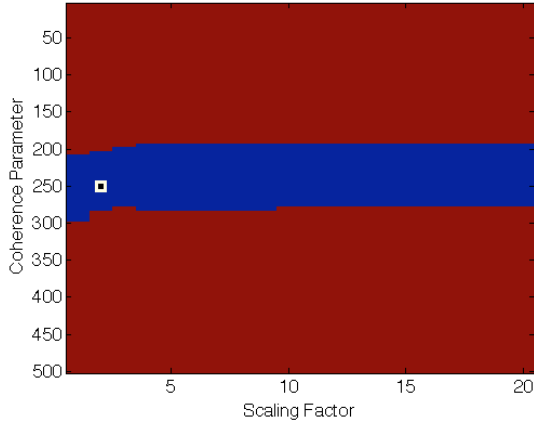
(c) scale factor $= 2$, $\mathcal{M} = 250$
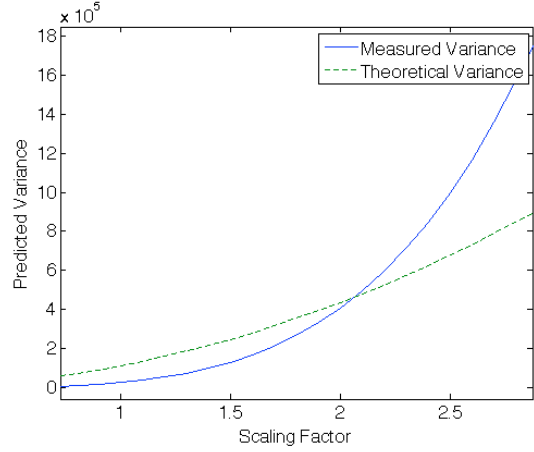
(d) scale factor $= 2$, $\mathcal{M} = 250$
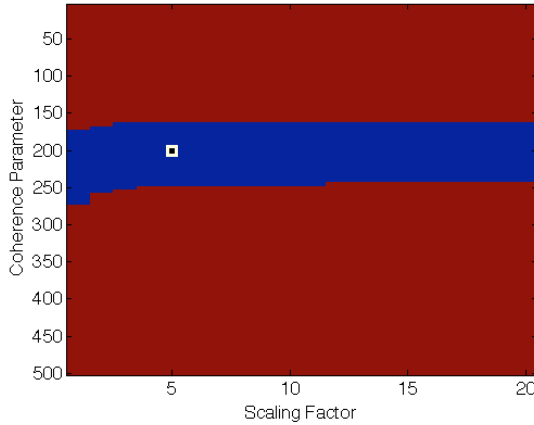
(e) scale factor $= 5$, $\mathcal{M} = 200$
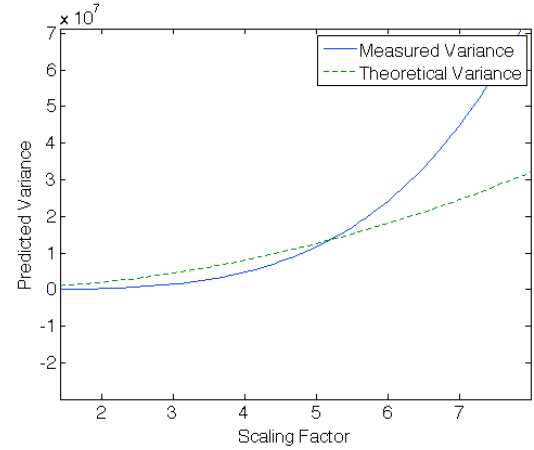
(f) scale factor $= 5$, $\mathcal{M} = 200$

Figure 2.7: **In this demonstration, the regions in red are where the null hypothesis can be rejected. The regions in blue are where we fail to reject the null hypothesis. The white box indicates the scale factor and $\mathcal{M}$ from which the results are based. The plots on the right hand side show the intersection of the measured variance and theoretical variance for a range of scale factors.**

34

Experimental measurements generally consisted of 144 3-D images. Based on the simulations presented in Figure 2.7 and the limited number of samples available, we expected a wider non-rejection region as shown in Figure 2.8(a). However, we were able to find a reasonable range for $\mathcal{M}$ that had negligible impact on the overall results. Based on the simulation results, we expect that more samples might enable a tighter bound on the prediction. Unfortunately, the time required to collect this data would likely introduce additional inconsistencies in the data that would need to be addressed. Based on the results in Figure 2.8, we expect that the camera is

(a) Hypothesis Test Results   (b) Scale Factor Estimation
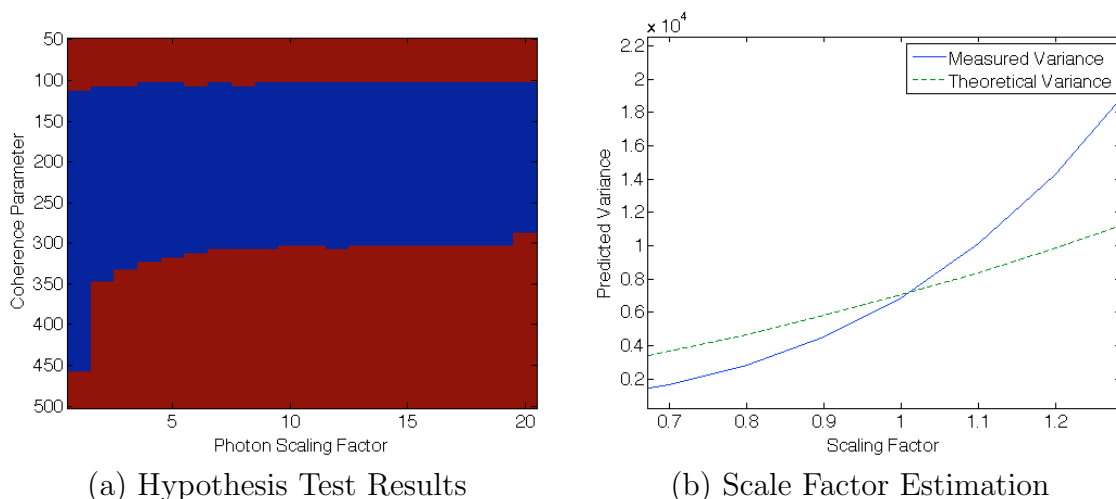
Figure 2.8:   Hypothesis test performed on data collected with ASC 3-D FLASH LADAR sensor. Data exhibits a similar trend to what was shown in simulation. The regions in red are where the null hypothesis can be rejected. (a) The non-rejection region appears to stabilize centered on a coherence parameter of 195. (b) Given a coherence parameter of 195, the scale factor is approximately 1.

a photon counting device with a $\mathcal{M}$ of approximately 195. Varying the value of $\mathcal{M}$ from 100 to 300 will vary the scale factor from 1.3 to 0.8 respectively. However, in all cases where we fail to reject the null hypothesis, the collected data exhibit negative binomial characteristics with the specified scaling and coherence parameter.

As a final note, it would likely be preferential to calibrate the sensor during the design process. For instance, the detector could be calibrated with incoherent illumination and a separate calibration could be performed on the coherence of the

laser illuminator. The technique described above using the χ^2 test should be effective in scenarios where prior calibrations are not available. However, caution must be exercised to avoid distorting the variance measurements due to imperfect image registration. Any registration errors will cause a spike in the measured variance as shown in Figure 2.6 at the edge of the step target. Therefore, we want to make our calibration measurements near largely uniform areas within the target.

2.4　Iterative Algorithm Stopping Criteria

A common challenge with iterative algorithms and a topic that has generated a significant amount of recent research involves the selection of a stopping criteria [2], [12], [19], [56]. The research conducted by MacManus and presented in Chapter III depended primarily on the stopping criteria to arrive at an estimate for Fried's Seeing Parameter, r_0. In the multi-surface ranging algorithm detailed in this dissertation, a key feature is the ability to maximize likelihood for the correct value of r_0. However, since likelihood will increase with each iteration even if the wrong value of r_0 is selected, we may find situations where likelihood is higher for a fixed number of iterations with the wrong r_0 than it is for the correct value of r_0. This likely has to do with the rate at which the algorithm converges. Based on experience with the algorithms, higher values of r_0 generally allow faster convergence than lower values. However, if the algorithm is allowed to iterate for too long, we can distort the results.

In the algorithms employed for both 2-D and 3-D parameterized blind deconvolution, the model for the received image considered a mean intensity convolved with a PSF and further degraded by some additive amount of noise. We can solve for the mean level of this noise. However, if the iterative algorithms are not stopped at the appropriate time, the estimates for image intensity will ultimately be distorted by trying to fit an estimate to the noise. This research will employ a Convergence of Variance (CoV) technique for the stopping criteria. This technique has been employed in similar research in the past with success [45], [48]. The data model is provided in Figure 2.1. Given this relationship, iterations will continue until the MSE between the collected data and the image estimate is lower than the estimated data variance. For a 3-D image this criteria can be represented as

$$\sum_{k=1}^{K} \sum_{u,v=1}^{M} \left(d\left(u,v,r_k\right) - I\left(u,v,r_k\right) \right)^2 < \sum_{k=1}^{K} \sum_{u,v=1}^{M} V\left(u,v,r_k\right), \qquad (2.24)$$

where V is the estimated data variance. At this point we can assume that any further iterations would only serve to fit the estimates to the noise, invalidating the model used.

Multiple techniques exist for identifying the estimated data variance. First of all, we could directly compute the variance if we have a series of images taken of the same scene. Alternatively, if the sensor can be accurately calibrated and we have an understanding of the nature of the light being detected, we can mathematically predict the estimated data variance. Given a partially coherent illumination source, the noise in the images will likely be dominated by speckle noise where the image variance can be accurately modeled with the negative binomial PDF [58]. Therefore, the expected variance for each image pixel and range slice would be

$$V_{NB}\left(u,v,r_k\right) = d_{NB}\left(u,v,r_k\right)\left[1 + \frac{d_{NB}\left(u,v,r_k\right)}{\mathcal{M}}\right], \tag{2.25}$$

where

$$d_{NB}\left(u,v,r_k\right) = d\left(u,v,r_k\right) - B\left(u,v\right). \tag{2.26}$$

Further refinement can be given to this model when the variance of the detector bias is also considered. In FLASH LADAR, detector bias can be measured by taking images without firing the laser and is generally modeled with the Poisson PMF [58]. Therefore the overall variance would be

$$V\left(u,v,r_k\right) = B\left(u,v\right) + V_{NB}\left(u,v,r_k\right). \tag{2.27}$$

The actual distribution of the variance will be sensor dependent; however, the model in (2.27) accurately approximated the variance of the calibrated 3-D FLASH LADAR sensor used for the experimentation in this research.

2.5   Seeing Parameter Measurement from Collected Imagery

In Figure 2.9 we demonstrate the ability to measure r_0 by measuring the step response from the collected image. The impulse response is then found by taking the derivative of this measured step response. Once we have the impulse response we can vary r_0 per the relationship in (2.9) to find the theoretical total OTF that minimizes the error between the measured impulse response and the theoretical impulse response. This demonstration was accomplished by blurring a perfect step target with an average short exposure OTF using an r_0 of 0.0015m.
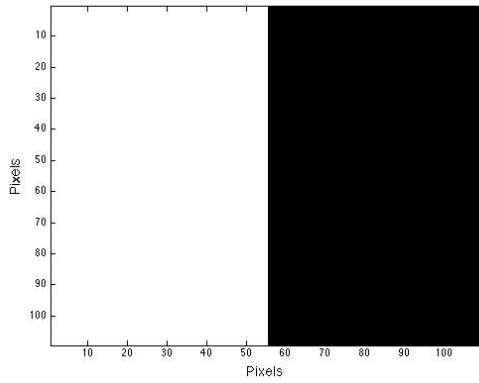
(a) Step target without blur
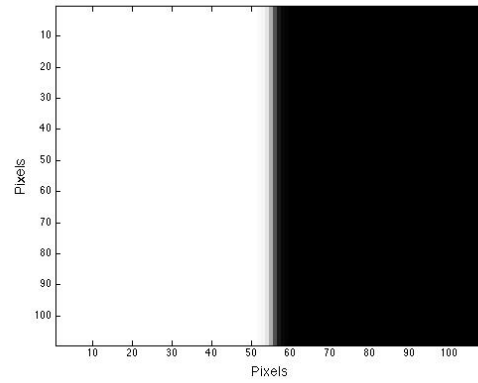
(b) Blurred step target
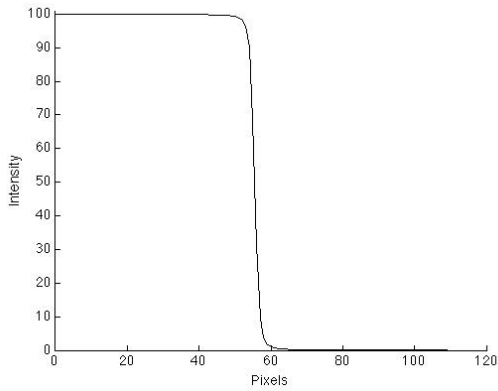
(c) Step response
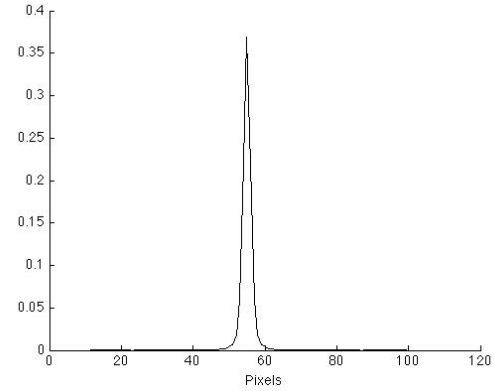
(d) Impulse response
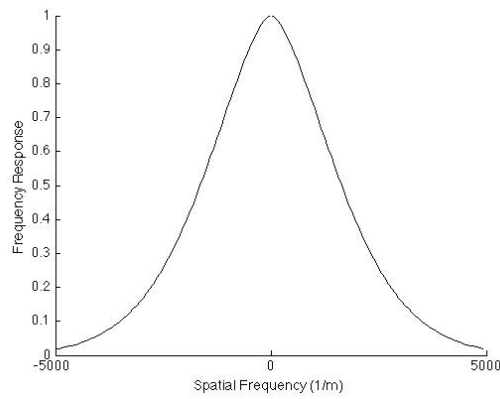
(e) Measured frequency response

Figure 2.9: **(a) Step target without any blur. (b) Step target blurred using a short exposure OTF with an r_0 of 0.0015m. (c) Measured step response by looking at the horizontal change in intensity. (d) Impulse response computed by taking the first derivative of the step response. (e) Frequency response computed by taking the Fourier transform of the impulse response.**

2.6 Previous Research

The following section will summarize and contrast previously published research on topics pertaining to this dissertation. On the specific topic of parameterized blind deconvolution with multi-surface ranging, no other research could be found. However, this dissertation levied ideas from several sub-topics in the final formulation of the overarching research goal.

2.6.1 Blind Deconvolution.

The importance of image deblurring is evident based on the wealth of research conducted on the topic of blind deconvolution. Due to the ill-posed nature of blind deconvolution with 2-D images, it is mathematically impossible to directly solve for the PSF impacting collected images when noise is present [38]. Despite this hurdle, numerous algorithms have been developed to circumvent these mathematical challenges with considerable success by making various assumptions or approximations [5], [11], [25], [35], [37], [61], [60], [64] and [68]. While the problem can be extremely challenging with 2-D images, Millane et al. realized that working with 3-D images presented the potential to reduce common constraints such as sensor sampling requirements and convergence time on iterative algorithms [49].

Complexity of the algorithm, applicability to certain classes of blurring functions and the time required to perform the necessary operations are common concerns associated with blind deconvolution algorithms. Kundur and Hatzinakos authored a pair of articles that provide an exceptional summary of the challenges associated with blind deconvolution and the various strategies commonly employed [33], [34]. The articles highlighted numerous considerations for image processing applications that will directly affect this research. First, due to the ill-conditioned nature of the problem, small perturbations in the received data can lead to large deviations in the

estimates produced by various algorithms. As an extension to this concept, noise amplification is especially likely [15]. This research reduces the issues associated with noise amplification through selection of an iterative algorithm stopping criterion based on noise variance, and application of a constraint on the amplitude. Another common issue with blind deconvolution is that multiple solutions are likely to exist [4], [29]. This research will minimize the chances for convergence to an undesirable solution through educated initialization and applied constraints.

In many remote sensing applications, processing time and complexity are the primary design considerations for an algorithm. As an example, the APEX method is a non-iterative, blind deconvolution technique that can enhance certain classes of imagery in near real time [8], [9]. The technique operates on a restricted class of blurs, in the form of 2-D radially symmetric, bell-shaped, heavy-tailed probability density functions. While this technique is very effective on certain classes of imagery, it does not provide an estimate of r_0 as given in the CoV technique. A comparison of this work to the CoV technique was provided in [45]. As previously mentioned, the ability to recover r_0 has applicability beyond the primary focus of conducting blind deconvolution.

The work reported on in [10] and [17] is significant because it shows the value of the Richardson-Lucy (RL) Filter for iteratively deblurring images. Variations on this technique are employed throughout this research in conjunction with OTFs parameterized by r_0. One technique for simplifying this problem considers a parameterization of the OTF [41], [43] and [45]. This work will extend the concepts presented by MacDonald and MacManus to show that working with 3-D images presents new opportunities that were previously mathematically ill-posed as theorized by Millane [49].

The parameterized OTF is chosen to simplify the structure of the unknown blur-

ring function to a certain class of atmospheric models. The goal of this simplification is to make the algorithm more suitable for implementation in a tactical environment where near-real-time operation is required. When using MCFA compilations of images where each individual image has an exposure time of less than $\frac{1}{100}$ of a second, the average short-exposure OTF, $\bar{H}_{SE}$, is reduced to a function of a single unknown parameter, Fried's seeing parameter, r_0, as shown in (2.10). A similar average OTF has been discussed for the long exposure case (2.11) as well. While there are benefits to using long-exposure imaging in certain scenarios such as astrophotography, the loss of frequency content is often an undesired side-effect. In a tactical military scenario or any other dynamic environment, it would be impractical if not impossible to point a sensor at a target long enough to warrant the use of long-exposure imaging.

Figure 2.10 compares the frequency response that is diffraction limited, to the frequency response considering a long and short-exposure OTF for two levels of atmospheric seeing. It is evident from a frequency content standpoint that there are inherent benefits with using properly registered short-exposure images. The parameters for this demonstration were chosen to match those in Table 2.1 that will be employed to obtain the experimental results shown in Chapter III. As expected, the short-exposure OTF is very close to the diffraction limited OTF when $r_0 = 5$ cm. However, the long-exposure OTF reveals a significant attenuation in high frequency content. Higher levels of turbulence yield a higher loss in frequency content for the long-exposure scenario, and significant attenuation of high frequency content for the short-exposure scenario as shown in Figure 2.10(b).

One of the primary benefits associated with parameterized blind deconvolution is computational efficiency. While the most significant improvement is realized through deconvolution with the actual instantaneous OTF, simultaneously computing the instantaneous OTF and deblurring an image is computationally intensive. However,

(a) OTF Comparison for r_0=5 cm   (b) OTF Comparison for r_0=2 cm
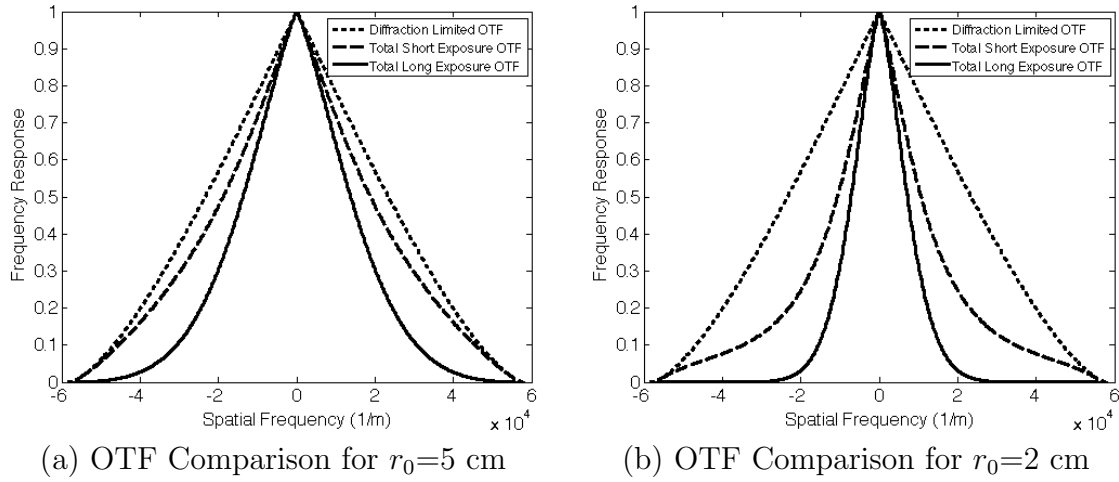
Figure 2.10: **(a) Comparison of the frequency response for this sensor given a D/r_0 ratio of 1. (b) Comparison of the frequency response for this sensor given a D/r_0 ratio of 2.5.**

this research will show that deconvolution with an average theoretical model for the OTF can produce significant gains in image quality while reducing the computational burden. Additionally, in scenarios where the average atmosphere remains relatively constant, the problem can almost be treated as a deconvolution problem rather than a blind deconvolution once the initial parameterized blind deconvolution is completed.

2.6.2 Multiple Surface Ranging.

Variations of LADAR technology have proven useful in a myriad of civilian and military applications. Common civilian uses are 3-D mapping of surfaces, autonomous vehicle navigation and forestry classification. Military applications include tasks such as targeting and autonomous aerial refueling. Current military application may be limited due to sensor capability; however, as the technology improves, additional emphasis will be given to incorporating LADAR onto new or existing platforms. Previously conducted research and the demonstrated ranging accuracy of LADAR systems have forged an interest in a myriad of defense applications.

Currently there is a significant desire within the Department of Defense (DoD) and

44

DHS to employ a 3-D imaging sensor. Provided spatial resolution can be improved to be comparable with currently employed passive sensors, 3-D FLASH LADAR technology is a likely successor. One of the primary motivators for this move is that previous simulations and experiments with both ALS and FLASH systems have demonstrated the ability to image through foliage canopies, camouflage netting or various other obscurations.

In LADAR imaging, a common method for obtaining the ranges to multiple surfaces per detector is to fit a Gaussian mixture (2.2) to the received pulse through the use of various techniques such as an EM algorithm [6], [27], [55] and [67]. Hernández et al. developed a multiple surface ranging algorithm that relied on reversible jump Markov chain Monte Carlo techniques [24]. While their work shows great promise for many applications, the complexity of the algorithm does not lend itself to near real time image processing. Additionally, most algorithms operate on each pixel in isolation and do not consider the spatial or temporal effects from interaction with neighboring surfaces. While the techniques may give additional insight to candidate ranges for an image, depending on the severity of the diffraction effects, the surfaces visible in the collected data may vary significantly from reality. The primary goal of this portion of the research was to develop an EM solution which could accurately discriminate the range to multiple true surfaces per pixel while discarding false returns due to diffraction. Since we are considering statistical independence for each detector in the APD array, and the received pulse is a composition of temporally displaced Gaussians, ideas and techniques for pulse estimation can be leveraged from numerous other disciplines. Gaussian decomposition has applications in nearly any case where the collected data can be decomposed into numerous subsets, each with an approximately normal distribution.

Fortunately Gaussian decomposition or mixture modeling is studied a great deal

in the literature, but numerous challenges are commonly cited with reference to developing an estimator for the Gaussian mixture. Expectation Maximization (EM) is a common technique employed to isolate the parameters of interest in the received data [24], [46]. Zhuang points out that common challenges are employing estimators when the number of components in the mixture are unknown, or when mixture components may merge due to their individual parameters [69]. Vlassis and Nikas approached the first problem with a greedy EM technique. They performed an iterative process where the number of components was incrementally increased until the number corresponding with the solution with the highest likelihood was obtained [66]. With 3-D FLASH LADAR, this process could be extremely time consuming as the number of components grows, therefore making this an impractical solution for this work. Rather, this research will propose the establishment of an upper bound, and then refining the estimate based on pulse parameter estimates.

The approach employed for multi-surface ranging is similar to the EM approach derived by Dolce for fusing 2-D and 3-D LADAR data [16]. However, the work is not equivalent because Dolce's work does not account for the possibility of multiple surfaces per pixel, nor does it provide an estimate for the pulse amplitude or pulse width. Dolce's algorithm was only concerned with a single pulse detector. For this reason, he was able to use the amplitude received from the Richardson-Lucy deconvolution of the 2-D image. However, since we would like to solve the problem where multiple surface returns may be received by each detector, we will not have that luxury. An interesting topic for future research would be to combine the work presented in this dissertation with the work conducted by Dolce.

A considerable amount of previous research focused on LADAR technology has been devoted to enhancing the capability of ALS systems such as in [28], [32], [46] and [63]. One advantage for ALS sensors, is that their spatial resolution is primarily

determined by the system's ability to finely scan over the target area and accurately reconstruct the received pulses into an image. Mallet and Bretar provide a good summary of various techniques and successes that have been realized with this technology with respect to multiple surface ranging [46]. Unfortunately, ALS systems commonly require a considerable amount of time to form an image, and the targeted scene must remain fairly constant during the imaging period. In addition to the constraints on the targeting area, ALS sensors also suffer from added complexity due to the requirement for a tracking and stabilization system. As pointed out by Halmos, one of the primary driving factors for the interest in FLASH systems is that "size can be dramatically reduced by eliminating the stabilization subsystem that can be a large part of the LADAR implementation cost and size" [23].

As 3-D FLASH technology improves, the benefits of ALS systems without the detractors may be possible. In addition to the research tailored specifically to ALS systems, the following work has been devoted to multiple surface ranging with FLASH or hybrid systems. By gathering polarization information from various surfaces in conjunction with 3-D FLASH LADAR data, Murray demonstrated that multiple surfaces could be discerned. Additionally, the undesired obscuration could be discarded based on *a priori* knowledge of the polarization of the desired surface [50]. In addition to the more common imaging through camouflage applications, Gelbart et al. used a FLASH system to image through ocean environments to demonstrate the ability to detect sea mines or obstructions that may impact a beach landing. Gelbart ascertained the number of surfaces in the received data by counting the zero-crossings of the first derivative of the received pulse [18]. An observation in common with both efforts was that the spatial resolution for collected images was poor due to hardware limitations and complexity of the detector array. As a proof-of-concept, the JIG-SAW LADAR sensor developed for the Defense Advanced Research Projects Agency

(DARPA) used a hybrid of both FLASH and ALS technology. By scanning with an 8×128 detector array, the sensor could rapidly obtain a 304×256 3-D image [40]. While the spatial resolution of this system was an improvement, the added complexity and increase in hardware associated with tracking and image stabilization would likely limit the technique's utility for many applications where size is an important design consideration.

The previously mentioned research highlights the potential advantages of employing 3-D LADAR or more specifically 3-D FLASH LADAR on future sensor platforms. Common among each of the previously mentioned efforts is the lack of addressing the effects of imaging through a turbid medium. The techniques and associated systems have demonstrated the ability to identify multiple surfaces per detector. However, no previously developed algorithm has been identified that accounts for the spatial mixing associated with the lowering of the spatial frequency cutoff, and how it impacts multi-surface ranging. As sensors improve in maximum attainable spatial resolution, this impact will only become more pronounced.

2.6.3 3-D FLASH LADAR Image Enhancement.

Recent work conducted at Utah State University focused on improving the ability to perform Automated Target Recognition (ATR) with 3-D LADAR images [54]. The focus of this research was to use post processing techniques to enhance the resolution of surface edges through multi-surface ranging techniques. While the focus of the research has similar goals, there were several underlying assumptions that reduce the applicability to the specific problems being addressed in this dissertation. Perhaps the most difficult assumptions to overcome are, that the range, intensity, and pointing direction of each return was known and that the surfaces were assumed to have constant reflectivity and a Lambertian bi-directional reflectance distribution

function.

Likely the most similar research to what is presented in this dissertation was produced by McMahon [47], [48]. McMahon's work was the only previous research that could be found with a focus on improving or restoring the images collected through blind deconvolution. He found that by using the range diversity present in 3-D FLASH LADAR images, he could simultaneously solve for the instantaneous OTF and an enhanced model for the 3-D image. Several differences exist between his research and what is presented in this dissertation. First and foremost, McMahon's work only accounts for a single surface per detector. He ultimately proposes the topic of multi-surface ranging as future research. Additionally, he produces estimates for the instantaneous OTF rather than the parameterized average OTF. While this technique has application where post-processing can be conducted, it is likely too complex to be conducted in a near real time fashion.

Based on the similar structure of the iterative algorithm developed by McMahon [48] and the Multi-Surface Including Diffraction (MSID) algorithm presented in Chapter IV, we can compare rough estimates on the computational power required for each iteration. Likely the most complex mathematical component in each algorithm is the computation of the 2-D Fast Fourier Transform (FFT) or 2-D inverse Fast Fourier Transform (iFFT). The remaining operations are simply pixel-by-pixel additions, multiplications and divisions. The 2-D FFT can be used to efficiently perform convolution by multiplying the 2-D FFT of both components and then taking the 2-D iFFT of the result. Similarly, the use of 2-D FFTs and iFFTs can also be used to speed up the correlation operations throughout the algorithms by also taking the complex conjugate of one of the two components. Given the solutions for the pulse shape, PSF, gain and bias derived by McMahon [48], each iteration will take three 2-D iFFTs, and six 2-D FFTs. For each level of seeing tested, an iteration of the MSID

algorithm can be completed with just two 2-D iFFTs, and two 2-D FFTs. This results in a roughly 56% decrease in processing time per iteration for the MSID algorithm. As we will discuss in Chapter V, parameterized blind deconvolution in conjunction with the MSID algorithm is performed in a search routine. However, with the use of parallel processing and enough available processing threads, the search routine could be accomplished in roughly the same time that a single level of atmospheric seeing could be tested.

A final contrast with the research conducted by McMahon is that his work does not produce direct estimates for all of the pulse parameters. Rather, he produces a refined estimate for the pulse, and then employs a ranging algorithm separately. Despite the differences, McMahon's work established a solid foundation from which the research in this dissertation is derived.

III. Convergence of Variance for Seeing Parameter Estimation

In this chapter, two previously developed image reconstruction algorithms are presented that will remove the effect of atmospheric turbulence on 2-D images. While neither of the algorithms presented in this chapter are novel, this chapter will consist of an expansion upon previous findings and a discussion / demonstration of the potential challenges with applying the techniques to 3-D imagery. The primary focus of this portion of research was to identify a blind deconvolution technique that could be employed in a tactical military environment where both time and computational power are limited. Additionally, the following techniques have application in the measurement of atmospheric seeing conditions. In a blind deconvolution fashion, the algorithms simultaneously compute a high resolution image and an average model for the atmospheric blur parameterized by Fried's seeing parameter.

Convergence of Variance (CoV) presented in Section 2.4 as a stopping criteria has been incorporated with success in various blind deconvolution algorithms [44], [48]. MacManus later demonstrated that CoV by itself allowed for identification of the best model for the PSF parameterized by r_0 [45]. The novelty in his approach was that it did not assume a *prior* distribution for the seeing parameter, rather it assessed the convergence of the image's variance as the stopping criteria and identification of the proper seeing parameter from a range of candidate values. Experimental results show that the CoV technique allows for estimation of the seeing parameter accurate to within 0.5 cm and often even better depending on the signal to noise ratio.

This chapter is organized as follows: Section 3.1 presents background material on image deconvolution and the challenges associated with blind deconvolution, in Section 3.2 the two techniques will be compared on a variety of artificially blurred images,

Section 3.3 demonstrates the value of the CoV technique on actual collected imagery and Section 3.4 presents considerations and challenges associated with extending this technique to 3-D imagery.

3.1   Image Deconvolution

The process of deconvolution is commonly performed on collected images, i, that are degraded by a PSF and noise. The goal of the process is to recover the true representation of the remote scene. The notation for the image model in this chapter will differ slightly from Chapter II. In this chapter we are primarily concerned with 2-D images. In the 2-D case, the model for the received data, d, is the convolution of the remote object, o, with the PSF, h, with an additive amount of noise, n, as shown in

$$(o \otimes h) + n = d. \tag{3.1}$$

For the 2-D case, we are simply accounting for a received intensity during the detectors integration time rather than trying to account for the entire pulse shape reflected off of the remote scene. As previously mentioned, there are a plethora of algorithms designed to aid in this problem. Perhaps the most widely accepted or recognized algorithm for image deconvolution when the collected images follow a Poisson distribution is the RL algorithm.

3.1.1   Richardson-Lucy Deconvolution Algorithm.

One of the key benefits of the RL algorithm,

$$\hat{o}\,(x,y)_{new} = \hat{o}\,(x,y)_{old} \sum_u \sum_v \frac{d\,(u,v)}{I\,(u,v|\,r_0)} h\,(u-x, v-y|\,r_0), \tag{3.2}$$

where

$$I\left(u, v \left| r_0\right.\right) = E\left[d\left(u, v\right)\left| r_0\right.\right] = \sum_x \sum_y \hat{o}\left(x, y\right) h\left(u - x, v - y \left| r_0\right.\right), \qquad (3.3)$$

for a wide variety of imaging applications in the presence of Poisson statistics, is that if the algorithm converges, it will converge to the MLE [39], [62]. In (3.2), $\hat{o}$ is an estimate for o and I is the expected value of the intensity received at each detector pixel given a specific PSF. Since (3.2) is an iterative algorithm dependent upon previous estimates for the image, $\hat{o}\left(x, y\right)_{old}$, we must provide some sort of initialization to the algorithm. Typically, the initial value for the image estimate is just set to equal the collected data.

A commonly cited drawback to the RL algorithm is the noise amplification that occurs as the number of iterations increases [10], [15]. Noise amplification is a common problem with iterative ML algorithms where the algorithm is attempting to fit the estimate to a particular distribution as closely as possible. Therefore, we must stop iterations before noise amplification occurs. Clearly this could be accomplished interactively by the user; however, for an automated or blind routine, any required user interaction would be undesirable. The method proposed in this work will rely on the convergence of the estimate of the noise power and the predicted variance of the collected data to cease iterations.

3.1.2 Blind Estimate of Seeing via Maximum a Priori Technique.

The idea of using the RL algorithm in a blind fashion to de-blur an image was previously presented by Fish et al. [17]. However, their work did not employ the theoretical models for the long and short-exposure transfer functions parameterized by r_0 [21]. Perhaps the most similar work to this portion of the research was accomplished by MacDonald. He developed a blind technique that was iterative in nature like the

RL algorithm, yet he considered *a priori* information for images distorted by speckle noise following more of a negative binomial distribution [44]. MacDonald considered *a priori* information for the distribution of r_0 in hopes of maximizing the likelihood at the appropriate level of seeing.

Assuming the collected image can be approximated with the Poisson PMF, and if we assume independence of the measurements for every pixel in the detector array, we can state the joint probability of the observed noisy image, i, as

$$p\left[I = d\left(u,v\right); \forall\left(u,v\right)\right] = \prod_u \prod_v \frac{I\left(u,v\left|r_0\right.\right)^{d(u,v)} e^{-I(u,v|r_0)}}{d\left(u,v\right)!}. \qquad (3.4)$$

Ideally, we would like to maximize the likelihood or log likelihood

$$L\left(r_0\right) = \sum_u \sum_v \left[d\left(u,v\right) \ln\left[I\left(u,v\left|r_0\right.\right)\right] - I\left(u,v\left|r_0\right.\right) - \ln\left[d\left(u,v\right)!\right]\right], \qquad (3.5)$$

over a range for r_0 to identify the appropriate PSF. Unfortunately, likelihood continually increases with r_0 as illustrated by the following example in Figure 3.1. While the RL algorithm maximizes likelihood for a given PSF, the ML solution over a range of r_0 values does not necessarily occur when the correct PSF parameterized by r_0 is chosen. This is the direct problem that MacDonald sought to solve by introducing *a priori* information for the distribution of r_0.

(a) Original Image
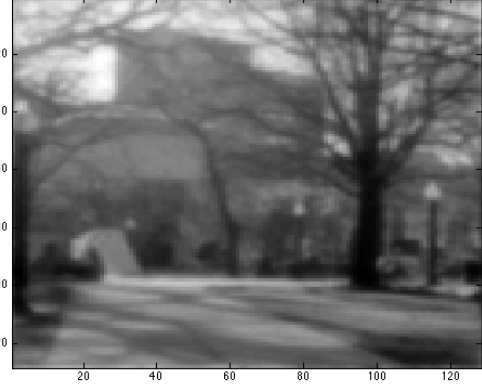
(b) Blurred Image (r_0=2.5 cm)
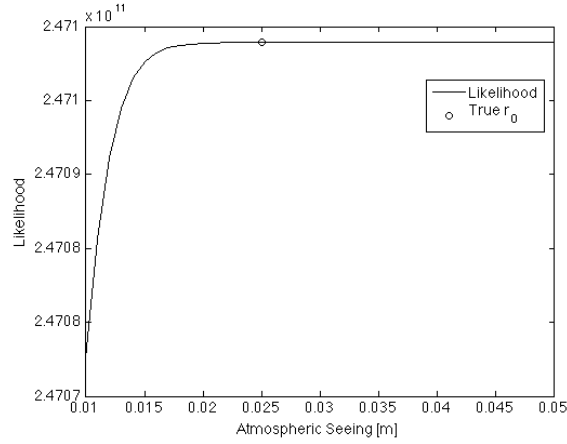
(c) Log Likelihood

Figure 3.1: (a) The original image without the added effects of atmospheric blurring. (b) The image that would be received by a sensor with the specifications listed in Table 3.1 given an r_0 of 2.5 cm. (c) Likelihood as a function of r_0. Zooming in on the plot of likelihood vs. r_0 will show a gradual increase in likelihood with increasing r_0.

MacDonald hypothesized that a distribution could be applied to the value for r_0 based on the intuitive observation that the seeing is seldom extremely better than the average and can often be worse. The form of the probability density function for the random parameter r_0 was assumed to be

$$f_{R_0}(r_0) = \left[\frac{e^{-M^2(r_0/r_{avg})}}{r_{avg}/M^2} \right], \tag{3.6}$$

where r_{avg} is the average atmospheric seeing, and M^2 is the number of pixels in the detector array. In situations where r_{avg} is unknown, we initialize the value to be equal to the aperture diameter [41]. We can then execute the likelihood maximization strategy produced by MacDonald. If the value of r_0 that maximizes likelihood is less than the initialized value for r_{avg}, we set the value of r_{avg} to the new r_0 estimate and recompute the estimate for r_0. We continue this process until the estimate for r_0 is equal to r_avg. When applying this technique to the example illustrated in Figure 3.1, we see that likelihood is maximized near the correct value of r_0 as shown in Figure 3.2. While the technique is successful in this scenario, two mathematical

(a) Prior for r_0 (b) Log Likelihood Using the Prior for r_0
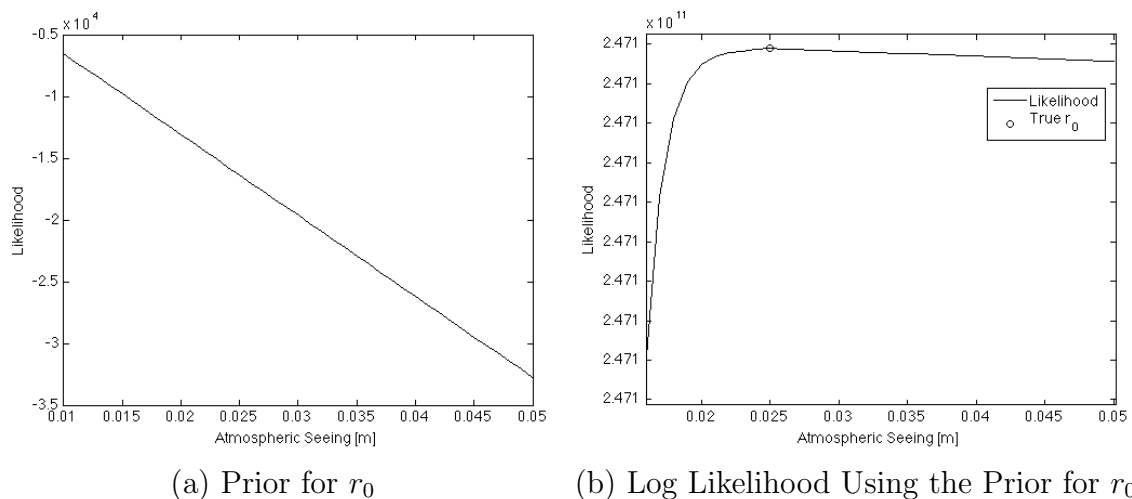
Figure 3.2: **(a) Log likelihood of the exponential prior as a function of r_0. (b) Overall log likelihood with the addition of the prior. With the addition of the prior, likelihood is maximized for the correct value of r_0.**

challenges remain. First, the choice of an exponential distribution for r_0 is probably inaccurate. Extremely low values of r_0 are expected to be nearly as unlikely as high values. Second, the effect of scaling the exponential density function by the number of pixels in the detector array is difficult to justify for partially illuminated scenes such as astronomical images. The CoV technique will remove the requirement for the *prior* distribution on r_0 and allow us to directly converge to the correct value.

3.1.3 Blind Estimate of Seeing via CoV Technique.

The CoV technique works on the premise of searching for the best possible PSF parameterized by r_0 in the amount of time available for processing. Given more time, the technique will provide a more refined estimate for r_0. We will first explain this technique in more detail using the assumption that the images collected follow the Poisson model. Later we will demonstrate the technique using images that follow a negative binomial noise model. Ultimately, the technique should work regardless of the noise distribution assuming the correct iterative deblurring algorithm and convergence criteria are used.

This technique relies on detecting the point where the MSE between the collected data and the image estimate is lower than the estimated data variance. At this point we can assume that any further iterations would only serve to fit the estimates to the noise. In other words, for 2-D images, iterations would cease when

$$\sum_u \sum_v \left(d\left(u,v\right) - I\left(u,v\right) \right)^2 < \sum_u \sum_v V\left(u,v\right), \tag{3.7}$$

where V is the actual image variance. Assuming the collected MCFA follows Poisson statistics, the deblurring algorithm employed would be the Richardson-Lucy algorithm in (3.2), and

$$V\left(u,v\right) = d\left(u,v\right). \tag{3.8}$$

The relationship in (3.8) is allowed since the assumption can be made that the intensity captured by each detector is independent of other detectors, and each intensity can essentially be thought of as an independent Poisson random variable. The summation of these random variables is therefore a good approximation for the total image variance.

Due to the photon counting nature of many imaging applications, the Poisson distribution is often employed as a statistical distribution for the detected images. However, due to the highly coherent nature of laser light, images detected by a LADAR sensor often follow more of a negative binomial distribution. Fortunately, the robustness of the CoV technique allows for employment in this scenario as well. MacDonald derived an iterative MLE where the noise is dominated by laser speckle as

$$\hat{o}\left(x,y\right)_{new} = \hat{o}\left(x,y\right)_{old} \frac{\sum\limits_{u}\sum\limits_{v}\left(\frac{d(u,v)}{I(u,v|r_0)}h\left(u-x,v-y|\,r_0\right)\right)}{\sum\limits_{u}\sum\limits_{v}\left(\frac{d(u,v)+\mathcal{M}}{\mathcal{M}+I(u,v|r_0)}h\left(u-x,v-y|\,r_0\right)\right)}, \qquad (3.9)$$

where $\mathcal{M}$ is the coherence parameter of the light [44]. Using the deblurring algorithm in (3.9), we would again iterate until the relationship in (3.7) is satisfied where

$$V\left(u,v\right) = d\left(u,v\right)\left[1 + \frac{d\left(u,v\right)}{\mathcal{M}}\right]. \qquad (3.10)$$

The diagram in Figure 3.3 demonstrates how this technique could be employed in an operational scenario where processing time and computational power are limited. In this scenario, images are collected and fed into the r_0 estimation process. At any point in time, the best possible estimate for r_0 can be drawn upon for deblurring an image. However, in parallel, the r_0 estimation loop will continue to work on characterizing the current atmospheric seeing conditions. One of the key advantages to this algorithm is that it is easy to parallelize. Even with a common home computer

Figure 3.3: Potential employment scenario for the CoV technique, where the r_0 estimation loop is allowed to continually execute on recently collected images. The most recent estimate for r_0 can then be fed to an iterative deblurring algorithm to provide rapid results to the user.

that has a multi-core processor, it is possible to simultaneously test multiple values of r_0 for convergence. The r_0 to employ in the deblurring algorithm would be the lowest value of r_0 for which (3.7) is satisfied. As MacManus pointed out and as indicated in Figure 3.4, we can also further enhance the process by first conducting a coarse estimate of r_0 followed by a more refined estimate [45]. MacDonald references the employment of a convergence test for ceasing iterations in his algorithm; however, it is apparent that he did not utilize this test as a sufficient criteria for identifying the correct value of atmospheric seeing [41]. As previously mentioned, if allowed sufficient time, the relationship in (3.7) will be satisfied for the correct r_0 and all values higher. Given adequate SNR in the measured images, the criteria will never be attained for low estimates of r_0. The following sections will demonstrate the employment of this

59

Figure 3.4: In this demonstration, the true value for r_0 is 4.3 cm. However, the algorithm first converges at 5 cm using a 1 cm/step course search. It then accomplishes a 0.1 cm/step fine search to converge to the true value at 4.3 cm.

technique on images with Poisson and negative binomial noise to show that *a priori* information is not required to achieve accurate estimates for r_0.

3.2   Simulation

The following results will demonstrate the utility of the CoV technique and compare the results to the MAP algorithm developed by MacDonald for images with Poisson and negative binomial noise. The optical specifications listed in Table 3.1 and used for the simulations were not limited to what could readily be obtained for experimentation. Rather, the specifications were chosen to mimic what could potentially be incorporated into a targeting pod design based on size limitations. The specifications will allow for properly sampled images according to (2.7). We will first consider simulation results using a fully illuminated scene. We will then simulate conditions for astrophotography where the scenes are only partially illuminated.

Table 3.1: Simulated System Specifications.

Parameter Name	Defined Value
Mean wavelength $(\bar{\lambda})$	600 nm
Pixel size	5 μm $\times$ 5 μm
Sensor focal length (f_l)	3 m
Aperture diameter (D)	15 cm
Coherence Parameter (M)	30

3.2.1 Fully Illuminated Scenes.

In this section we will present results from images that are fully illuminated. By fully illuminated, we mean that the overwhelming majority of the scene is not dark, and contains varying levels of contrast. Recall that MacDonald's algorithm defined a *prior* for r_0 of exponential form scaled by the total number of pixels in the detector as shown in (3.6).

In the following examples, the cameraman photo built into MATLAB® is blurred using a total OTF that is the product of the diffraction limited OTF and an average short-exposure OTF with various levels of r_0. Multiple trials will be conducted with MCFA images composed of 1, 10, 20, 30, 50 and 100 individual frames with independent realizations of Poisson noise to demonstrate the effects of SNR on each algorithm. The original, blurred and an example of a recovered image are shown in Figure 3.5. In order to implement MacDonald's algorithm, we either need an initial estimate on the average value for atmospheric seeing, r_{avg}, or we can initialize it to the aperture diameter if no estimate can be made. For purposes of fair comparison, we will assume that no prior estimates are known for atmospheric seeing, and r_{avg} will be initialized to the aperture diameter.

Table 3.2 shows that the CoV technique and MacDonald's algorithm produce nearly identical results with the only exceptions highlighted in bold. MCFA images consisting of more frames take longer to converge due to the higher intensities at each

True Image   Blurred/Noisy Image   Image Estimate
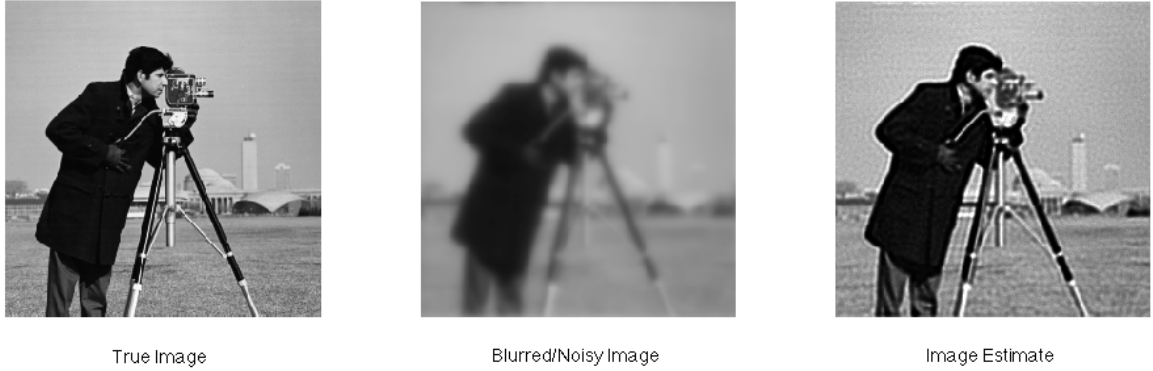
Figure 3.5: **In this demonstration, the true image (left) is blurred with an average short-exposure OTF with an r_0 of 2.6 cm. The blurred/noisy image (center) is the summation of 30 individual frames with independent realizations of Poisson noise. The image estimate (right) was obtained using the best estimate of r_0=2.6 cm with the cap on the number of iterations set to 5000 for the CoV technique.**

pixel associated with the summation of individual frames. While the algorithm does not always converge to the true value of r_0, the estimated value was always within 0.5 cm of the true value. The estimates for r_0 often appear to be lower than the true value, and this is likely due to the algorithm's attempt to remove minor focus errors that were not accounted for when assigning the image as truth data. The PSF arising from minor focus error will blur the image in a way that may not be easily distinguished from an atmospheric blur [70]. Therefore minor focus error could contribute to the low estimates for r_0. Additionally, a large portion of the scene consists of background objects that are likely affected by a lower r_0 than what is in the foreground. Therefore the CoV technique is likely attempting to account for this. This assessment is drawn from and supported by the fact that, provided we have an adequate SNR, the ideally simulated scenes in Section 3.2.2 never converge below the true value regardless of the number of iterations the algorithm is allowed to perform.

Table 3.2: Results for Fully Illuminated Image Simulation with Poisson Noise (True $r_0 = 2.6$ cm). Results in Bold Indicate the Algorithm that Performed Worse for a Particular Scenario

Max Iterations Allowed - 1000					
Frames	SNR (dB)	MAP Estimator (cm)		CoV (cm)	
		Result	Error	Result	Error
1	41.5	2.4	-0.2	2.4	-0.2
10	51.5	2.7	0.1	2.7	0.1
20	54.5	2.8	0.2	2.8	0.2
30	56.2	2.9	0.3	2.9	0.3
50	58.4	3.0	0.4	3.0	0.4
100	61.5	**3.2**	**0.6**	3.1	0.5
Max Iterations Allowed - 5000					
Frames	SNR (dB)	MAP Estimator (cm)		CoV (cm)	
		Result	Error	Result	Error
1	41.5	**2.1**	**-0.5**	2.2	-0.4
10	51.5	2.4	-0.2	2.4	-0.2
20	54.5	2.5	-0.1	2.5	-0.1
30	56.2	**2.5**	**-0.1**	2.6	0
50	58.4	2.6	0	2.6	0
100	61.5	2.7	0.1	2.7	0.1
Max Iterations Allowed - 10000					
Frames	SNR (dB)	MAP Estimator (cm)		CoV (cm)	
		Result	Error	Result	Error
1	41.5	2.1	-0.5	2.1	-0.5
10	51.5	2.3	-0.3	2.3	-0.3
20	54.5	2.4	-0.2	2.4	-0.2
30	56.2	2.4	-0.2	2.4	-0.2
50	58.4	2.5	-0.1	2.5	-0.1
100	61.5	2.6	0	2.6	0
Max Iterations Allowed - 20000					
Frames	SNR (dB)	MAP Estimator (cm)		CoV (cm)	
		Result	Error	Result	Error
1	41.5	2.1	-0.5	2.1	-0.5
10	51.5	2.3	-0.3	2.3	-0.3
20	54.5	2.3	-0.3	2.3	-0.3
30	56.2	**2.3**	**-0.3**	2.4	-0.2
50	58.4	2.4	-0.2	2.4	-0.2
100	61.5	2.5	-0.1	2.5	-0.1

The performance of the CoV technique is based on the quality of the blurred image and the amount of time available for processing. Provided enough time is allowed, (3.7) will be satisfied for the best estimate of r_0. However, allowing too much time does not present a problem for this algorithm. By observing the difference between the left-side and right-side of (3.7) at each iteration, we can update an estimate for the number of remaining iterations required for convergence, EI, using

$$
\begin{aligned}
IV\,(n) &= \sum_{u,v=1} \left(d\,(u,v) - I\,(u,v)\right)^2 \\
BV &= \sum_{u,v=1} V\,(u,v) \\
EI &= \frac{IV(n-1)-BV}{IV(n-1)-IV(n)}
\end{aligned}
\qquad\qquad (3.11)
$$

where n represents the iteration number, BV is the variance of the collected image, and IV is the MSE between the collected images and the non-noisy estimate. Essentially the relationships in (3.11) are used to predict how long the algorithm will have to iterate based on the current rate of convergence [45]. Figure 3.6 demonstrates that when the value of r_0 is too low, the estimated number of remaining iterations diverges.
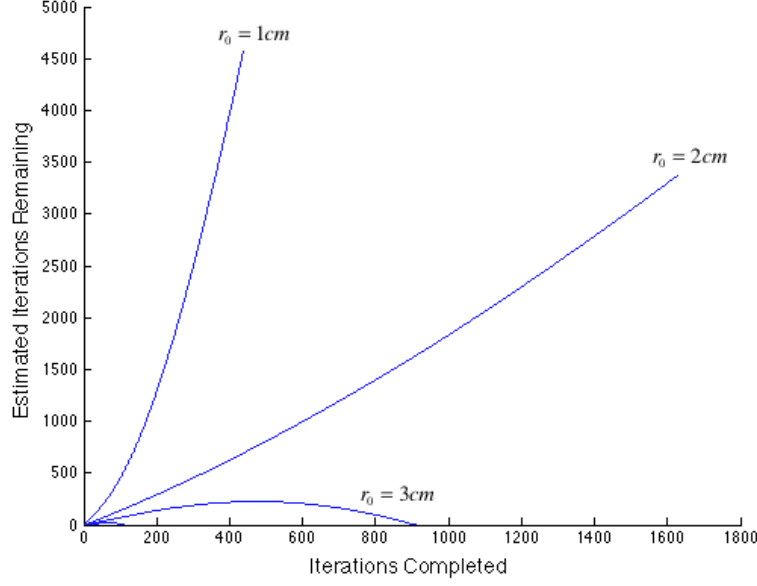
(a) Coarse Estimation for r_0=2.6 cm
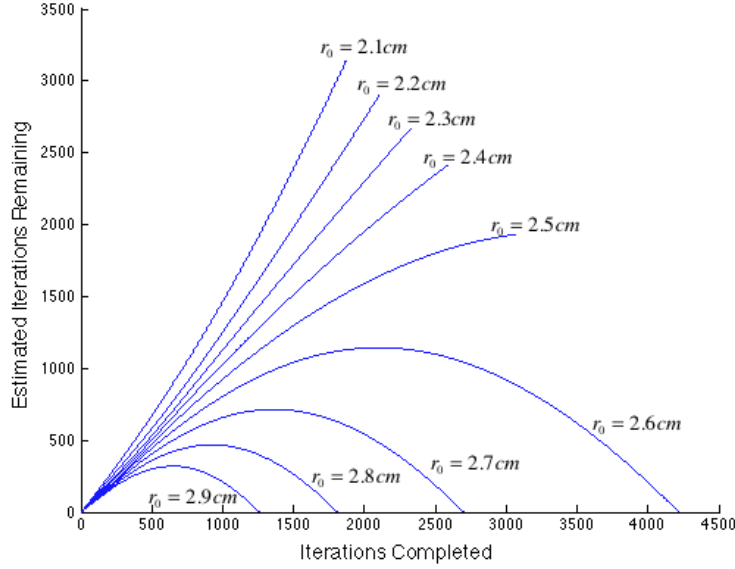
(b) Fine Estimation for r_0=2.6 cm

Figure 3.6: **Estimated iterations remaining for an MCFA image composed of 30 independent frames. (a) Coarse estimation shows convergence for r_0 values greater than 3 cm, but divergence for values of 2 cm or less when the true r_0=2.6 cm. (b) Fine estimation with a cap of 5000 iterations shows convergence for r_0 values of 2.6 cm or greater. Based on experience with this algorithm, it is expected that convergence will occur for an r_0 value of 2.4 cm due to the concave down nature of the curve as supported by the results in Table 3.2.**

We now repeat this experiment in the presence of negative binomial noise to simulate the expected results from laser illuminated imagery. Figure 3.7 again demonstrates the results using an MCFA consisting of 30 frames and a cap on the maximum iterations set to 5000. A close inspection of the blurred/noisy image reveals a significant and visible increase in overall noise variance. As expected, this does impact the final results. Table 3.3 summarizes the results obtained for the CoV technique, as well as the MAP estimator using the introduction of a *prior* for the distribution of r_0. However, in the case of negative binomial noise, the differences in the results are more significant. By introducing the *prior*, the tendency to underestimate r_0 is more pronounced. This trend of underestimation of r_0 was also noticed by MacDonald [41]. Again, it is expected that focus error in the original image is a contributing factor in the underestimation of r_0. This presents an interesting topic for potential future research.

True Image   Blurred/Noisy Image   Image Estimate

Figure 3.7: **In this demonstration, the true image (left) is blurred with an average short-exposure OTF with an r_0 of 2.6 cm. The blurred/noisy image (center) is the summation of 30 individual frames with independent realizations of negative binomial noise. The image estimate (right) was obtained using the best estimate of r_0=2.6 cm with the cap on the number of iterations set to 5000 for the CoV technique.**

Table 3.3: Results for Fully Illuminated Image Simulation with Negative Binomial Noise (True $r_0 = 2.6$ cm). Results in Bold Indicate the Algorithm that Performed Worse for a Particular Scenario

| Max Iterations Allowed - 1000					
Frames	SNR (dB)	MacDonald's Algorithm (cm)		CoV (cm)	
		Result	Error	Result	Error
1	14.7	**0.9**	**-1.7**	1.5	-1.1
10	24.7	**2.1**	**-0.5**	2.5	-0.1
20	27.7	**2.4**	**-0.2**	2.8	0.2
30	29.4	**2.6**	**0**	3.0	0.4
50	31.6	**3.0**	**0.4**	3.1	0.5
100	34.7	3.2	0.6	3.2	0.6
Max Iterations Allowed - 5000					
Frames	SNR (dB)	MacDonald's Algorithm (cm)		CoV (cm)	
		Result	Error	Result	Error
1	14.7	**0.9**	**-1.7**	1.4	-1.2
10	24.7	**1.8**	**-0.8**	2.0	-0.6
20	27.7	**2.0**	**-0.6**	2.2	-0.4
30	29.4	**2.2**	**-0.4**	2.4	-0.2
50	31.6	2.4	-0.2	2.4	-0.2
100	34.7	2.5	-0.1	2.5	-0.1
Max Iterations Allowed - 10000					
Frames	SNR (dB)	MacDonald's Algorithm (cm)		CoV (cm)	
		Result	Error	Result	Error
1	14.7	**0.9**	**-1.7**	1.3	-1.3
10	24.7	**1.8**	**-0.8**	1.9	-0.7
20	27.7	**2.0**	**-0.6**	2.1	-0.5
30	29.4	**2.1**	**-0.5**	2.2	-0.4
50	31.6	**2.2**	**-0.4**	2.3	-0.3
100	34.7	**2.3**	**-0.3**	2.4	-0.2
Max Iterations Allowed - 20000					
Frames	SNR (dB)	MacDonald's Algorithm (cm)		CoV (cm)	
		Result	Error	Result	Error
1	14.7	**0.8**	**-1.8**	1.3	-1.3
10	24.7	**1.8**	**-0.8**	1.9	-0.7
20	27.7	**1.9**	**-0.7**	2.0	-0.6
30	29.4	**2.0**	**-0.6**	2.0	-0.6
50	31.6	**2.1**	**-0.5**	2.2	-0.4
100	34.7	2.2	-0.4	2.2	-0.4

At this point, the functionality of the CoV technique has been demonstrated for fully illuminated scenes. Further experimentation was conducted on simulated stellar targets to identify the potential for measurement of atmospheric seeing on scenes where the majority of the image consists only of background illumination and noise. Since these targets are fully simulated, and thus inherently perfectly focused, underestimation of r_0 was not expected to be a problem for the CoV technique. Provided the algorithm is allowed enough time to iterate, convergence to the correct r_0 should be achieved. However, the scaling factor of M^2 in the *prior* (3.6) was expected to still cause some bias in the estimates for r_0 using MacDonald's algorithm.

3.2.2 Partially Illuminated Scenes.

Space Situational Awareness (SSA) is a key mission of the United States Air Force Space Command and was a key motivator for MacManus' research. One aspect of SSA involves using both telescope networks and radars to detect, identify, record and track all man-made objects orbiting the Earth. Knowing the exact locations of these orbiting objects in space is crucial for future space operation safety. Any debris that results from international space operations will be an ongoing risk to US assets for years to come as the orbits of the debris degrade toward Earth. The SSA mission only increases in importance as additional high value assets are placed in orbit. This is merely a single example and justification of the importance for deblurring techniques applicable to astronomical images [45].

The following simulations will consider three separate target configurations. We will look at a single point source that could be representative of a star, a scene that has multiple point sources arranged throughout the image and finally we will look at a cross bar pattern, as in Figure 3.8. We will again consider both Poisson and negative binomial assumptions with various SNR levels.
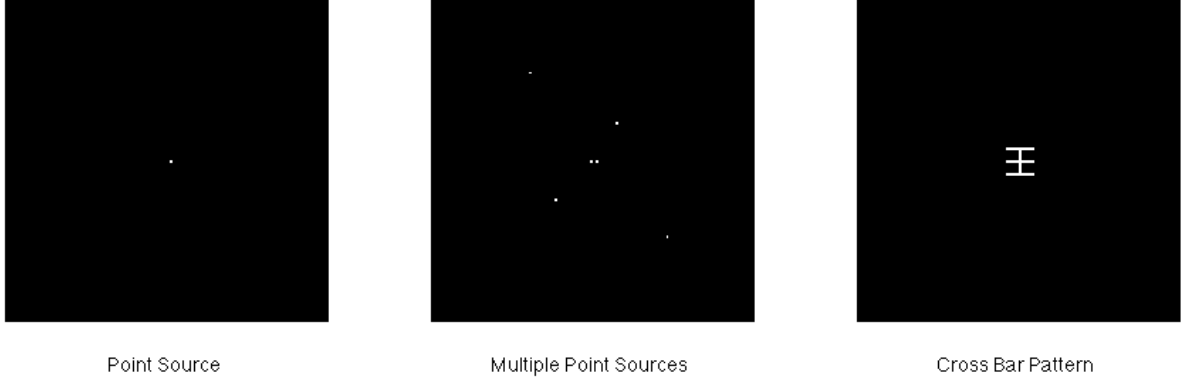
Figure 3.8: (left) This scene is representative of a single star or point source. (center) This scene contains multiple point sources with varying intensities and spacings. The spacing between the two point sources in the center of the image is a single pixel. (right) This scene contains a cross bar pattern.

The testing in Section 3.2.1 revealed that both algorithms are impacted by SNR and focus error. However, the simulations also revealed that no gain in performance was realized through the introduction of the *prior* for r_0, and that the CoV technique exhibited promise for estimation of r_0 as well as a deblurred scene. The results that follow add support for the hypothesis that underestimation of r_0 was a function of both SNR and focus error. The SNR for the various MCFAs used in the following simulations is identified in Table 3.4. As expected, the SNR for MCFAs with Poisson noise is higher than the SNR for MCFAs with negative binomial noise.

For demonstration purposes, the algorithm was allowed a cap of 1,000,000 iterations. Even under these conditions, underestimation was never a factor for images with adequate SNR using the CoV technique. At this point, it is unknown if it would be possible to predict the precise level of SNR at which the algorithm will converge to the correct value of r_0 since the relationship appears to be scene or contrast dependent. However, we can conclude that higher levels for SNR will yield better results. Additionally, even at low values of SNR we achieve reasonable estimations for the deblurred scene and r_0 using the CoV technique. On the other hand, by introducing a *prior* for the distribution of r_0, underestimation is more prevalent.

69

Table 3.4: Signal to Noise Ratio for Simulation Data

Signal to Noise Ratio (dB) for Poisson MCFAs			
Frames in MCFA	Point Source	Multiple Point Sources	Cross Bar
1	15.0	17.2	30.0
10	24.8	26.2	39.3
20	28.0	29.2	42.9
30	29.6	30.7	44.7
50	31.9	33.3	46.9
Signal to Noise Ratio (dB) for Negative Binomial MCFAs			
Frames in MCFA	Point Source	Multiple Point Sources	Cross Bar
1	11.8	13.1	14.4
10	22.6	23.7	25.7
20	26.3	27.0	29.3
30	27.5	28.1	30.5
50	29.4	30.0	32.7

Tables 3.5 and 3.7 demonstrate the utility of the CoV algorithm on partially illuminated scenes with Poisson and negative binomial noise respectively. Trials where the estimate for r_0 matched the true value are shown in bold. From these results, we conclude that provided enough frames are properly registered and averaged to provide adequate SNR, and enough time is allowed for convergence, the value of r_0 can be estimated to within 1 mm for the simulated optical configuration. In cases where we have low SNR the algorithm will tend to underestimate, but this is expected since the noise power in the images masks some of the high frequency content. If insufficient time is allowed for convergence, the algorithm will produce a high estimate for r_0, as observed when the cap for iterations was limited to 1,000. Additionally, we notice that in cases of adequate SNR, we do not have a problem of underestimation of r_0 since focus error was not present in these images.

Table 3.5: Results for Partially Illuminated Image Simulation with Poisson Noise (True $r_0 = 3.3$ cm). Results in Bold Indicate the Estimate Matched the True Value for r_0.

Max Iterations Allowed - 1000						
Frames	MAP Estimator (cm)			CoV (cm)		
	Point	Multi-Point	Cross Bar	Point	Multi-Point	Cross Bar
1	0.1	1.5	2.6	3.2	3.2	3.4
10	2.9	3.1	**3.3**	**3.3**	3.5	4.2
20	3.2	3.2	3.4	**3.3**	3.6	4.6
30	**3.3**	**3.3**	3.5	**3.3**	3.8	5.1
50	**3.3**	**3.3**	3.6	3.4	3.9	5.9
Max Iterations Allowed - 10000						
Frames	MAP Estimator (cm)			CoV (cm)		
	Point	Multi-Point	Cross Bar	Point	Multi-Point	Cross Bar
1	0.1	1.3	2.6	3.2	3.2	3.2
10	2.9	3.0	3.2	**3.3**	**3.3**	**3.3**
20	3.1	3.2	**3.3**	**3.3**	**3.3**	**3.3**
30	3.2	3.2	**3.3**	**3.3**	**3.3**	**3.3**
50	3.2	3.2	**3.3**	**3.3**	**3.3**	3.4
Max Iterations Allowed - 20000						
Frames	MAP Estimator (cm)			CoV (cm)		
	Point	Multi-Point	Cross Bar	Point	Multi-Point	Cross Bar
1	0.1	1.3	2.6	3.2	3.2	3.2
10	2.9	3.0	3.2	**3.3**	**3.3**	**3.3**
20	3.1	3.1	**3.3**	**3.3**	**3.3**	**3.3**
30	3.1	3.2	**3.3**	**3.3**	**3.3**	**3.3**
50	3.2	3.2	**3.3**	**3.3**	**3.3**	**3.3**
Max Iterations Allowed - 1000000						
Frames	MAP Estimator (cm)			CoV (cm)		
	Point	Multi-Point	Cross Bar	Point	Multi-Point	Cross Bar
1	0.1	1.3	2.5	3.2	3.2	3.2
10	2.8	3.0	3.2	**3.3**	**3.3**	**3.3**
20	3.1	3.1	**3.3**	**3.3**	**3.3**	**3.3**
30	3.1	3.2	**3.3**	**3.3**	**3.3**	**3.3**
50	3.2	3.2	**3.3**	**3.3**	**3.3**	**3.3**

In Figure 3.9 we demonstrate the performance of the CoV technique for the three target types in the presence of Poisson noise. Using the RL deconvolution algorithm with a cap on the number of iterations set to 10,000, and an MCFA consisting of 30 frames, we were able to recover the correct r_0 in all cases. For the point source targets, the blurring effects of the simulated atmosphere reduce the intensity to the point that it is difficult to visually identify the various point sources. However, when deconvolution is completed, each of the sources is easily identified. For the cross bar pattern, the process of deconvolution makes it much easier to identify the structure of the target pattern. While it may seem that a cap of 10,000 iterations is unreasonable, the algorithm will only take as much time as needed to converge within this upper bound. For instance, if the termination criteria is met before the upper bound on iterations is achieved, the algorithm will terminate. Even with a standard home computer with a 2.7GHz Intel® Core™ i5 processor and 16GB of memory, convergence was achieved in a reasonably short period of time for all target types as shown in Table 3.6. In this example, coarse convergence is to the nearest centimeter and

Table 3.6: Convergence Times for Simulations Shown in Figure 3.9.

Target Type	Coarse Convergence		Fine Convergence		Total
	Iterations	Time (sec)	Iterations	Time (sec)	Time (sec)
Single Point	627	1.66	968	2.49	4.15
Multi-Point	800	1.90	1,709	4.45	6.35
Cross Bar	2,123	4.26	8,275	17.51	21.77

fine convergence goes to the nearest millimeter. The algorithm could be manually interrupted sooner if needed. At which point, the lowest value of r_0 that has allowed convergence would be returned as the answer. For instance, in the example shown in Figure 3.9, if we interrupted the routine after 4.26 seconds for the cross bar pattern, we would get an estimated r_0 of 4 cm. The estimate continues to be refined until the best estimate is achieved after 21.77 seconds.
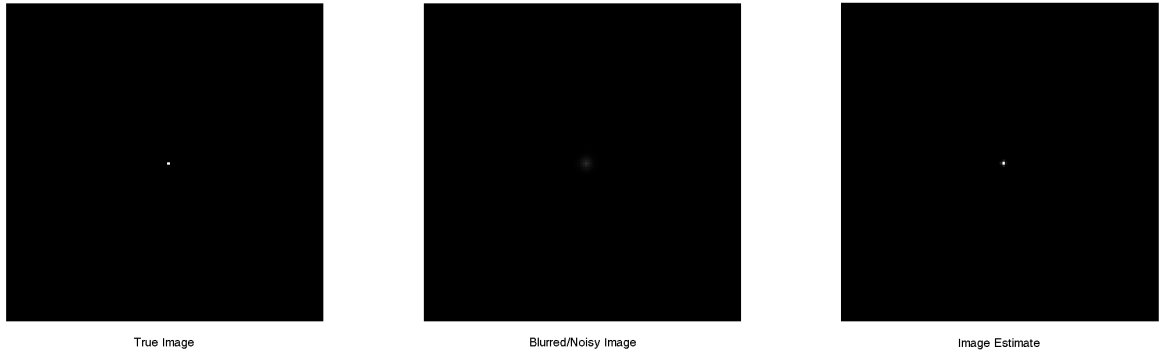
(a) Single Point Source
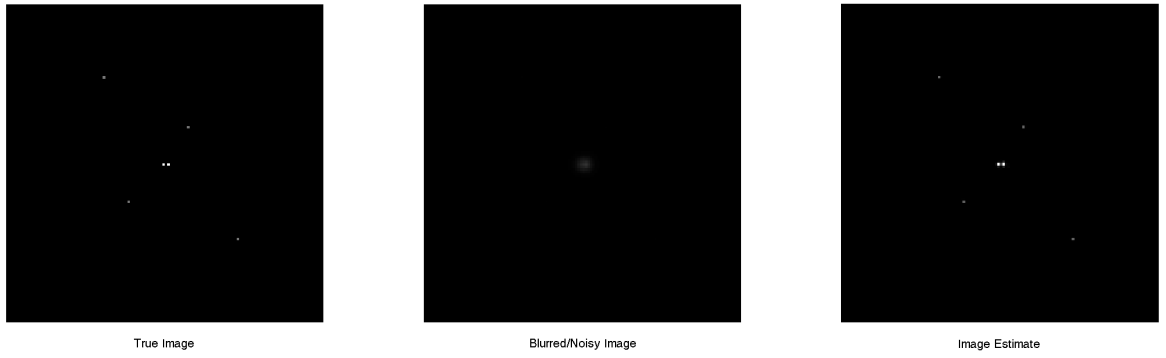
(b) Multiple Point Sources
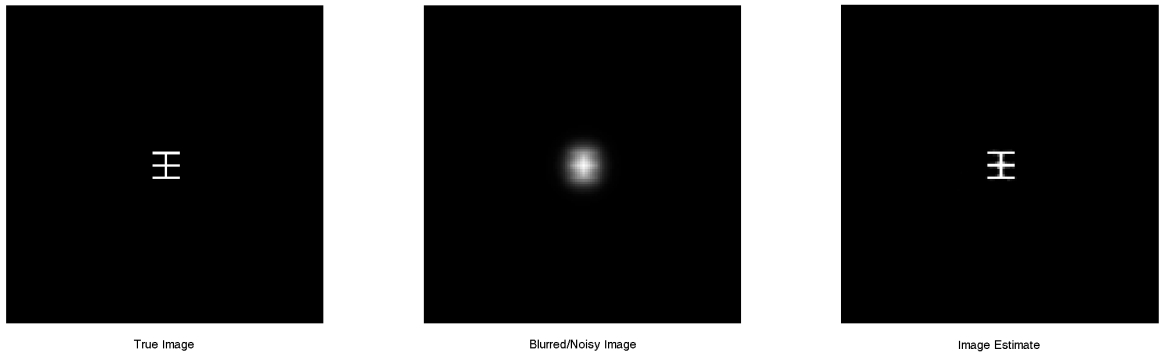
(c) Cross Bar Pattern

Figure 3.9: **Demonstration of the CoV technique using the RL deconvolution algorithm with an MCFA consisting of 30 frames for the single point source (a), multiple point sources (b), and the cross bar pattern (c).**

Table 3.7: Results for Partially Illuminated Image Simulation with Negative Binomial Noise (True $r_0 = 3.3$ cm). Results in Bold Indicate the Estimate Matched the True Value for r_0.

| Max Iterations Allowed - 1000						
Frames	**MAP Estimator (cm)**			**CoV (cm)**		
	Point	**Multi-Point**	**Cross Bar**	**Point**	**Multi-Point**	**Cross Bar**
1	0.1	1.0	1.8	3.1	3.0	5.0
10	2.4	2.7	2.8	3.4	3.7	5.1
20	2.9	3.0	3.0	3.5	4.0	5.8
30	3.0	3.1	3.1	3.7	4.8	6.5
50	3.2	3.2	3.2	3.9	5.0	8.5
Max Iterations Allowed - 10000						
Frames	**MAP Estimator (cm)**			**CoV (cm)**		
	Point	**Multi-Point**	**Cross Bar**	**Point**	**Multi-Point**	**Cross Bar**
1	0.1	0.5	1.7	3.1	2.9	3.4
10	2.3	2.6	2.7	**3.3**	3.2	3.4
20	2.7	2.9	3.0	**3.3**	**3.3**	3.5
30	2.9	3.0	3.1	**3.3**	**3.3**	3.7
50	3.0	3.1	**3.3**	**3.3**	**3.3**	4.0
Max Iterations Allowed - 20000						
Frames	**MAP Estimator (cm)**			**CoV (cm)**		
	Point	**Multi-Point**	**Cross Bar**	**Point**	**Multi-Point**	**Cross Bar**
1	0.1	0.4	1.7	3.1	2.9	3.2
10	2.3	2.6	2.7	3.2	3.2	3.2
20	2.7	2.9	3.1	3.2	**3.3**	**3.3**
30	2.9	3.0	3.1	**3.3**	**3.3**	**3.3**
50	3.0	3.1	3.2	**3.3**	**3.3**	**3.3**
Max Iterations Allowed - 1000000						
Frames	**MAP Estimator (cm)**			**CoV (cm)**		
	Point	**Multi-Point**	**Cross Bar**	**Point**	**Multi-Point**	**Cross Bar**
1	0.1	0.4	1.7	3.1	2.9	3.2
10	2.3	2.5	2.7	3.2	3.2	3.2
20	2.7	2.8	3.0	3.2	**3.3**	**3.3**
30	2.8	3.0	3.1	**3.3**	**3.3**	**3.3**
50	3.0	3.1	3.1	**3.3**	**3.3**	**3.3**

3.3 Experimental Results

The optical configuration shown in Figure 2.3 was used to obtain properly sampled images. The specifications for this setup are listed in Table 2.1. The experiments for fully illuminated scenes will use the image in Figure 3.10 as a target. This target will be placed indoors, 10 meters from the sensor where turbulence and illumination can be controlled. The incorporation of a step in the bottom portion of the scene will permit the measurement of the true r_0 for comparison with the estimated values. In order to create a turbulent atmosphere to image through, a heat source was directed in front of the telescope aperture. This technique allowed for the generation of repeatable turbulent atmospheres with r_0 values in the sub-centimeter range. Without the use of this heat source, all of the images would likely have been at or near the diffraction limit making validation of the CoV technique difficult.

E E E E
Q Q Q Q
D D D D
P P P P
C C C C
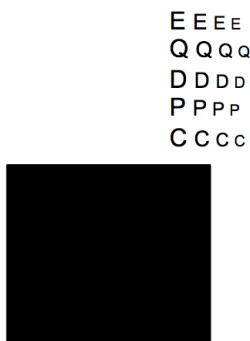
Figure 3.10: Scene used for each of the fully illuminated experiments. The top portion of the scene includes various characters of decreasing size. The bottom portion of the scene has a step target to allow for measurement of the true r_0.

3.3.1 Fully Illuminated Scenes - Natural Light.

In the following two experiments, the remote scene was fully illuminated by natural lighting. Given that the light source was incoherent, the Poisson statistical distribution for the photon arrival rate applies [21]. We will use the Richardson-

Lucy deconvolution algorithm (3.2) with PSFs parameterized by a range of r_0 values from 0.1 cm up to the aperture diameter of 5 cm. The images were blurred using a heat source to create various levels of atmospheric turbulence and subsequent image blurring.

In Figure 3.11 we demonstrate the ability to measure r_0 by measuring the step response from the collected MCFA as described in Section 2.5. The impulse response is then found by taking the derivative of this measured step response. Once we have the impulse response, we can vary r_0 per the relationship in (2.9) to find the theoretical total PSF, h_{tot}, that minimizes the error between the measured impulse response and the theoretical impulse response.
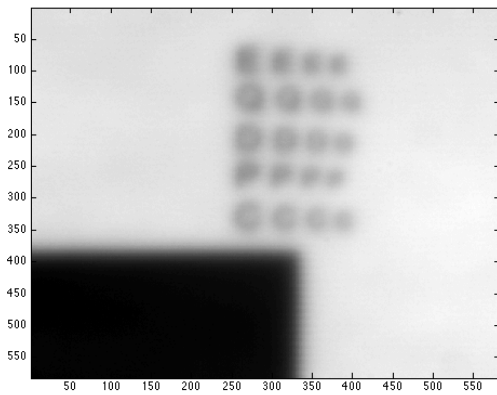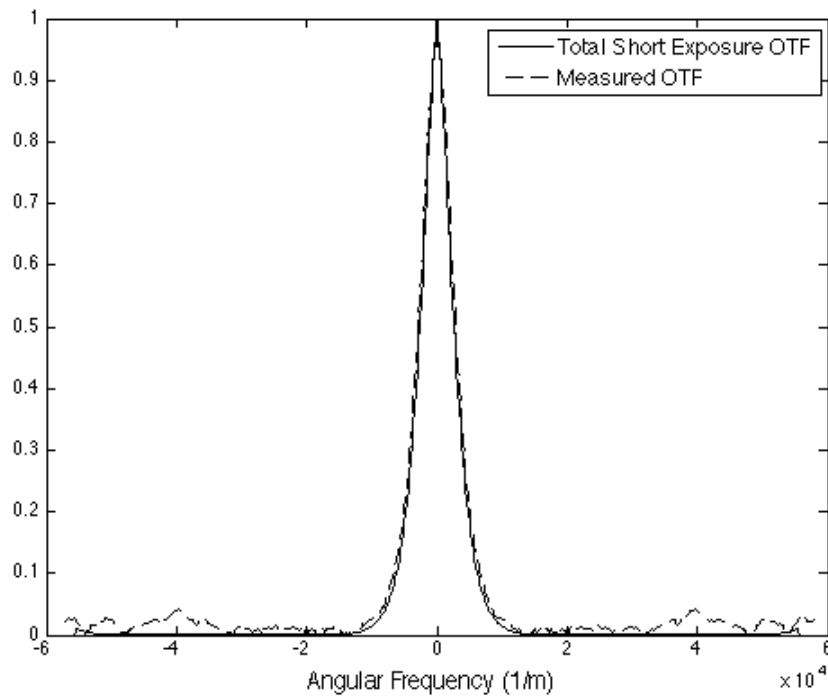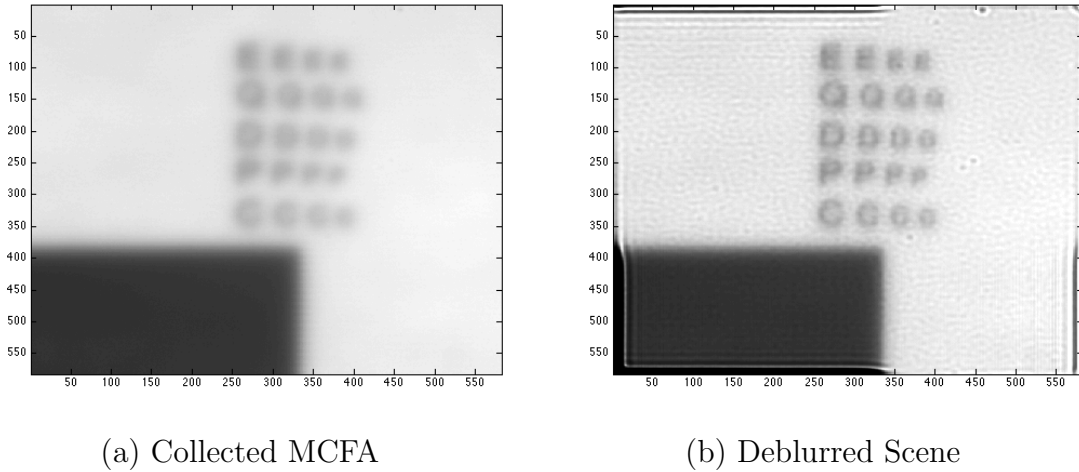
(a) Collected MCFA
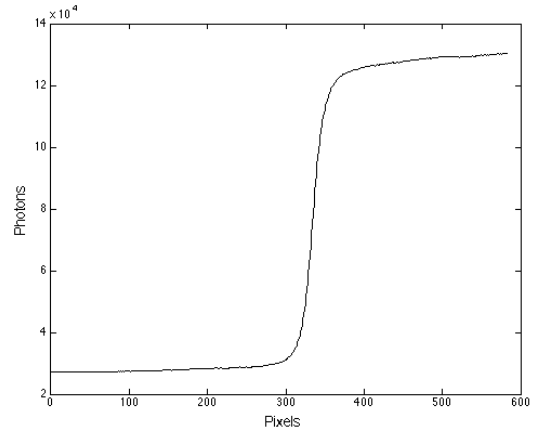
(b) Mean Step Response

(c) Theoretical/Experimental OTF Comparison

Figure 3.11: Using the step in the bottom portion of the colected remote scene (a) we can compute the mean step response for the collected MCFA (b). From this step response we compute the experimental OTF and find the theoretical short exposure OTF that minimizes MSE between the two (c).

In the first experiment shown in Figure 3.12, r_0 was measured at 0.4 cm. Using the CoV technique, we obtain an estimate of $r_0 = 0.5$ cm for an error in estimation of only 1 mm. At this point it is important to note that the edges of the deblurred images are distorted due to the implementation of the RL algorithm using the 2-D FFT in MATLAB. This implementation was chosen in order to decrease the time required for execution and results in a fair substitution as long as the image edges are not of importance. Therefore, when computing the variance per the relationship in (3.7), the variance for the image edges were ignored. In the collected MCFA, it is difficult to discern the smaller font sizes. However, when deconvolution is conducted with an OTF parameterized by the estimate for r_0, it is possible to identify each of the characters. In the second experiment shown in Figure 3.13, r_0 was measured at 1.1 cm. Using the CoV technique, we obtain an estimate of $r_0 = 1.1$ cm. While the blurring due to turbulence was less severe in this experiment, improvement in sharpness of the characters is again noted when deconvolution was conducted using the estimate for r_0.

(a) Collected MCFA   (b) Deblurred Scene

Figure 3.12: **(a) Collected MCFA consisting of 100 registered frames, each with an exposure time of** 0.001s. **(b) Deblurred image using the lowest** r_0 **for which convergence was achieved** ($r_0 = 0.5$ **cm).**
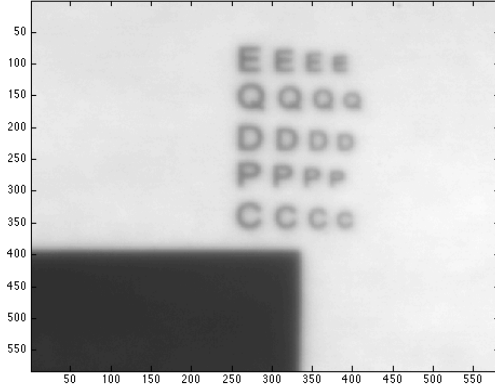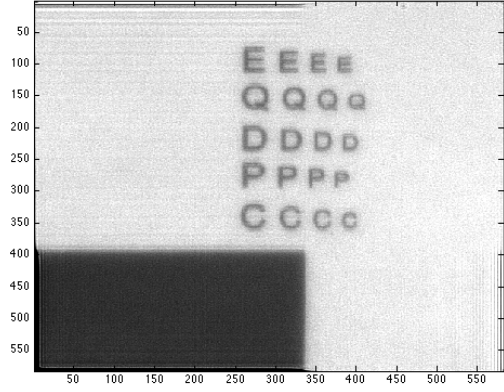
(a) Collected MCFA   (b) Deblurred Scene

Figure 3.13: **(a) Collected MCFA consisting of 100 registered frames, each with an exposure time of** $0.001s$**. (b) Deblurred image using the lowest** r_0 **for which convergence was achieved** $(r_0 = 1.1$ **cm).**

3.3.2   Fully Illuminated Scenes - Laser Illumination.

In the following two experiments, the remote scene was illuminated using a laser with a wavelength of 630 nm. Given that the light source was partially coherent, with a measured coherence parameter, $\mathcal{M} = 10$, the negative binomial model for speckle noise applies [21]. We will use the ML estimator in (3.9) with PSFs parameterized by a range of r_0 values from 0.1 cm up to the aperture diameter of 5 cm.

In the first experiment shown in Figure 3.14, r_0 was measured at 0.5 cm. Using the CoV technique, we obtain an estimate of $r_0 = 0.5$ cm. In the collected MCFA, it is difficult to discern the smaller font sizes, and based on where the illumination spot was centered, the top two rows of text are nearly illegible. However, when deconvolution is conducted with an OTF parameterized by the estimate for r_0 it is possible to identify most of the characters. It is much easier to identify the row of Qs, and the top row of Es is faintly visible. In the second experiment shown in Figure 3.15, r_0 was measured at 1.1 cm. Using the CoV technique, we obtain an estimate of $r_0 = 1.1$ cm. While the blurring due to turbulence was less severe in this experiment,

79

significant improvement is again noted when deconvolution was conducted using the estimate for r_0.

Table 3.8: Summary of Results for Fully Illuminated Image Experiments.

Trial	Estimated r_0 (cm)	Measured r_0 (cm)
Natural Light - Low r_0	0.5	0.4
Natural Light - High r_0	1.1	1.1
Laser Illumination - Low r_0	0.5	0.5
Laser Illumination - High r_0	1.1	1.1

Figure 3.14: (a) Collected MCFA consisting of **100 registered frames, each with an exposure time of** $0.005s$**. (b) Deblurred image using the lowest** r_0 **for which convergence was achieved (**$r_0 = 0.5$ **cm).**
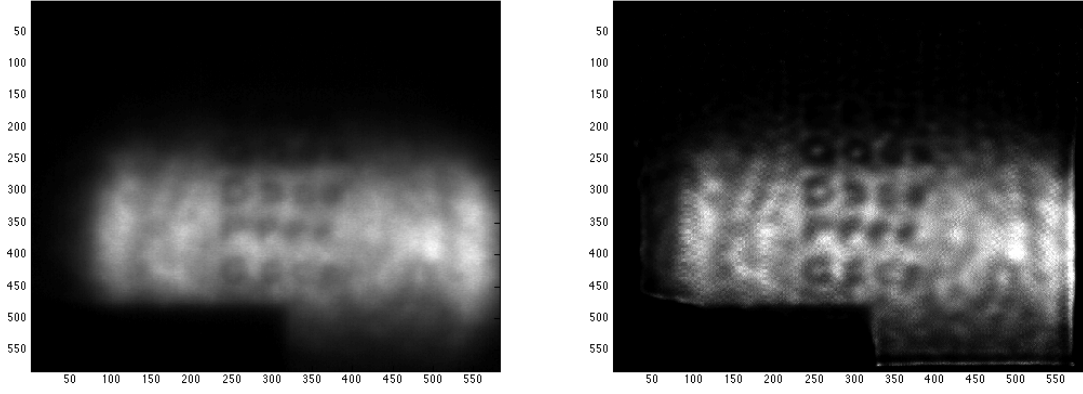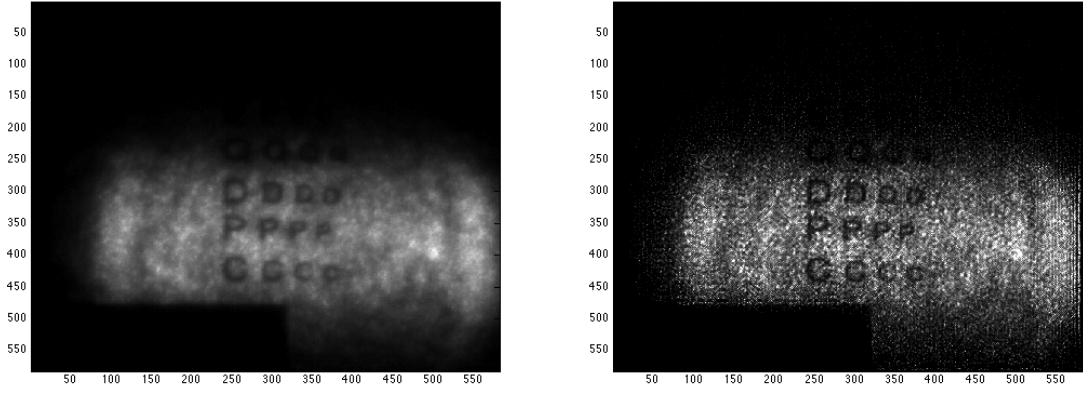

Figure 3.15: (a) Collected MCFA consisting of **100 registered frames, each with an exposure time of** $0.005s$**. (b) Deblurred image using the lowest** r_0 **for which convergence was achieved (**$r_0 = 1.1$ **cm).**

3.3.3 Correlation Technique for Measurement of Atmospheric Seeing.

With the previous experiments, the true value of r_0 could be measured by imaging a step target and taking the derivative to find the impulse response as shown in Figure 3.11. The step target could be placed in line with the desired remote scene such that the measurements were made through nearly identical columns of turbulent air. However, when trying to measure the true r_0 of stellar images for comparison with the experimental results, this was not a viable solution. We could average many short exposure images of a single star in order to get the average short exposure OTF parameterized by r_0, however this requires precise tilt removal and any shift estimation errors will appear as attenuation of the short exposure OTF and underestimation of r_0. Trying to average enough frames to achieve the long exposure OTF in order to find r_0 would likely take thousands of images to converge upon the optimal solution. Based on the frame rate of the experimental collection system, it is possible that the value for r_0 would change in the time required to gather this amount of data. Therefore, we considered an alternative technique for measuring the value of atmospheric seeing that considers the cross correlation of the collected images.

By considering all possible combinations of the cross correlations between a series of individual short exposure images, $\{S_k : k = 1, ..., K\}$, taken of a star, we can find the Cross Power Spectral Density (CPSD), $P_S(\nu_x, \nu_y)$, where

$$P_S\left(\nu_x, \nu_y\right) = E\left[\mathcal{F}\left\{S_k\left(x, y\right)\right\}\mathcal{F}^*\left\{S_{k'}\left(x, y\right)\right\}\right] \forall k \neq k'. \tag{3.12}$$

In other words, the CPSD is the correlation between the normalized Fourier transforms of all possible image combinations [30]. For a sequence of K images, there are a total of $K(K-1)/2$ non redundant cross correlations. Additionally, the CPSD of

the blurred point source can be shown to have the following relationship

$$P_S\left(\nu_x, \nu_y\right) = E\left\{\left|H\left(\nu_x, \nu_y\right)\right|^2\right\}, \tag{3.13}$$

where $E\left\{\left|H\left(\nu_x, \nu_y\right)\right|^2\right\}$ is the speckle transfer function [59]. Fortunately, the speckle transfer function can also be parameterized by r_0. Therefore, in order to obtain the true value for atmospheric seeing, we can find the value of r_0 that minimizes the error in (3.13). At this point we must keep in mind that this technique for measuring r_0 is limited to cases where we are imaging a point source. We will use this technique to demonstrate that the CoV technique will in fact identify the correct r_0.

### 3.3.4 Partially Illuminated Scenes.

For the experiments involving partially illuminated scenes, we chose to image a star. Stars can essentially be considered point sources of light, allowing us to use the technique presented in Section 3.3.3 to obtain truth data for comparison with the CoV results. While the resultant deblurred image is intuitive, the estimated values for r_0 prove that the technique can be successfully used to measure r_0 for partially illuminated scenes. For the experiments, we chose a relatively bright star near Polaris to image. This minimized the relative motion between the FOV and the imaged portion of the sky. All individual images were taken using an exposure time of 0.001s to ensure that the short-exposure model was applicable [21]. Additionally, each of the MCFAs is a compilation of 20 individual frames. Some experimentation with MCFAs consisting of more than 20 frames was accomplished. However, no increase in performance was observed.

In Table 3.9, the estimated value for r_0 was always within 0.2 cm of the measured value. Initially the cap on the number of iterations was set to 1,000. In all cases, if convergence was achieved for a particular level of r_0, it occurred within the first 100

Table 3.9: Results for Partially Illuminated Image Experiments.

Trial	Estimated r_0 (cm)	Measured r_0 (cm)
1	2.3	2.1
2	2.4	2.2
3	2.3	2.2
4	2.4	2.1
5	2.4	2.1

iterations. We then increased the number of iterations to 10,000 and subsequently 20,000 to see if convergence could be achieved for a lower level of r_0, but the results remained the same with the increased cap on iterations.
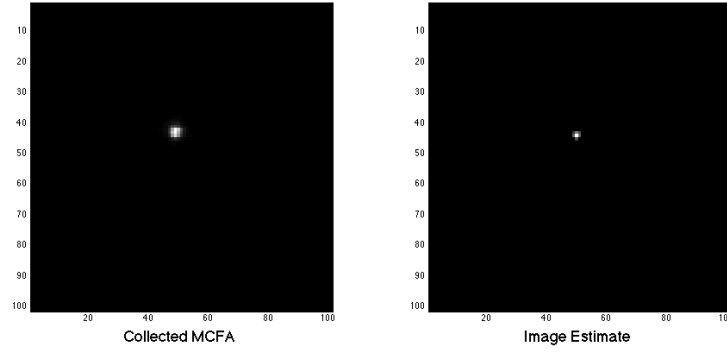
Figure 3.16: The collected MCFA consisting of 20 registered short exposure images (left) and the deblurred image estimate when the average short exposure OTF with an r_0 of 2.4 cm is used for deconvolution (right).

For the image shown in Figure 3.16 we first conducted a course search with a step size of 1 cm revealing that the minimum value of r_0 that will allow convergence is 3 cm. We then step through with a smaller step size and show that convergence can be achieved for values of r_0 as low as 2.4 cm. For this image, convergence occurs after just 68 iterations for an r_0 of 2.4 cm. However, it is divergent for anything less than this value. In Figure 3.16 we show the resultant deblurred image when using this best estimate for r_0 in conjunction with the RL deconvolution algorithm and the average short exposure OTF. As expected the image estimate approaches more of a point source than the original image.

3.4 Extension of CoV Technique for 3-D FLASH LADAR Images

Through the course of this research, it was found that the accuracy of the CoV technique was primarily dependent on the variance determined threshold for stopping the algorithm. This threshold is chosen based on the assumed noise model. For FLASH LADAR imagery, this does present a challenge since there are again various forms of noise present in the image. In order to effectively use the CoV technique we must be able to either predict the variance attributed to each source of noise, or measure the total variance through a series of independent images.

Three dimensional LADAR technology is receiving an increased interest as the technology improves. Currently, the commercially available sensors are severely under-sampled, and do not experience the effects of diffraction from atmospheric turbulence. However, as the technology continues to progress, it is expected that minimizing the effects of atmospheric turbulence will be important. Conversely, certain applications such as the imaging and tracking of space debris may require an optics configuration where the current sensors would receive properly sampled images. In those cases, the CoV technique could potentially be applied to identify the PSF parameterized by r_0 that will deblur the scene.

A typical full-waveform 3-D LADAR image is comprised of multiple 2-D images or frames separated by a small time delta. Therefore, the 3-D image can be flattened into a 2-D image by simply removing the range information and accumulating the intensity information for each pixel for the series of individual frames. Flattening a 3-D image into a 2-D image presents several challenges to the CoV technique. The primary issue being that the summation of multiple negative binomial random variables with different means is not another negative binomial random variable. Therefore it would be difficult to determine the best deconvolution algorithm to use based on the distribution of the data. By applying the Central Limit Theorem, it may be

possible to make a case for employing a deconvolution algorithm based on the Gaussian distribution. Likely less of a limiting factor would be the case where the image has uniform reflectance across a diversity of ranges. In this scenario, any contrast in intensity through multiple regions of the image may be lost, making it difficult to determine the best r_0. Fortunately, the atmosphere can be considered static for the laser illuminator pulse duration and subsequent detector integration times that are common to 3-D LADAR sensors [21], [58]. Given these challenges, likely the best option for employing the CoV technique on 3-D FLASH LADAR images would be to treat each of the 2-D frames separately. Based on this premise, this technique was originally explored as a means of identifying the best PSF parameterized by r_0 to be employed in algorithms such as the multiple surface FLASH LADAR ranging algorithm that will be discussed in Chapter IV and originally presented in [53].

Given the 3-D FLASH LADAR image model provided in Chapter II, we expect the total variance to consist of multiple components. Likely the most dominant form of image variance in illuminated portions of the scene will be speckle noise. However, the additional detector noise or background lighting noise may significantly impact the overall stopping threshold, especially in low illumination images. Due to the independence of the different noise sources, the total image variance for the kth frame, σ_{Tk}^2, will equal

$$\sigma_{Tk}^2 = \left(\sigma_{Sk}^2 + \sigma_{Bk}^2 \right), \tag{3.14}$$

where σ_{Sk}^2 is the noise due to speckle illumination and σ_{Bk}^2 is the noise due to detector bias for each of the K 2-D frames in the 3-D image. Since the 3-D image is made up of numerous 2-D images corresponding with unique ranges, we need to choose the image that allows the CoV technique the greatest chance for success. Given that the target profile in Figure 3.17 (a) is centered within the range gate of the 3-D FLASH LADAR sensor, we would expect the individual 2-D frames to have various levels of

86

contrast. Additionally, it is possible that the 2-D frames corresponding to specific ranges may not have a visible return present as shown in Figure 3.18. As shown in Figure 3.17(b), the estimates of r_0 are generally within 3 mm of the true value when the frames of higher contrast (frames 6-10 and 13-15) are used. However, when frames with low contrast are used, the accuracy of the estimates falls off. Additional demonstrations with the CoV technique on actual 3-D FLASH LADAR images will be provided in Chapter V.
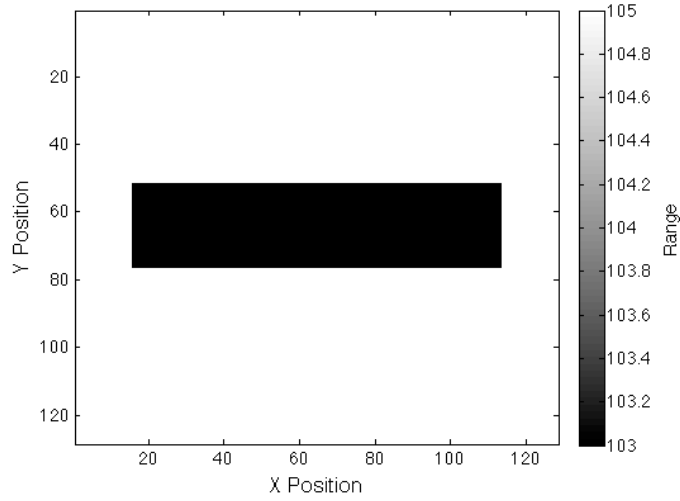
(a) Target Profile
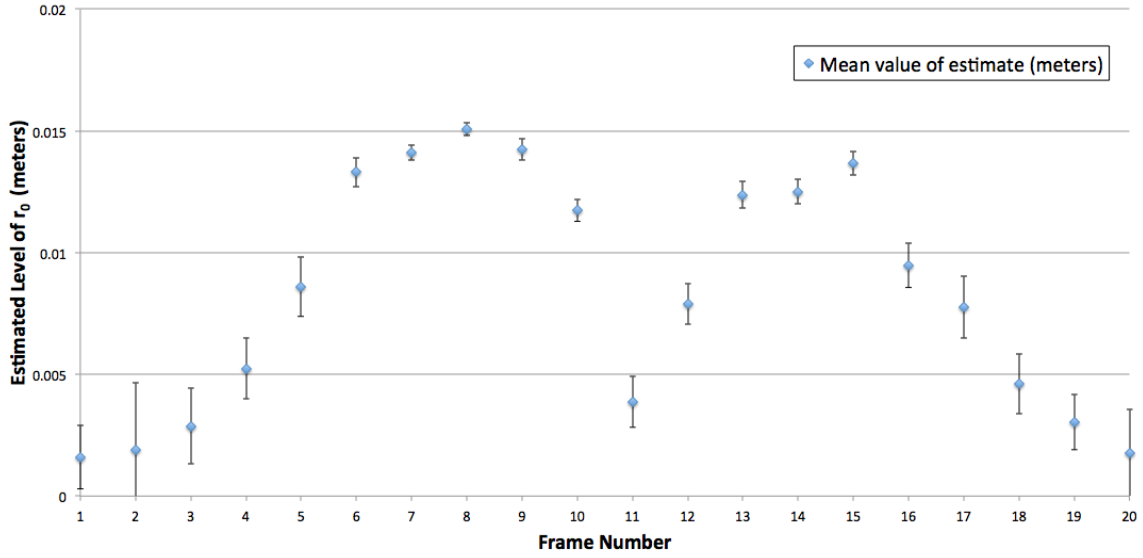
(b) Estimates for r_0

Figure 3.17: (a) Simulated target with a single raised bar placed at a range of 103 meters and the background is located at 105 meters. The reflectivity of the single bar is 0.7 and the reflectivity of the background is 1.0. (b) Estimated values of r_0 for each of the 2-D frames in the simulated 3-D FLASH LADAR image where the true value of $r_0 = 1.5$ cm. Error bars indicate the standard deviation of estimates for 30 separate trials.
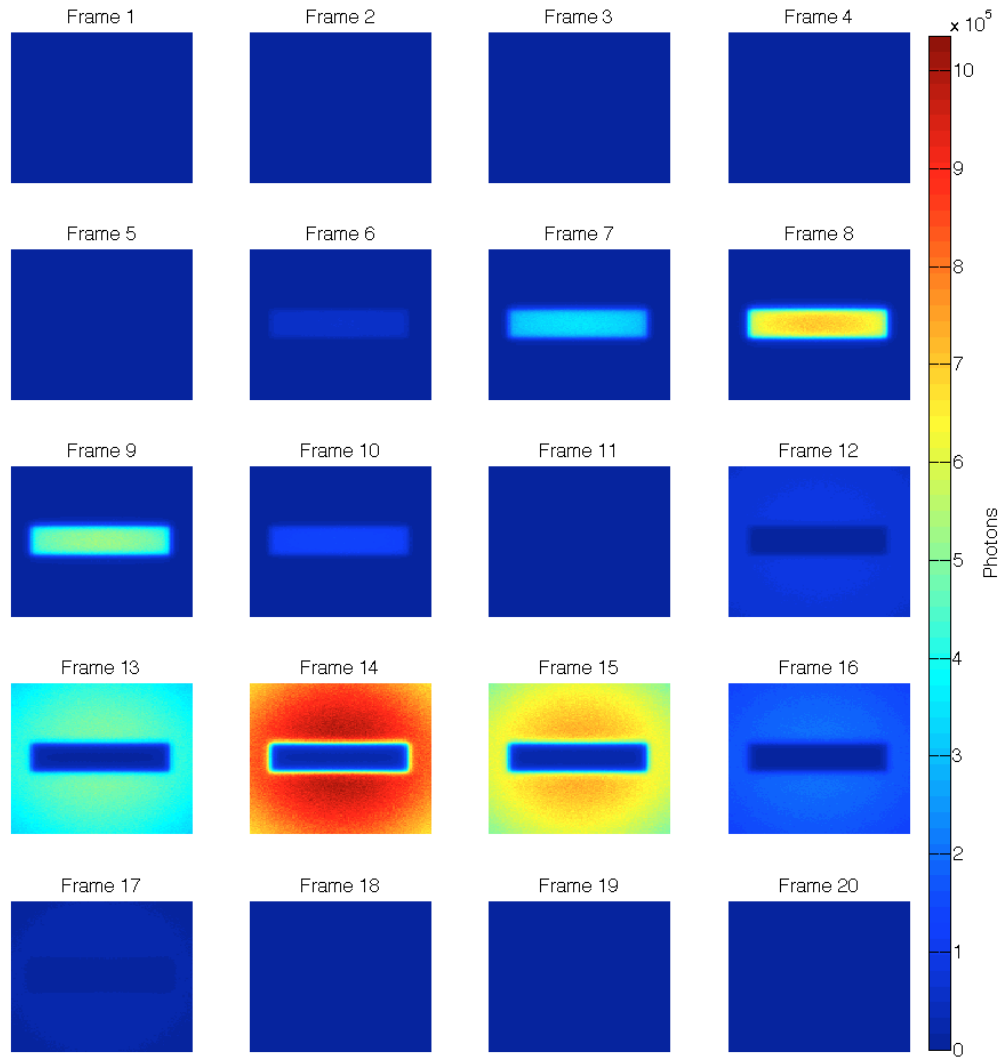
Figure 3.18: Individual 2-D frames based on the single bar target in Figure 3.17 being centered in the range gate for a LADAR system with parameters listed in Table 4.1.

3.5 Chapter Summary

The original focus of this work was to develop a blind deconvolution technique that could be employed in a tactical military environment where both time and computational power are limited. The intent behind its expansion and inclusion in this dissertation was to provide a means of comparison with the techniques that will be provided in Chapter V. The CoV technique detailed above allows for rapid and accurate estimations of the atmospheric OTF parameterized by the seeing parameter, r_0. As shown in Figure 3.3, the technique can be interrupted after any amount of time, at which point the best available results would be provided. If more time is provided, the results are generally enhanced. Additionally, the CoV technique reduces the possibility of noise amplification common with iterative deconvolution algorithms by ceasing iteration once the statistically predicted variance is achieved.

An interesting discovery was also made through the course of this effort and is highlighted in Section 3.2.1. This technique may be useful in recovering from minor focus error in the collected images. There are similarities between the atmospheric OTF and the OTF that arises from a minor focus error. As a result, the estimates for r_0 may be lower than the true value. Therefore, if this algorithm is to be used for atmospheric seeing measurement, the images must be in focus. Another source of error in estimation may arise if various portions of the scene have differing levels of r_0. In the cameraman photo used for the simulations, the objects in the background were likely impacted by a different level of atmospheric turbulence than those in the foreground. A potential topic for future research would be the relationship between the seeing parameter and focus interaction for varying levels of focus error and atmospheric turbulence.

IV. Multiple Surface Estimation

This chapter focuses on the development of a multiple surface ranging algorithm for full waveform 3-D FLASH LADAR images. In addition to providing pulse information for multiple surfaces per image pixel, the presented algorithm also reduces the effects of diffraction [52]. Simulation results will be presented to demonstrate the utility of this algorithm in cases where the blurring function is known. Experimental results will be presented in Chapter V in conjunction with results demonstrating the ability to solve for a parameterized blurring function.

Currently there are numerous efficient techniques such as peak estimation, cross-correlation and leading edge detection for identifying a single surface per pixel [58]. Of these techniques, the cross-correlation technique can be shown to be extremely accurate in identifying the range to a single surface. When multiple surfaces are present in each pixel or detector, the process of accurately identifying the correct ranges to each surface is more complex. With some modification, traditional ranging techniques can account for multiple surfaces given adequate temporal separation of the received pulses. However, effects due to the medium through which we are imaging introduce error into a traditional ranging technique. By diffracting light from neighboring areas within the scene, each detector or pixel may receive a pulse in which numerous false surfaces can be identified in addition to the potential for multiple true surfaces.

This chapter is organized as follows: Section 4.1 details the techniques employed to find solutions for the components of the Gaussian mixture model, in Section 4.2 an alternative solution is derived with a constraint applied to the amplitudes of the estimated pulses, Section 4.3 details the parameters used for simulation, Section 4.4 presents considerations and challenges associated with employing EM techniques to solve this problem and Section 4.5 presents a comparison of range RMSE for various competing algorithms or techniques.

4.1 EM Solution

The following algorithm is derived using an EM approach to jointly estimate the pulse parameters for a total of N surface returns as well as a signal bias. The MSID approach is similar to the EM approach derived by Dolce for fusing 2-D and 3-D LADAR data [16]. However, the work is not equivalent because Dolce's work does not account for the possibility of multiple surfaces per pixel, nor does it provide an estimate for the pulse amplitude or width. The EM process is generally broken down into two steps. First, the *E-Step* involves formulating a statistical relationship between the data collected (incomplete-data) and some known data model (complete-data), and then finding the expectation of the complete-data log-likelihood. The second step, the *M-Step* is to iteratively maximize the expectation of the complete-data log-likelihood function found in the *E-Step* [14]. The following sections will describe in detail the process for jointly estimating the pulse amplitudes, widths, ranges and overall bias for each image pixel.

4.1.1 Formulating the Complete and Incomplete-data.

As previously mentioned, the first step to the EM algorithm is to formulate the statistical relationship between the observed or collected data (incomplete-data) and the data model (complete-data). Since we are assuming our received pulse is essentially a Gaussian mixture with an additive bias, the relationship is

$$d(u, v, r_k) = \sum_{n=1}^{N} \sum_{x=1}^{M} \sum_{y=1}^{M} \tilde{d}^{(n)}(u, v, x, y, r_k) + \tilde{d}_B(u, v, r_k) \tag{4.1}$$

where d is the incomplete-data and the complete-data is made up of a component for the received pulse, $\tilde{d}^{(n)}$, and a separate component for the detector bias, $\tilde{d}_B$. It is important to note at this point that we are finding a total of N amplitudes, ranges and

corresponding pulse widths for each pixel. The expected values of the complete-data components are shown in (4.2) and (4.3).

$$E\left[\tilde{d}^{(n)}\left(u, v, x, y, r_k\right)\right] = \frac{A^{(n)}\left(x, y\right)}{\sqrt{2\pi}\sigma^{(n)}\left(x, y\right)} e^{-\frac{\left[r_k - r^{(n)}\left(x,y\right)\right]^2}{2\sigma^{(n)}\left(x,y\right)^2}} h\left(u - x, v - y\right) \quad (4.2)$$

$$E\left[\tilde{d}_B\left(u, v, r_k\right)\right] = B\left(u, v\right) \quad (4.3)$$

Since both components of the complete-data are approximated by the Poisson PMF, and the sum of Poisson random variables is also Poisson, we can now state the joint probability of the complete-data, p_J, as

$$
\begin{aligned}
p_J = {} & \left(\prod_{n=1}^{N} \prod_{u=1}^{M} \prod_{v=1}^{M} \prod_{k=1}^{K} \prod_{x=1}^{M} \prod_{y=1}^{M} p^{(n)}\left\{\tilde{d}^{(n)}\left(u, v, x, y, r_k\right)\right\}\right) \\
& \times \left(\prod_{u=1}^{M} \prod_{v=1}^{M} \prod_{k=1}^{K} p_B\left\{\tilde{d}_B\left(u, v, r_k\right)\right\}\right),
\end{aligned} \quad (4.4)
$$

where the probability for the nth pulse, $p^{(n)}$, is

$$
\begin{aligned}
p^{(n)}\left\{\tilde{d}^{(n)}\left(u, v, x, y, r_k\right)\right\} = {} & \frac{\frac{A^{(n)}(x,y)}{\sqrt{2\pi}\sigma^{(n)}(x,y)} e^{-\frac{\left[r_k - r^{(n)}(x,y)\right]^2}{2\sigma^{(n)}(x,y)^2}} h(u-x,v-y)^{\tilde{d}^{(n)}(u,v,x,y,r_k)}}{\tilde{d}^{(n)}(u,v,x,y,r_k)!} \\
& \times \exp\left\{\frac{A^{(n)}(x,y)}{\sqrt{2\pi}\sigma^{(n)}(x,y)} e^{-\frac{\left[r_k - r^{(n)}(x,y)\right]^2}{2\sigma^{(n)}(x,y)^2}} h\left(u - x, v - y\right)\right\},
\end{aligned} \quad (4.5)
$$

and the probability for the bias, p_B, is

$$p_B\left[\tilde{d}_B\left(u, v, r_k\right)\right] = \frac{B\left(u, v\right)^{\tilde{d}_B(u,v,r_k)} e^{-B(u,v)}}{\tilde{d}_B\left(u, v, r_k\right)!}. \quad (4.6)$$

Now that we have the joint probability, we can form the complete-data log-likelihood, L, by taking the natural logarithm of equation (4.4) such that

$$
\begin{aligned}
L = \sum_{n=1}^{N} \sum_{u=1}^{M} \sum_{v=1}^{M} \sum_{k=1}^{K} \sum_{x=1}^{M} \sum_{y=1}^{M} & \left(\tilde{d}^{(n)} \left(u, v, x, y, r_k \right) \right. \\
\times \ln & \left\{ \frac{A^{(n)}(x,y)}{\sqrt{2\pi}\sigma^{(n)}(x,y)} e^{-\frac{\left[r_k - r^{(n)}(x,y) \right]^2}{2\sigma^{(n)}(x,y)^2}} h\left(u - x, v - y\right) \right\} \\
- & \frac{A^{(n)}(x,y)}{\sqrt{2\pi}\sigma^{(n)}(x,y)} e^{-\frac{\left[r_k - r^{(n)}(x,y) \right]^2}{2\sigma^{(n)}(x,y)^2}} h\left(u - x, v - y\right) - \ln \left[\tilde{d}^{(n)} \left(u, v, x, y, r_k \right)! \right] \right) \\
+ \sum_{u=1}^{M} \sum_{v=1}^{M} \sum_{k=1}^{K} & \left\{ \tilde{d}_B \left(u, v, r_k \right) \ln \left[B\left(u, v\right) \right] - B\left(u, v\right) - \ln \left[\tilde{d}_B \left(u, v, r_k \right)! \right] \right\}.
\end{aligned} \tag{4.7}
$$

With the complete-data log-likelihood formed, we are now ready to perform the *E-Step*.

4.1.2 Finding the Expectation *E-Step*.

The *E-Step* involves finding the expectation of (4.7) conditioned on the incomplete-data and the previous estimates for the pulse and bias. Through the course of the following derivation, it was realized that maximizing the expectation with respect to the bias and the pulse are separable. Therefore, the following equations will be broken up into respective conditional expectations for the Gaussian pulse mixture, $Q^{(n)}$, and the bias, Q_B, to simplify the explanation. We now let Q be the overall conditional expectation of the complete-data log-likelihood function such that

$$
Q = \sum_{n=1}^{N} Q^{(n)} + Q_B, \tag{4.8}
$$

where

$$
Q^{(n)} = \sum_{u=1}^{M} \sum_{v=1}^{M} \sum_{k=1}^{K} \sum_{x=1}^{M} \sum_{y=1}^{M} \left(E\left[\tilde{d}^{(n)}(u,v,x,y,r_k) \middle| d(u,v,r_k), P_{old}^{(n)}(u,v,r_k), B_{old}(u,v) \right] \right.
$$

$$
\times \left\{ \ln\left[\frac{A^{(n)}(x,y)}{\sqrt{2\pi}\sigma^{(n)}(x,y)} h(u-x,v-y) \right] - \frac{\left[r_k - r^{(n)}(x,y)\right]^2}{2\sigma^{(n)}(x,y)^2} \right\}
$$

$$
- \frac{A^{(n)}(x,y)}{\sqrt{2\pi}\sigma^{(n)}(x,y)} e^{-\frac{\left[r_k - r^{(n)}(x,y)\right]^2}{2\sigma^{(n)}(x,y)^2}} h(u-x,v-y)
$$

$$
\left. - E\left\{ \ln\left[\tilde{d}^{(n)}(u,v,x,y,r_k)! \right] \middle| d(u,v,r_k), P_{old}^{(n)}(u,v,r_k), B_{old}(u,v) \right\} \right)
$$

$$(4.9)$$

and

$$
Q_B = \sum_{u=1}^{M} \sum_{v=1}^{M} \sum_{k=1}^{K} E\left[\tilde{d}_B(u,v,r_k) \middle| d(u,v,r_k), P_{old}^{(n)}(u,v,r_k), B_{old}(u,v) \right] \ln\left[B(u,v)\right]
$$

$$
- B(u,v) - E\left\{ \ln\left[\tilde{d}_B(u,v,r_k)! \right] \middle| d(u,v,r_k), P_{old}^{(n)}(u,v,r_k), B_{old}(u,v) \right\}.
$$

$$(4.10)$$

It can be shown that the expected value of the complete-data components with respect to the incomplete-data and the previous estimates for the pulse and bias are as indicated in (4.11) and (4.12) [62].

$$
E\left[\tilde{d}^{(n)}(u,v,x,y,r_k) \middle| d(u,v,r_k), P_{old}^{(n)}(u,v,r_k), B_{old}(u,v) \right]
$$
$$
= \frac{d(u,v,r_k) P_{old}^{(n)}(x,y,r_k) h(u-x,v-y)}{I_{old}(u,v,r_k)}
$$

$$(4.11)$$

$$
E\left[\tilde{d}_B(u,v,r_k) \middle| d(u,v,r_k), P_{old}^{(n)}(u,v,r_k), B_{old}(u,v) \right] = \frac{d(u,v,r_k) B_{old}(u,v)}{I_{old}(u,v,r_k)} \quad (4.12)
$$

In (4.11) and (4.12), $I_{old}(u,v,r_k)$ is the image produced by the pulse estimate and the additive bias and is equal to

$$
I_{old}(u,v,r_k) = \sum_{n=1}^{N} \sum_{x=1}^{M} \sum_{y=1}^{M} P_{old}^{(n)}(x,y,r_k) h(u-x,v-y) + B_{old}(u,v). \quad (4.13)
$$

4.1.3 Maximizing the Expectation *M-Step*.

Now that we have the expectation of the complete-data log-likelihood function, we can maximize it with respect to N total ranges, pulse widths and amplitudes as well as the signal bias. Similar to the previous work by Dolce, the received pulse from each surface is assumed to exist entirely in the range gate [16]. This assumption allows us to find a direct solution for range. In order to find estimates for $A^{(n)}$, $r^{(n)}$, $\sigma^{(n)}$ and B we must take the derivative of Q with respect to each parameter, set the resultant derivative equal to zero and then solve for the desired parameter.

Even though we are looking for a solution that involves N surface returns, it is possible and perhaps even likely depending on the imaged scene that the FOV for a given pixel may have fewer surfaces visible. In those cases, the corresponding amplitudes for ranges that are not truly present in the image scene are driven towards zero by this algorithm as will be demonstrated in Section 4.5. Several techniques exist for finding an upper bound on the number of surfaces in each pixel such as the center-of-gravity and zero-crossing of the first derivative of the received pulse [67]. This work assumed a fixed cap of two visible surfaces per pixel; however, this cap could be adjusted to account for varying numbers of surfaces per pixel depending on the number of 2-D slices per image.

We will first demonstrate the maximization process for the pulse amplitudes. Bringing the derivative inside of the summations of (4.14) is the first step to maximizing the expectation with respect to amplitude. Upon inspection it is evident that Q_B in (4.8) is not dependent on $A^{(n)}(x, y)$, thus its derivative with respect to $A^{(n)}(x, y)$

will be zero and we are left with

$$
\begin{aligned}
\frac{\partial Q}{\partial A^{(n)}(x,y)} &= \sum_{n=1}^{N}\sum_{u=1}^{M}\sum_{v=1}^{M}\sum_{k=1}^{K}\sum_{x=1}^{M}\sum_{y=1}^{M}\left(\frac{d(u,v,r_k)P_{old}^{(n)}(x,y,r_k)h(u-x,v-y)}{I_{old}(u,v,r_k)}\right.\\
&\times \frac{\partial}{\partial A^{(n)}(x_0,y_0)}\left\{\ln\left[\frac{A^{(n)}(x,y)}{\sqrt{2\pi}\sigma^{(n)}(x,y)}h\left(u-x,v-y\right)\right]-\frac{\left[r_k-r^{(n)}(x,y)\right]^2}{2\sigma^{(n)}(x,y)^2}\right\}\\
&-\frac{\partial}{\partial A^{(n)}(x_0,y_0)}\left\{\frac{A^{(n)}(x,y)}{\sqrt{2\pi}\sigma^{(n)}(x,y)}e^{-\frac{\left[r_k-r^{(n)}(x,y)\right]^2}{2\sigma^{(n)}(x,y)^2}}h\left(u-x,v-y\right)\right\}\\
&\left.-\frac{\partial}{\partial A^{(n)}(x_0,y_0)}E\left\{\ln\left[\tilde{d}^{(n)}\left(u,v,x,y,r_k\right)!\right]\middle| d\left(u,v,r_k\right),P_{old}^{(n)}\left(u,v,r_k\right),B_{old}\left(u,v\right)\right\}\right).
\end{aligned}
$$
(4.14)

Computing the derivative of (4.14) and eliminating terms with no dependency on $A^{(n)}(x,y)$, we can further simplify to

$$
\begin{aligned}
\frac{\partial Q}{\partial A^{(n)}(x,y)} &= \sum_{n=1}^{N}\sum_{u=1}^{M}\sum_{v=1}^{M}\sum_{k=1}^{K}\sum_{x=1}^{M}\sum_{y=1}^{M}\left(\frac{d(u,v,r_k)P_{old}^{(n)}(x,y,r_k)h(u-x,v-y)}{I_{old}(u,v,r_k)}\times\left[\frac{1}{A^{(n)}(x,y)}\frac{\partial A^{(n)}(x,y)}{\partial A^{(n)}(x_0,y_0)}\right]\right.\\
&\left.-\frac{1}{\sqrt{2\pi}\sigma^{(n)}(x,y)}e^{-\frac{\left[r_k-r^{(n)}(x,y)\right]^2}{2\sigma^{(n)}(x,y)^2}}h\left(u-x,v-y\right)\frac{\partial A^{(n)}(x,y)}{\partial A^{(n)}(x_0,y_0)}\right).
\end{aligned}
$$
(4.15)

We now have that the derivative of Q with respect to $A^{(n)}(x,y)$ is

$$
\begin{aligned}
\frac{\partial Q}{\partial A^{(n)}(x,y)} &= \sum_{n=1}^{N}\sum_{u=1}^{M}\sum_{v=1}^{M}\sum_{k=1}^{K}\sum_{x=1}^{M}\sum_{y=1}^{M}\left\{\frac{d(u,v,r_k)P_{old}^{(n)}(x,y,r_k)h(u-x,v-y)}{I_{old}(u,v,r_k)}\times\left[\frac{1}{A^{(n)}(x,y)}\right]\right.\\
&\left.-\frac{1}{\sqrt{2\pi}\sigma^{(n)}(x,y)}e^{-\frac{\left[r_k-r^{(n)}(x,y)\right]^2}{2\sigma^{(n)}(x,y)^2}}h\left(u-x,v-y\right)\right\}\delta\left(x-x_0,y-y_0\right).
\end{aligned}
$$
(4.16)

The Dirac delta function in (4.16) allows us to remove two of the summations with respect to x and y via the sifting property, since all values not equal to x_0 and y_0 will

be zero, leaving us with

$$
\begin{aligned}
\frac{\partial Q}{\partial A^{(n)}(x,y)} = \sum_{u=1}^{M} \sum_{v=1}^{M} \sum_{k=1}^{K} & \left\{ \frac{d(u,v,r_k) P_{old}^{(n)}(x_0,y_0,r_k) h(u-x_0,v-y_0)}{I_{old}(u,v,r_k)} \times \left[\frac{1}{A^{(n)}(x,y)} \right] \right. \\
& \left. - \frac{1}{\sqrt{2\pi}\sigma^{(n)}(x_0,y_0)} e^{-\frac{\left[r_k - r^{(n)}(x_0,y_0) \right]^2}{2\sigma^{(n)}(x_0,y_0)^2}} h\left(u - x_0, v - y_0 \right) \right\} .
\end{aligned}
\tag{4.17}
$$

We can now set (4.17) equal to zero and solve for $A^{(n)}(x,y)$,

$$
A^{(n)}(x_0,y_0) = \frac{\displaystyle\sum_{u=1}^{M} \sum_{v=1}^{M} \sum_{k=1}^{K} \left[\frac{d(u,v,r_k) P_{old}^{(n)}(x_0,y_0,r_k) h(u-x_0,v-y_0)}{I_{old}(u,v,r_k)} \right]}{\displaystyle\sum_{u=1}^{M} \sum_{v=1}^{M} \sum_{k=1}^{K} \left[-\frac{1}{\sqrt{2\pi}\sigma^{(n)}(x_0,y_0)} e^{-\frac{\left(r_k - r^{(n)}(x_0,y_0) \right)^2}{2\sigma^{(n)}(x_0,y_0)^2}} h\left(u - x_0, v - y_0 \right) \right]} . \tag{4.18}
$$

If we now recall the assumption that the pulse is entirely within the range gate and make the additional assumption that

$$
\sum_{x,y=1}^{N} h(x,y) = 1, \tag{4.19}
$$

the denominator of (4.18) will sum to one leaving us with a final iterative solution for $A^{(n)}(x,y)$ that is

$$
A^{(n)}(x_0,y_0) = \sum_{k=1}^{K} P_{old}^{(n)}(x_0,y_0,r_k) \sum_{u=1}^{M} \sum_{v=1}^{M} \frac{d(u,v,r_k) h(u-x_0,v-y_0)}{I_{old}(u,v,r_k)}. \tag{4.20}
$$

We can perform a very similar process for maximizing Q with respect to range, but this time we consider our assumption of the pulse being within the range gate up front. This assumption forces the summation of the pulse with respect to a change in range to remain a constant. Or in other words, even though the pulse location is dependent on range, the summation of the derivative with respect to $r^{(n)}(x_0,y_0)$ is

zero. We now just have the derivative

$$
\begin{aligned}
\frac{\partial Q}{\partial r^{(n)}(x,y)} &= \sum_{n=1}^{N} \sum_{u=1}^{M} \sum_{v=1}^{M} \sum_{k=1}^{K} \sum_{x=1}^{M} \sum_{y=1}^{M} \left(\frac{d(u,v,r_k) P_{old}^{(n)}(x,y,r_k) h(u-x,v-y)}{I_{old}(u,v,r_k)} \right. \\
&\left. \times \frac{\partial}{\partial r^{(n)}(x_0,y_0)} \left\{ \ln \left[\frac{A^{(n)}(x,y)}{\sqrt{2\pi}\sigma^{(n)}(x,y)} h\left(u-x,v-y\right) \right] - \frac{\left[r_k - r^{(n)}(x,y)\right]^2}{2\sigma^{(n)}(x,y)^2} \right\} \right)
\end{aligned}
\tag{4.21}
$$

to maximize. Following a very similar simplification process to the above process for the amplitude, we are left with the solution for range

$$
r^{(n)}(x_0,y_0) = \frac{\sum_{k=1}^{K} r_k P_{old}^{(n)}(x_0,y_0,r_k) \sum_{u=1}^{M} \sum_{v=1}^{M} \frac{d(u,v,r_k)h(u-x_0,v-y_0)}{I_{old}(u,v,r_k)}}{\sum_{k=1}^{K} P_{old}^{(n)}(x_0,y_0,r_k) \sum_{u=1}^{M} \sum_{v=1}^{M} \frac{d(u,v,r_k)h(u-x_0,v-y_0)}{I_{old}(u,v,r_k)}}.
\tag{4.22}
$$

This solution is nearly identical to the solution found by Dolce, with the exception that it is generalized for multiple surfaces per detector, and it does not consider the effects of 3-D and 2-D fusion [16]. Originally, pulse width was not of major concern because the simulation results were not sensitive to changes in pulse width given that all targets were simulated to be oriented normally to the illumination source. However, through the course of employing this algorithm on experimentally collected data where targets were not always oriented normally to the illumination source, it was realized that pulse width deviation caused a noticeable error in the results. For this reason, the solution for pulse width was derived using the same techniques previously presented, and found to equal

$$
\sigma^{(n)}(x_0,y_0) = \frac{\sum_{k=1}^{K} \left[r_k - r^{(n)}(x_0,y_0)\right]^2 P_{old}^{(n)}(x_0,y_0,r_k) \sum_{u=1}^{M} \sum_{v=1}^{M} \frac{d(u,v,r_k)h(u-x_0,v-y_0|r_0)}{I_{old}(u,v,r_k)}}{\sum_{k=1}^{K} P_{old}^{(n)}(x_0,y_0,r_k) \sum_{u=1}^{M} \sum_{v=1}^{M} \frac{d(u,v,r_k)h(u-x_0,v-y_0|r_0)}{I_{old}(u,v,r_k)}}.
\tag{4.23}
$$

During the iterative process, the algorithm will then allow the pulse width to adjust based on the orientation and physical properties of the targeted surfaces.

We can now perform a similar procedure to find the solution for pixel bias. For this solution we again refer back to equations (4.8), (4.9) and (4.10). We notice that (4.9) is not dependent on pixel bias. Therefore taking the derivative of (4.10) with respect to $B(u_0, v_0)$ will be sufficient

$$
\begin{aligned}
\frac{\partial Q}{\partial B(u_0,v_0)} = & \sum_{u=1}^{M} \sum_{v=1}^{M} \sum_{k=1}^{K} \left[\frac{\partial}{\partial B(u_0,v_0)} \left\{ \frac{d(u,v,k) B_{old}(u,v)}{I_{old}(u,v,r_k)} \ln\left[B\left(u,v\right)\right] - B\left(u,v\right) \right\} \right. \\
& \left. - \frac{\partial}{\partial B(u_0,v_0)} \left(E\left\{ \ln\left[\tilde{d}\left(u,v,r_k\right)!\right] \middle| d\left(u,v,r_k\right), P_{old}^{(n)}\left(u,v,r_k\right), B_{old}\left(u,v\right) \right\} \right) \right].
\end{aligned}
\tag{4.24}
$$

Equation (4.24) simplifies to

$$
\frac{\partial Q}{\partial B\left(u_0,v_0\right)} = \sum_{u=1}^{M} \sum_{v=1}^{M} \sum_{k=1}^{K} \left\{ \left[\frac{d\left(u,v,r_k\right) B_{old}\left(u,v\right)}{I_{old}\left(u,v,r_k\right)} \times \frac{1}{B\left(u,v\right)} - 1 \right] \frac{\partial B\left(u,v\right)}{\partial B\left(u_0,v_0\right)} \right\}.
\tag{4.25}
$$

The partial derivative of $B(u,v)$ with respect to $B(u_0,v_0)$ will yield a Dirac delta allowing for further simplification to

$$
\frac{\partial Q}{\partial B\left(u_0,v_0\right)} = \sum_{k=1}^{K} \left[\frac{d\left(u_0,v_0,r_k\right) B_{old}\left(u_0,v_0\right)}{I_{old}\left(u_0,v_0,r_k\right)} \times \frac{1}{B\left(u_0,v_0\right)} - \delta\left(u-u_0, v-v_0\right) \right].
\tag{4.26}
$$

This equation can now be set equal to zero and solved for $B(u_0, v_0)$ yielding the solution for pixel bias as shown in (4.27)

$$
B\left(u_0,v_0\right) = B_{old}\left(u_0,v_0\right) \frac{\sum_{k=1}^{K} \frac{d(u_0,v_0,r_k)}{I_{old}(u_0,v_0,r_k)}}{K}.
\tag{4.27}
$$

Using the results from (4.20), (4.22), (4.23) and (4.27) we are now able to iteratively find estimates for all parameters simultaneously. The following section presents an added constraint on amplitude estimation that further enhances the capability of the algorithm.

Initialization is a commonly cited challenge for EM algorithms [69]. However, the

iterative solutions presented in (4.20), (4.22), (4.23) and (4.27), can effectively be initialized as follows:

- Initialize range through peak search or correlation technique

- Initialize amplitude to intensity values at initial range estimates

- Initialize pulse width to the outgoing pulse width

- Initialize pixel bias to minimum value in received pulse

This methodology for initialization proved effective as shown in the later results.

4.2   Constrained Amplitude EM Solution

It is generally accepted that the Richardson-Lucy algorithm (3.2) will produce a maximum likelihood estimate of a 2-D scene when the blurring source or PSF is known and the noise is Poisson [57], [62]. However, when an image is both spatially and temporally blurred as is the case with 3-D imaging through a turbulent atmosphere, the Richardson-Lucy algorithm may be less than optimal.

The solutions provided in Section 4.1.3 allowed us to directly solve for the amplitude, range, pulse width and bias for N surfaces as detected by each pixel in a APD array while also removing the spatial and temporal blurring associated with the PSF. Using the stopping criteria from Section 2.4, it was observed that the algorithm often converged before optimal estimates on pulse amplitude were achieved. While the results from the algorithm were still an improvement over traditional techniques, an attempt was made to improve upon this solution by considering the following constraint. When dealing with full-waveform data, each 3-D image can be flattened into an amplitude only 2-D image by simply summing the amplitude for each slice in the data cube. With this in mind, the amplitude only 2-D image obtained from

the Richardson-Lucy deconvolution algorithm appears to be a potential candidate for an added constraint to prevent inappropriate convergence of the EM Algorithm designed for 3-D data. Alternatively, a more time consuming but likely more accurate approach would be to use the ML estimate derived by MacDonald on each 2-D frame as described in Section 3.4 prior to summation into an overall 2-D image of the remote scene [44]. Finally, a constraint of this nature could also be applied in cases where diffraction is not of concern. In this case, the 2-D image used as the constraint would be obtained by summing the received data along the temporal axis. The work by Schulz supports the idea of introducing a penalty function via a Lagrange multiplier to prevent the algorithm's convergence to undesirable solutions [60]. Provided the function that we add as a penalty is continuously differentiable, the method of using a Lagrange multiplier will allow for convergence to a maximal solution for the log-likelihood subject to the constraint [65].

Using the amplitude only representation of the 3-D data cube, we found the best results when using the ML estimate on each 2-D frame prior to summation into the constraint image. This constraint image is used to penalize estimates for amplitude any time the following equation is not satisfied

$$A_c(x, y) = \sum_{n=1}^{N} A^{(n)}(x, y),$$
(4.28)

where A_c is the amplitude of the 2-D constraint image. The original multi-surface EM algorithm allowed for maximization of the log-likelihood, L, with respect to N amplitudes, ranges and pulse widths as well as a pixel bias. In the case of the N surface model, this can be written in simplified notation as

$$L(A, r, \sigma, B) = \sum_{n=1}^{N} f\left(A^{(n)}, r^{(n)}, \sigma^{(n)}, B\right),$$
(4.29)

where f represents the component of the log-likelihood for each of the surface returns and is a function of pulse amplitude, range, width and bias. We now want to maximize $L(A, r, \sigma, B)$ subject to a new constraint, $g(A)$, where

$$g(A) = \sum_{n=1}^{N} A^{(n)} - A_c = 0. \tag{4.30}$$

In order to incorporate this constraint, we must introduce a new variable, χ, for our Lagrange multiplier and then maximize the constrained log-likelihood, L_φ,

$$L_\varphi (A, r, \sigma, B, \chi) = L(A, r, \sigma, B) - \chi [g(A)]. \tag{4.31}$$

By incorporating the constraint via the method above, we ensure that mathematical rigor is retained, and can demonstrate the enhanced performance over the non-constrained algorithm. Using (4.7) as a basis, L_φ becomes

$$
\begin{aligned}
L_\varphi = {}& \sum_{n=1}^{N} \sum_{u=1}^{M} \sum_{v=1}^{M} \sum_{k=1}^{K} \sum_{x=1}^{M} \sum_{y=1}^{M} \left(\tilde{d}^{(n)}(u, v, x, y, r_k) \right. \\
& \times \ln \left\{ \frac{A^{(n)}(x,y)}{\sqrt{2\pi}\sigma^{(n)}(x,y)} e^{-\frac{\left[r_k - r^{(n)}(x,y)\right]^2}{2\sigma^{(n)}(x,y)^2}} h(u - x, v - y) \right\} \\
& - \frac{A^{(n)}(x,y)}{\sqrt{2\pi}\sigma^{(n)}(x,y)} e^{-\frac{\left[r_k - r^{(n)}(x,y)\right]^2}{2\sigma^{(n)}(x,y)^2}} h(u - x, v - y) - \ln \left[\tilde{d}^{(n)}(u, v, x, y, r_k)! \right] \\
& \left. - \chi(x, y) \left[\sum_{n'=1}^{N} A^{(n')}(x, y) - A_c(x, y) \right] \right) \\
& + \sum_{u=1}^{M} \sum_{v=1}^{M} \sum_{k=1}^{K} \left\{ \tilde{d}_B(u, v, r_k) \ln [B(u,v)] - B(u,v) - \ln \left[\tilde{d}_B(u, v, r_k)! \right] \right\}.
\end{aligned}
\tag{4.32}
$$

With the constrained complete-data log-likelihood formed, we are again ready to perform the EM process.

It is readily apparent from (4.32) that the solutions for range, pulse width and bias will not be changed by the inclusion of the constraint. Therefore, only a new solution for amplitude and the constraint parameter are needed. Due to the addition

103

of the constraint, $Q^{(n)}$, from (4.9) becomes

$$
\begin{aligned}
Q_\phi^{(n)} = & \sum_{u=1}^{M} \sum_{v=1}^{M} \sum_{k=1}^{K} \sum_{x=1}^{M} \sum_{y=1}^{M} \left(E\left[\tilde{d}^{(n)}\left(u,v,x,y,r_k\right) \middle| d\left(u,v,r_k\right), P_{old}^{(n)}\left(u,v,r_k\right), B_{old}\left(u,v\right) \right] \right. \\
& \times \left\{ \ln\left[\frac{A^{(n)}(x,y)}{\sqrt{2\pi}\sigma^{(n)}(x,y)} h\left(u-x,v-y\right) \right] - \frac{\left[r_k - r^{(n)}(x,y) \right]^2}{2\sigma^{(n)}(x,y)^2} \right\} \\
& - \frac{A^{(n)}(x,y)}{\sqrt{2\pi}\sigma^{(n)}(x,y)} e^{-\frac{\left[r_k - r^{(n)}(x,y) \right]^2}{2\sigma^{(n)}(x,y)^2}} h\left(u-x,v-y\right) \\
& - E\left\{ \ln\left[\tilde{d}^{(n)}\left(u,v,x,y,r_k\right)! \right] \middle| d\left(u,v,r_k\right), P_{old}^{(n)}\left(u,v,r_k\right), B_{old}\left(u,v\right) \right\} \\
& \left. - \chi\left(x,y\right) \left[\sum_{n'=1}^{N} A^{(n')}\left(x,y\right) - A_c\left(x,y\right) \right] \right)
\end{aligned}
$$
(4.33)

Ultimately through the maximization process, we find that the constrained solution for amplitude becomes

$$
A^{(n)}\left(x_0,y_0\right) = \frac{\sum_{u=1}^{M} \sum_{v=1}^{M} \sum_{k=1}^{K} \left[\frac{d(u,v,r_k) P_{old}^{(n)}(x_0,y_0,r_k) h(u-x_0,v-y_0)}{I_{old}(u,v,r_k)} \right]}{\chi\left(x_0,y_0\right) + \sum_{u=1}^{M} \sum_{v=1}^{M} \sum_{k=1}^{K} \left[\frac{1}{\sqrt{2\pi}\sigma^{(n)}(x_0,y_0)} e^{-\frac{\left(r_k - r^{(n)}(x_0,y_0) \right)^2}{2\sigma^{(n)}(x_0,y_0)^2}} h\left(u-x_0,v-y_0\right) \right]}.
$$
(4.34)

If we now recall the assumption that the pulse is entirely within the range gate as well as the assumption on the PSF as shown in (4.19), the right hand term in the denominator of (4.34) will sum to one leaving us with a final iterative solution

$$
A^{(n)}\left(x_0,y_0\right) = \frac{\sum_{u=1}^{M} \sum_{v=1}^{M} \sum_{k=1}^{K} \left[\frac{d(u,v,r_k) P_{old}^{(n)}(x_0,y_0,r_k) h(u-x_0,v-y_0)}{I_{old}(u,v,r_k)} \right]}{\chi\left(x_0,y_0\right) + 1}.
$$
(4.35)

At this point, the only thing remaining is to derive the solution for the Lagrange multiplier. The derivative of Q_φ with respect to $\chi(x_0,y_0)$ easily simplifies to

$$
\frac{\partial Q_\varphi}{\partial \chi\left(x_0,y_0\right)} = \sum_{n=1}^{N} A^{(n)}\left(x_0,y_0\right) - A_c\left(x_0,y_0\right).
$$
(4.36)

Setting (4.36) to zero yields the following relationship:

$$\sum_{n=1}^{N} A^{(n)}(x_0, y_0) = A_c(x_0, y_0).$$ (4.37)

We can now substitute the solution from (4.35) into this relationship to allow us to find a solution for $\chi(x_0, y_0)$.

$$\sum_{n=1}^{N} \frac{\sum_{u=1}^{M} \sum_{v=1}^{M} \sum_{k=1}^{K} \left[\frac{d(u,v,r_k) P_{old}^{(n)}(x_0,y_0,r_k) h(u-x_0,v-y_0)}{I_{old}(u,v,r_k)} \right]}{\chi(x_0, y_0) + 1} = A_c(x_0, y_0)$$ (4.38)

The resultant solution for $\chi(x_0, y_0)$ is

$$\chi(x_0, y_0) = \frac{\sum_{n=1}^{N} \sum_{u=1}^{M} \sum_{v=1}^{M} \sum_{k=1}^{K} \left[\frac{d(u,v,r_k) P_{old}^{(n)}(x_0,y_0,r_k) h(u-x_0,v-y_0)}{I_{old}(u,v,r_k)} \right]}{A_c(x_0, y_0)} - 1.$$ (4.39)

At this point we have all of the necessary pulse parameter solutions in both a constrained and non-constrained fashion. By incorporating the PSF into our model we have enhanced the accuracy of the model and enabled the removal of the effects of diffraction. The subsequent results presented in this chapter will assume that the PSF is known. However, Chapter V will demonstrate that the average PSF parameterized by r_0 can be computed with the help of this algorithm.

4.3 Simulation

This work will report results from simulated 3-D FLASH LADAR data that was designed to mimic an ASC Tigereye™ camera. For this reason, simulation parameters were set to those published for the system.

4.3.1 Sensor Parameters.

Table 4.1 identifies the known specifications for the ASC sensor. Proper sampling

Table 4.1: ASC 3-D Tigereye FLASH LADAR System Specifications.

Known System Parameters	
Parameter Name	**Defined Value**
Frames per image	20
Laser wavelength (λ)	1.57 μm
Sample rate	420 MHz
Range delta per frame	0.357 m
Total range gate	7.14 m
Energy per pulse (E_t)	0.025 J
Sensor pulse width	$4.7 \times 10^{-9} s$
Detector Array Size	128×128
Pixel Size	100 μm $\times$ 100 μm
Lens Parameters for Simulation	
Parameter Name	**Defined Value**
Sensor focal length (f_l)	3 m
Aperture diameter (D)	2.325 cm
Instantaneous Field of View (iFOV)	0.24°

of the images is important due to the use of deconvolution in the algorithm. The maximum dimension, γ, on a pixel in the detector array must abide by the relationship [22]

$$\gamma \leq \frac{\lambda f_l}{2D}. \tag{4.40}$$

The factor of two in the denominator arises from the Nyquist sampling theorem which states we must sample at twice the maximum achievable spatial frequency, ν_{max}, as shown in (2.7). Therefore, given the known system specifications for the ASC system, the lens parameters were chosen as also shown in Table 4.1. While this is not a current commercially available lens configuration, the flexibility of simulation allows for selection of the optics parameters in order to ensure proper sampling of the simulated images according to (4.40). Ultimately the goal was to simulate the type of diffraction that would be experienced by an airborne platform incorporating

FLASH LADAR technology as a remote sensor at long slant ranges from the target. Therefore the parameter values for the simulation were chosen to allow the ratio of aperture diameter, D, to atmospheric seeing parameter, r_0, to be similar to what would be experienced in an airborne sensor application.

4.3.2 Target Profiles.

All targets for this simulation were designed such that all surfaces would produce returns within the range gate.

(a) 3-bar Target Range Image

(b) Obscured Target Range Image

(c) Multiple Void Target Range Image
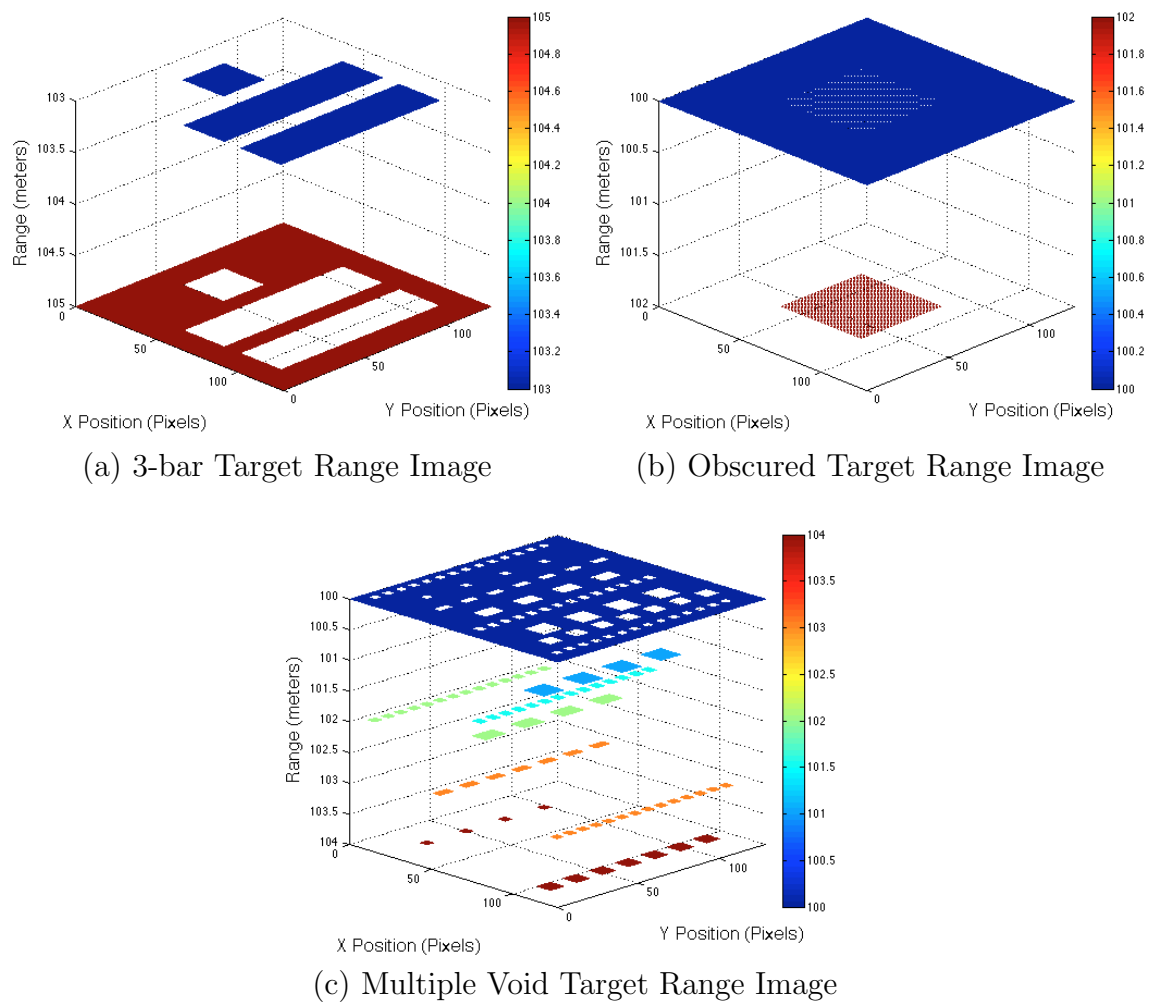
Figure 4.1: (a) The 3-bar target has an opaque background at a distance of 2 meters from the three separate opaque raised surfaces. (b) Has a foreground at a distance that is 2 meters from the partially obscured surface in the background. Only the center section of the foreground is transparent, the remainder of the surfaces are opaque. (c) Has an opaque foreground at a fixed distance, with an opaque background that varies from 1 to 4 meters from the foreground.

While the algorithm has demonstrated increased performance in multiple surface ranging for all tested profiles, this dissertation will consider three unique target profiles shown in Figures 4.1 and 4.2. The target profiles were designed to ensure that some pixels had various numbers of surfaces visible. In the case of the 3-bar target and multi-void target, only the edges of the features possessed multiple surfaces per pixel. However, the obscured target has an entire region in the center of the target where multiple surfaces are present. For the example targets shown, no pixel will have more than two surfaces visible. However, once the effects of diffraction are added in, some pixels may receive returns from additional surfaces depending on the severity of the simulated turbulence. Given the relatively short range gate for a single 3-D image, the number of surfaces in the included target profiles was limited to two. However, for a larger range gate the algorithm can easily be expanded to account for the general case of N surfaces [53].
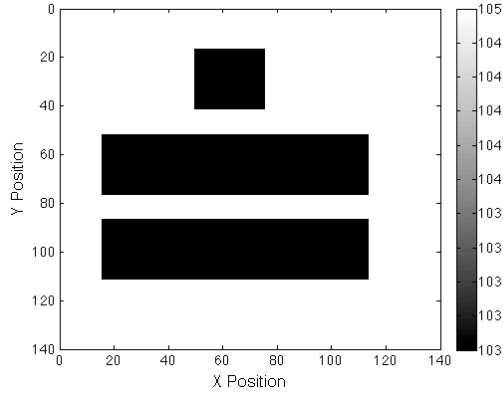
(a) 3-bar Target Range Image
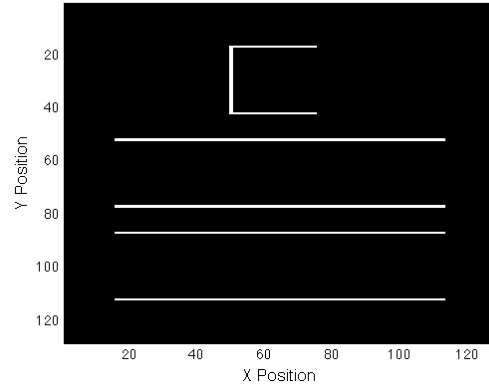
(b) Pixels with Multiple Surfaces
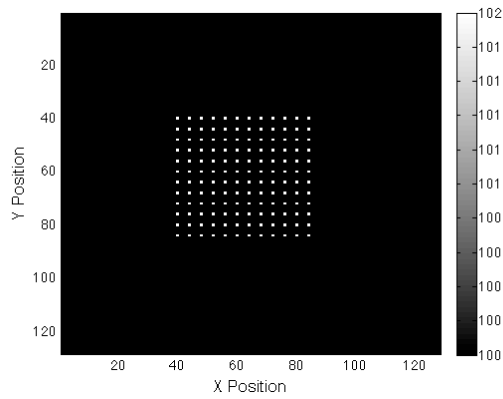
(c) Obsured Target Range Image
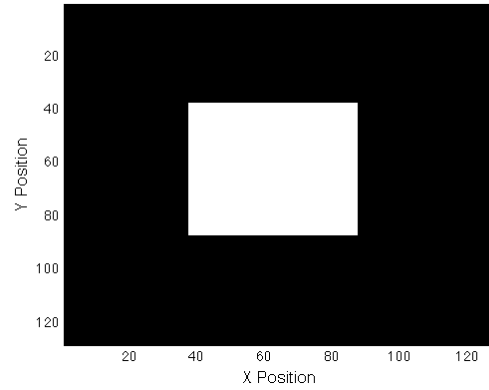
(d) Pixels with Multiple Surfaces
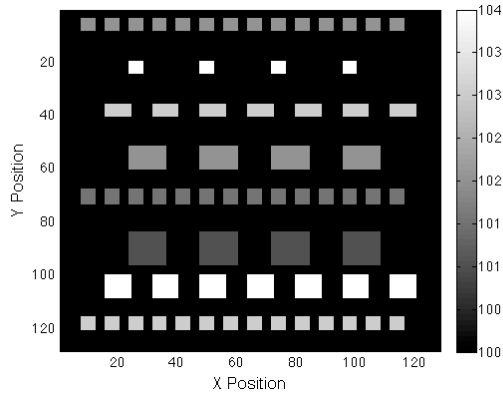
(e) Multiple Void Target Range Image
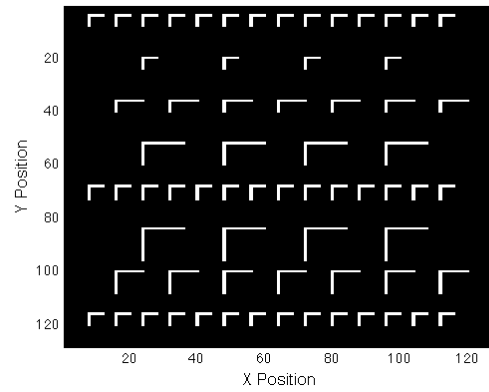
(f) Pixels with Multiple Surfaces

Figure 4.2: **(a) Has a background at a distance of 2 meters from the three separate raised surfaces. (b) The areas in white indicate the pixels whose iFOV contain 2 surfaces, while all remaining pixels have only a single surface visible in the iFOV. (c) Has a foreground at a distance that is 2 meters from the partially obscured surface in the background. (d) The areas in white indicate the pixels where the iFOV contains 2 surfaces. (e) Has a foreground at a fixed distance, with a background that varies from 1 to 4 meters from the foreground. (f) The areas in white indicate the pixels where the iFOV contains 2 surfaces.**

110

4.4 Mixture Modeling Considerations

Expectation Maximization in conjunction with Gaussian mixture modeling is a common technique employed to isolate the parameters of interest in the received LADAR data [46]. However, Zhuang points out that common challenges with employing EM in conjunction with Gaussian mixture modeling are determining the number of components in the mixture or isolating mixture components that may merge due to their individual parameters [69]. For various applications of Gaussian mixture modeling, Vlassis and Nikas solved the first problem with a Greedy EM approach. They performed an iterative process where the number of components was incrementally increased until the number corresponding with the solution with the highest likelihood was obtained [66]. Unfortunately, to employ this solution on the multi-surface detection problem including the effects of diffraction would be intractable due to the sheer volume of possibilities. For instance, if we consider a 128×128 array, where each detector may have between $0 - 2$ surfaces visible, we would have to consider 3^{16384} possible combinations for each image we wish to process. Additionally, it also seems intuitive that the maximum likelihood estimate will occur where the maximum possible number of surfaces are estimated since the algorithm will attempt to fit the noise inherent in the received signal. This research proposes a new solution to this problem. The Cap and Refine (CaR) strategy places an upper bound on the number of surfaces for which pulse parameters are generated. The respective pulse amplitudes will then be used to refine the number of surfaces visible in each detector.

4.4.1 Key Challenges with Multisurface Modeling.

In practice, the true upper bound on the number of surfaces visible by each detector could be established through various methods. Techniques such as the center-of-gravity and zero-crossing of the first derivative have been employed in the past with

success [67]. Based on the objectives of this research, the upper cap on the number of surfaces was fixed at two, but could easily be adjusted to account for the possibility of additional visible surfaces per pixel. The novelty for the approach employed by this research does not arise from the ability to define the upper cap on the number of surfaces. Rather, the novelty is that we can use the unique functionality of the MSID algorithm in conjunction with various detection schemes to efficiently estimate the number of components in our Gaussian mixture. Or in other words, once we have solved for the maximum possible components or surface returns, we can then discard those that are insignificant after a single execution of the MSID algorithm, rather than iteratively search for the best possible Gaussian mixture.
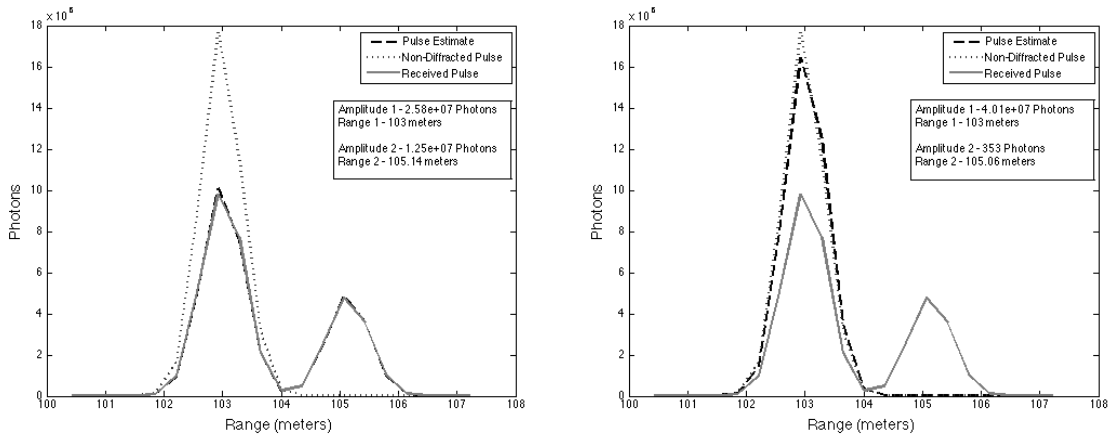
(a) Estimate not Accounting for Diffraction (b) Estimate Accounting for Diffraction

Figure 4.3: Comparison of pulses when the effects of diffraction were not accounted for (a), and when the effects of diffraction were incorporated into the estimation algorithm (b).

The MSID algorithm produces a number of amplitude, range and pulse width estimates for each detector based on the upper cap established. In cases where one or more of the surfaces either arises from effects due to diffraction, or in cases where there are no surfaces visible in the FOV, the corresponding estimates for amplitude will be driven towards zero. Due to the effects of noise and the residual effects from diffraction even after deconvolution, the algorithm may not perfectly drive undesired surfaces to

112

zero. In Figure 4.3 we consider two scenarios again with the 3-bar target from Figure 4.2(a). In Figure 4.3 (a) and (b), we plot the received pulse for pixel (55,75) in both an ideal case where the effects of diffraction are not present (non-diffracted pulse) as well as the actual received pulse where the image is both spatially and temporally blurred due to the effects of diffraction with $\frac{D}{r_0} \approx 2$. Since the selected pixel is two
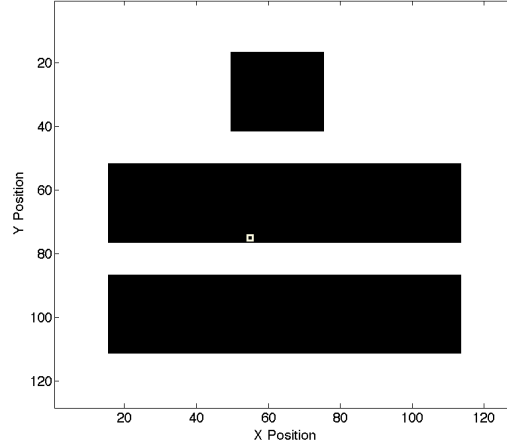
Figure 4.4: Identifies the location of the image pixel used.

pixels above the edge of one of the raised bars as shown in Figure 4.4, in the ideal scenario we would only expect to see a single pulse return at 103 meters. However, the effects of diffraction have caused some of the light that reflected off of the background at 105 meters to fall incident onto this detector as well, causing a temporal distortion which manifests as a second visible return in the received waveform. This presents one of the fundamental problems when performing multiple surface modeling where the collected images may be impacted by the effects of diffraction.

Figure 4.3 also demonstrates the utility of two techniques that could be employed for this multi-surface estimation problem. First we consider a traditional Gaussian mixture model, Figure 4.3(a), which does not incorporate the effects of diffraction in the estimation of the pulse. In this case we see that the technique estimates a pulse that closely matches the received pulse. The technique also extracts the amplitude

113

and range information for each of the two components in the mixture. However, once we incorporated the effects of diffraction through the MSID algorithm, we were able to drive the estimate for the second pulse towards zero as shown in Figure 4.3(b). While the second return is barely visible at this point, its amplitude is not perfectly zero, highlighting another key challenge associated with the multi-surface estimation problem.

At this point, a decision is required as to whether or not the reflection from a second surface represented by an amplitude of 353 photons is of interest or not. Clearly a classical detection approach could be employed where the threshold is determined by the noise variance. For instance, Stilla et al. compared the pulse amplitude to the standard deviation of the background noise. In cases where the pulse amplitude exceeded three times the standard deviation of the noise for at least the duration of the transmitted pulse, their initial classification was that a pulse was present [63]. They then used waveform-stacking to refine their classification of whether or not a surface of interest was truly present. While this detection algorithm is efficient to implement, the choice of threshold is somewhat arbitrary given the statistics used in our model. Additionally, the technique does not take advantage of the fact that we are using full waveform data.

4.4.2   Using Probability of False Alarm as Key Metric.

While perhaps not as efficient to implement as a simple threshold detection scheme, detection methods using waveform data can be shown to be extremely accurate [58]. Additionally, the performance of the technique can be adjusted to mission specific roles by simply adjusting the parameter of interest. For instance if we primarily wanted to minimize the possibility of detecting a surface that doesn't truly exist, we

could adjust the probability of false alarm, p_F. Given the following hypotheses:

H_0 - No surface is present in this pixel at this range

H_1 - Surface is present in this pixel at this range

the probability of false alarm is

$$p_F = p\left[H_1|H_0\right]. \tag{4.41}$$

At this point, we will be working with the estimates produced by the MSID algorithm in conjunction with the measured data. Ultimately, the goal is to determine the amplitude threshold that will ensure we exceed the user defined threshold for p_F. Any surfaces with amplitude estimates below this threshold could be discarded and classified as the algorithm's attempt to fit a pulse to the noise.

In order to execute this detection strategy we also need to establish the Likelihood Ratio Test (LRT). For purposes of this research we will consider equal prior probabilities and equal costs allowing

$$\Lambda = \frac{p\left(D|H_1\right)}{p\left(D|H_0\right)} > 1 \text{ say } H_1. \text{ Otherwise say } H_0 \tag{4.42}$$

where D is a pulse return with amplitude corresponding with the threshold we wish to test [58]. If prior knowledge of the scene is available, this test could be adjusted to potentially allow for better performance. Given the pulse width and bias estimates that were found using the MSID algorithm, we can find the amplitude threshold that satisfies the user defined value for p_F. Unfortunately due to the fact that we are using full waveform data, a closed form solution for the amplitude threshold does not exist. However, Monte Carlo methods could be employed to obtain this threshold [58].

Using the width parameter generated from the MSID algorithm, we can simulate

numerous independent noisy waveforms. Using the measured or estimated bias level, we can predict the noise variance in the signal. The amplitude of the simulated noisy return can be gradually increased. For each amplitude level, p_F is computed [58]. Our amplitude threshold is established once we reach the user defined value for p_F. In this manner, we can compute a threshold that varies with the width of the received pulse.

While this process can be considered computationally intensive, it would be possible to compute the threshold in advance for a range of pulse width and bias values and store them in a lookup table since each amplitude threshold is entirely dependent on these values. Computing the values in advance could easily allow for a test that could be executed in real time. Demonstration of this technique for a $p_F = 0.01$ in conjunction with the performance gains from the MSID algorithm are detailed in the following section.

4.5   Results

The following results will demonstrate the performance enhancements of the algorithm developed through this research over traditional Gaussian mixture modeling. Various algorithms were tested against MCFA images, where each MCFA image is composed of 30 separate 3-D images. Using the MCFA images serves to improve the SNR. First, we must consider a metric by which the algorithms will be compared.

4.5.1   Range Accuracy Measurement.

In the case of the multi-surface problem, comparing the performance of the techniques is not simply a matter of looking at the difference between the range estimate and the true value. We must also consider the true number of ranges present for each pixel and the algorithm's ability to accurately predict both the number of surfaces

visible as well as the true range to that surface. The following method will be used to compare the performance of the algorithms. For this work, we again assume that the max number of surfaces visible in any one image pixel is two. However, this technique will also scale as the number of surfaces increases.

In a 3-D FLASH LADAR system we are primarily concerned with the accurate ranging to the target, but amplitude also plays a key role in visual depiction of the target. Since the algorithms mentioned above are initially hard-coded to force each pixel to have the maximum number of surfaces, we must balance both the predicted range and amplitude. The following range accuracy measurement will consider the RMSE between the predicted and true ranges weighted by the predicted amplitudes. In that manner we will not penalize any of the algorithms for predicting a false range if the corresponding amplitude is driven to zero or more specifically below the threshold established by the techniques listed in Section 4.4.2. However, if an algorithm falsely predicts a range, it will be penalized based on the amplitude corresponding to the falsely predicted range. For instance, (4.43) demonstrates the error calculation if the algorithm correctly predicts that there are two surfaces present for a pixel, (4.44) is the error calculation for a pixel that only has one surface present but the algorithm predicts two and (4.46) is the case where one surface is present and the algorithm correctly predicts this.

$$\epsilon_{2,2} = A^{(1)}(x,y)\left(r^{(1)}(x,y) - r^{(1)(true)}(x,y)\right)^2 + A^{(2)}(x,y)\left(r^{(2)}(x,y) - r^{(2)(true)}(x,y)\right)^2$$
$$(4.43)$$

$$\epsilon_{2,1} = A^{(1)}(x,y)\left(r^{(1)}(x,y) - r^{(true)}(x,y)\right)^2 + A^{(2)}(x,y)\left(r^{(2)}(x,y) - r^{(true)}(x,y)\right)^2$$
$$(4.44)$$

$$\epsilon_{1,2} = A^{(1)}(x,y)\left(r^{(1)}(x,y) - r^{(1)(true)}(x,y)\right)^2 + A^{(1)}(x,y)\left(r^{(1)}(x,y) - r^{(2)(true)}(x,y)\right)^2$$
$$(4.45)$$

$$\epsilon_{1,1} = A^{(1)}(x,y)\left(r^{(1)}(x,y) - r^{(true)}(x,y)\right)^2 \qquad (4.46)$$

117

Once the error, $\epsilon_{predicted,true}$, is computed for each pixel, the mean error is taken over the entire image and divided by the mean amplitude of all estimated surfaces. Finally, the square root of this value is taken, giving us an error value with units of meters. This final value will be used to judge the accuracy of the algorithm.

4.5.2 Comparison of Algorithms.

This section will compare four multi-surface estimation techniques against the three target profiles listed in Figure 4.2. The primary metric that will be used to judge overall performance will be the range accuracy measurement listed in Section 4.5.1. The techniques will be tested against images with various levels of range diversity as well as two levels of atmospheric turbulence based on r_0 values of 1 cm and 2 cm.
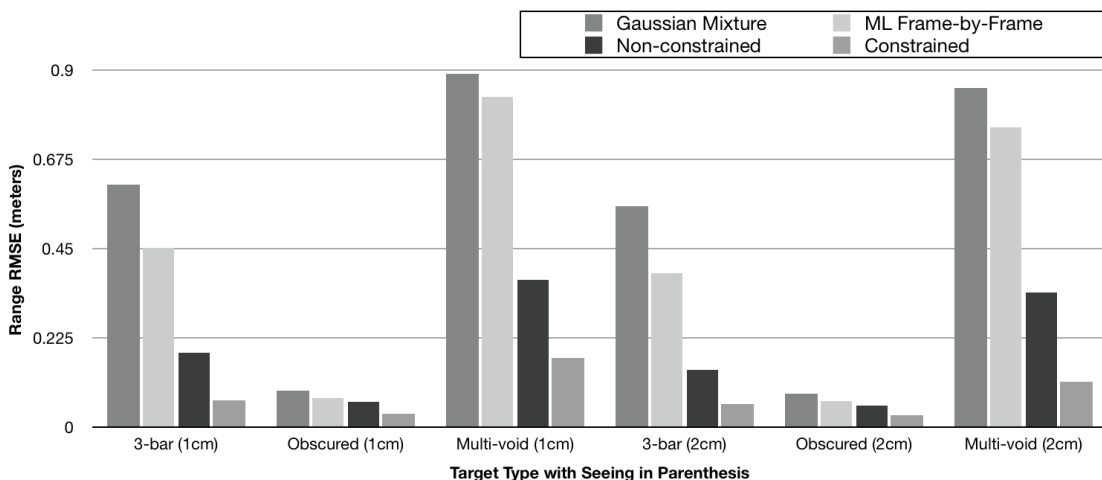
Figure 4.5:   Range RMSE Comparison.

The first technique under consideration was a simple Gaussian decomposition using an EM technique. This technique will essentially fit the best possible two-component per pixel Gaussian mixture to the received data without considering the effects of diffraction. The second technique was to use the ML estimate (3.9) on each frame of the 3-D image prior to estimation of the individual surfaces. Third, we will

look at the performance of the originally developed non-constrained MSID algorithm [53]. Finally, we will look at the constrained MSID algorithm [52].

From the results in Figure 4.5 it is visible that the constrained MSID algorithm obtains the best performance for the estimation problem for each of the target profiles considered. The overall magnitude for RMSE is highly dependent on target type; however, the observed trend on algorithm performance was similar across all target types. The improvements of the constrained MSID algorithm compared with non-constrained MSID algorithm were only slight in some cases. However, the ability to accurately predict the number of surfaces visible by the detector in conjunction with the CaR technique was significantly enhanced when using the constrained MSID algorithm.

The true numbers of surfaces visible by each detector under ideal conditions are shown in Figure 4.2. When compared with the truth, the constrained MSID algorithm clearly outperforms the other techniques as shown in Figure 4.6 for the 3-bar target blurred by an OTF with an r_0 of 2 cm. Here, the pixels that are estimated to have two surfaces visible are indicated in white. The pixels where the amplitude of only a single surface is determined to be significant are either gray or black. The determining factor for which surface is used to estimate an individual return is based on the initialization value for range. The results from this test were used to finalize the optimal mixture of components based on the estimated data. The constrained MSID algorithm demonstrated the best ability to drive false surfaces towards zero making it easier to develop an accurate mixture model using the CaR technique. For comparison purposes similar results were produced for the obscured target in Figure 4.7 and the multi-void target in Figure 4.8. For each of the target types, the constrained MSID algorithm demonstrated the best ability to eliminate false surfaces that appear due to noise or diffraction effects.
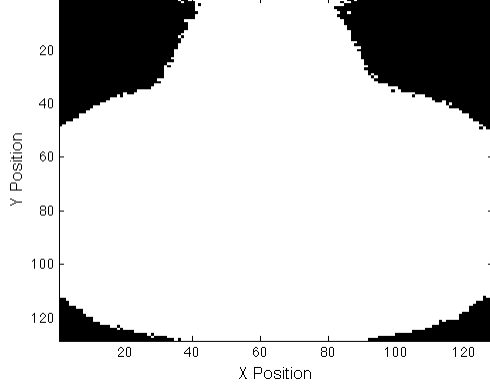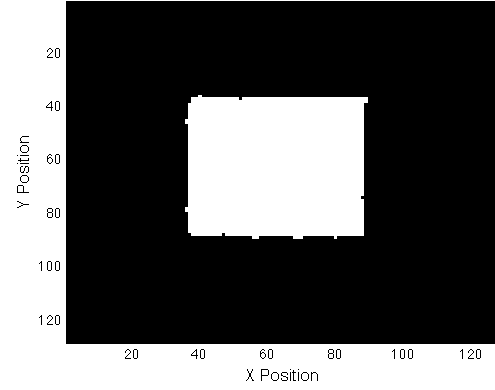
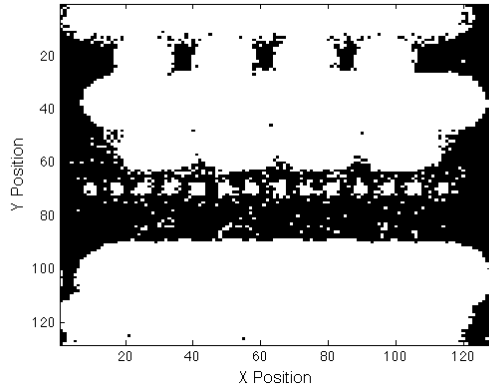(a) Gaussian Mixture
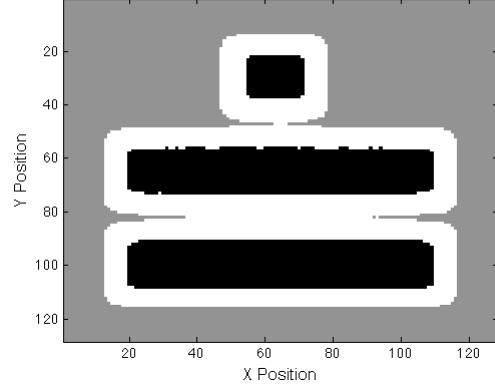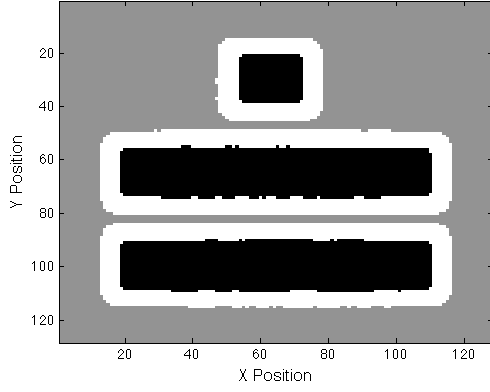
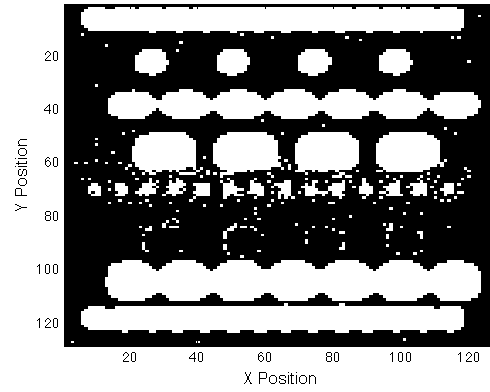(b) ML Frame-by-Frame
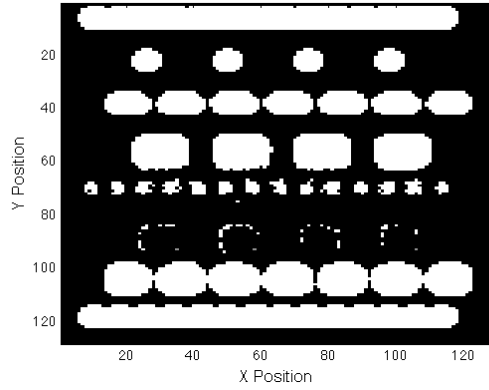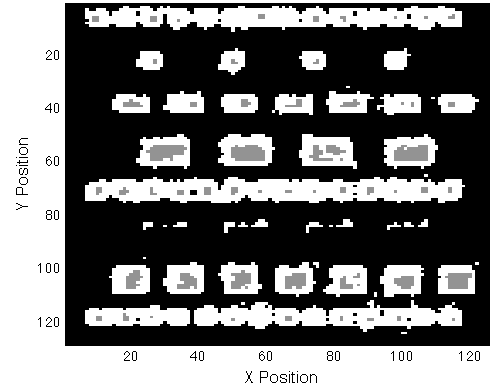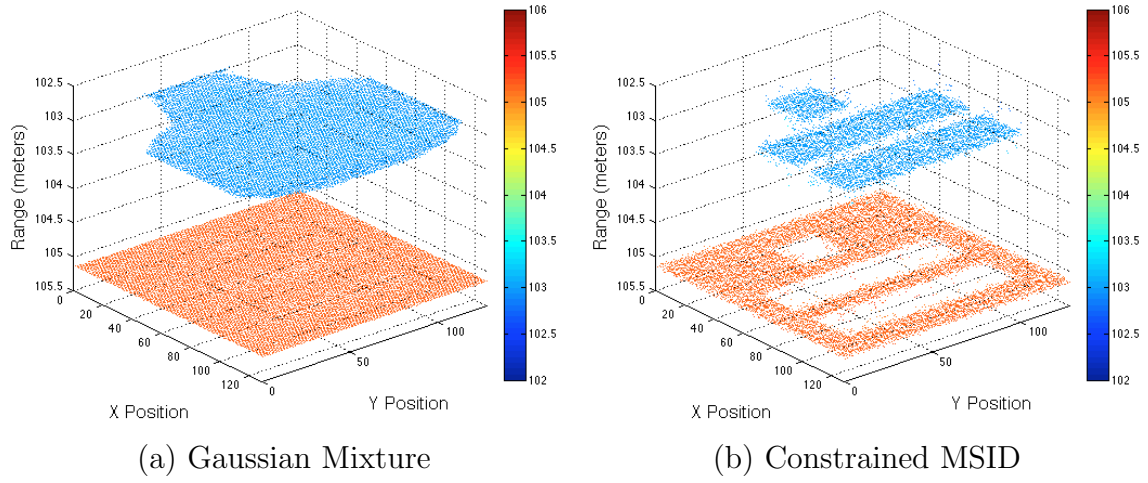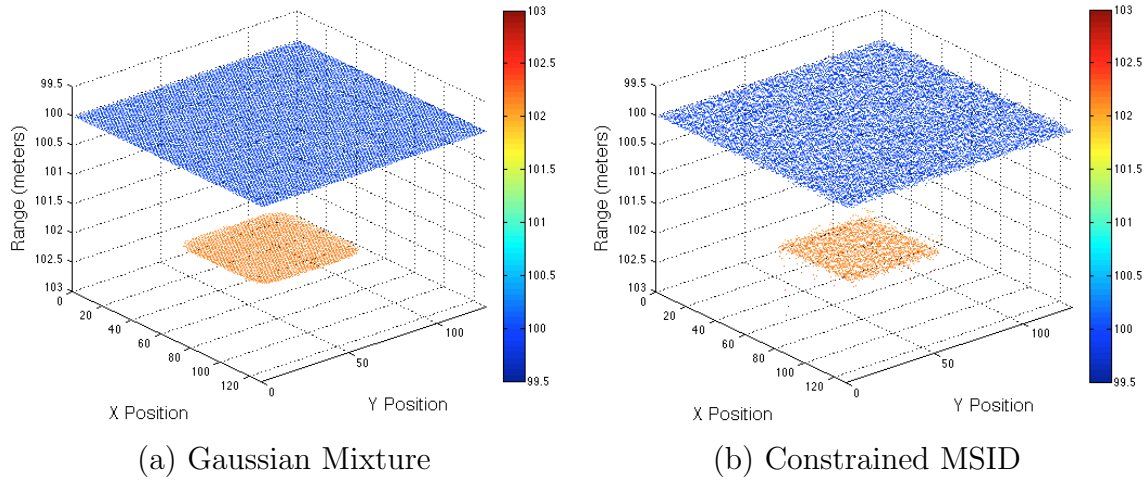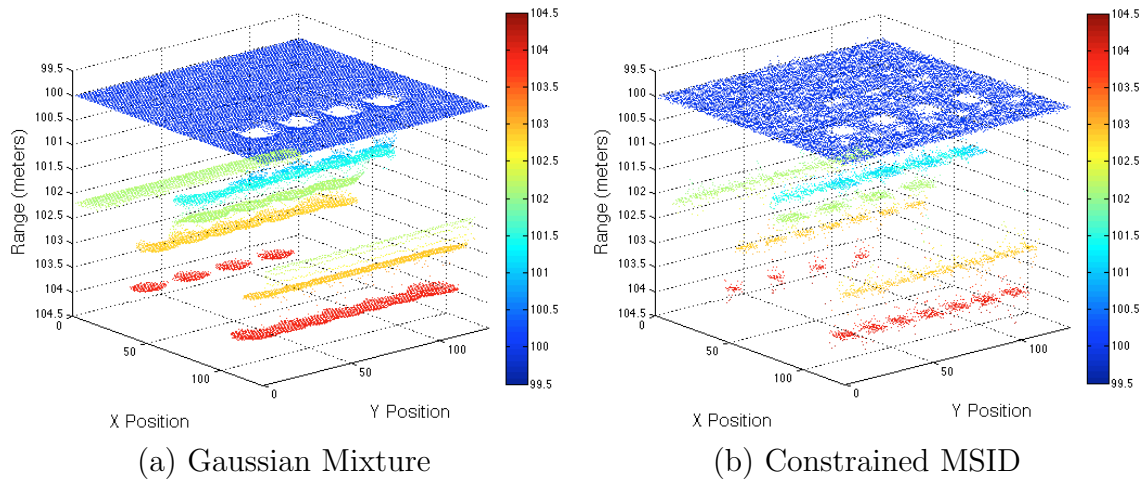

(c) Non-constrained MSID
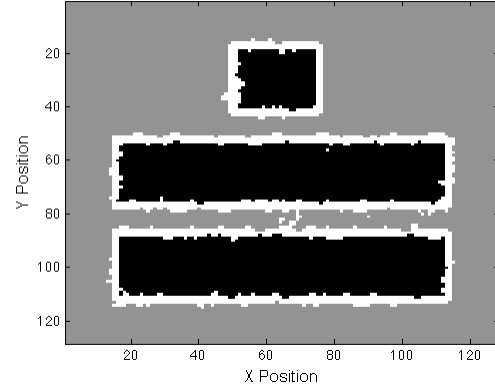
(d) Constrained MSID

Figure 4.6: **Surface prediction using CaR technique with** $r_o = 2cm$ **for (a) Gaussian mixture EM algorithm without including the effects of diffraction, (b) RL Frame-by-Frame deconvolution technique, (c) non-constrained MSID algorithm and (d) the constrained MSID algorithm. The pixels where the amplitudes of both surfaces yield a detection are indicated in white. The pixels where the amplitude of the second surface,** $A^{(2)}(x, y)$**, was the only one of significance are indicated in gray. Finally, the pixels where the amplitude of the first surface,** $A^{(1)}(x, y)$**, was the only one of significance are indicated in black.**
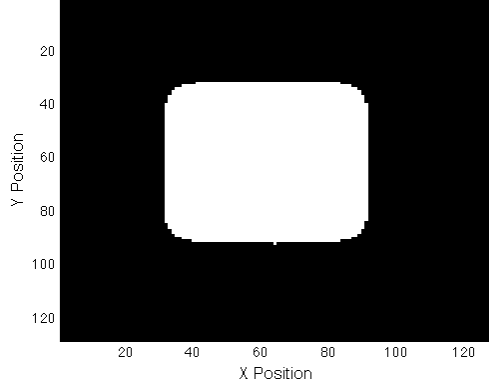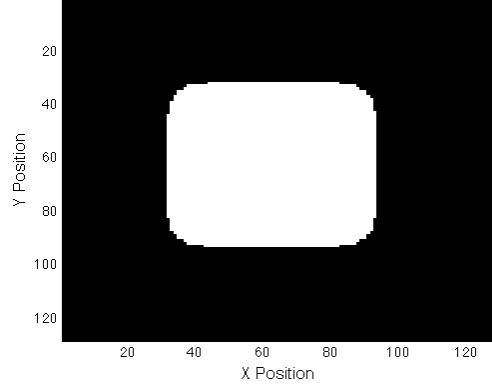
(a) Gaussian Mixture
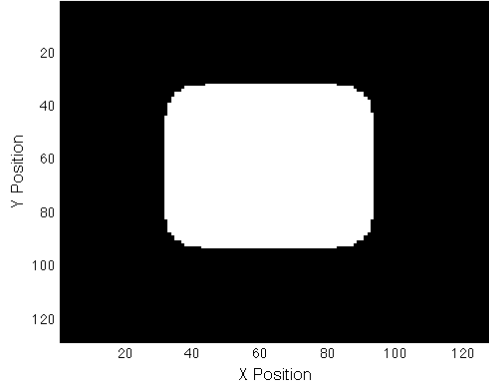
(b) ML Frame-by-Frame

(c) Non-constrained MSID

(d) Constrained MSID

Figure 4.7: Surface prediction using CaR technique with $r_o = 2cm$ for (a) Gaussian mixture EM algorithm without including the effects of diffraction, (b) RL Frame-by-Frame deconvolution technique, (c) non-constrained MSID algorithm and (d) the constrained MSID algorithm. The pixels where the amplitudes of both surfaces yield a detection are indicated in white. The pixels where the amplitude of the second surface, $A^{(2)}(x,y)$, was the only one of significance are indicated in gray. Finally, the pixels where the amplitude of the first surface, $A^{(1)}(x,y)$, was the only one of significance are indicated in black.

(a) Gaussian Mixture   (b) ML Frame-by-Frame

(c) Non-constrained MSID   (d) Constrained MSID

Figure 4.8: **Surface prediction using CaR technique with $r_o = 2cm$ for (a) Gaussian mixture EM algorithm without including the effects of diffraction, (b) RL Frame-by-Frame deconvolution technique, (c) non-constrained MSID algorithm and (d) the constrained MSID algorithm. The pixels where the amplitudes of both surfaces yield a detection are indicated in white. The pixels where the amplitude of the second surface, $A^{(2)}(x,y)$, was the only one of significance are indicated in gray. Finally, the pixels where the amplitude of the first surface, $A^{(1)}(x,y)$, was the only one of significance are indicated in black.**

(a) Gaussian Mixture

(b) Constrained MSID

Figure 4.9: Comparison of 3-D surface returns for 3-bar target using a (a) Gaussian mixture EM algorithm without including the effects of diffraction, and (b) the constrained MSID algorithm which accounts for the effects of diffraction. By including the effects of diffraction, our estimate of the 3-D target is significantly more accurate when compared to the truth in Figure 4.1 (a).

(a) Gaussian Mixture

(b) Constrained MSID

Figure 4.10: Comparison of 3-D surface returns for obscured target using a (a) Gaussian mixture EM algorithm without including the effects of diffraction, and (b) the constrained MSID algorithm which accounts for the effects of diffraction. By including the effects of diffraction, our estimate of the 3-D target is significantly more accurate when compared to the truth in Figure 4.1 (b).

123

(a) Gaussian Mixture   (b) Constrained MSID

Figure 4.11: **Comparison of 3-D surface returns for multiple void target using a (a) Gaussian mixture EM algorithm without including the effects of diffraction, and (b) the constrained MSID algorithm which accounts for the effects of diffraction. By including the effects of diffraction, our estimate of the 3-D target is significantly more accurate when compared to the truth in Figure 4.1 (c).**

In Figures 4.12, 4.13 and 4.14 we compare the range error by pixel for the various target profiles from Figure 4.2 for each of the four multi-surface ranging techniques. The results provide an intuitive explanation for the variation in range RMSE. The traditional Gaussian decomposition strategy has minimal range error when there are truly two surfaces to estimate, such as in the center of the image for the obscured target. However, near the edges of the obscuration where some of the reflected light from the far surface diffracts onto neighboring pixels we experience an increase in range error as expected. By using the ML estimate on each frame of the 3-D data, we can reduce this error somewhat, though largest reductions in error occur when the effects of diffraction are directly incorporated into the multi-surface ranging algorithm. On the 3-bar target and the multi-void target, we again see that as the light from different surfaces is diffracted to neighboring areas of the image, we experience higher levels of error.
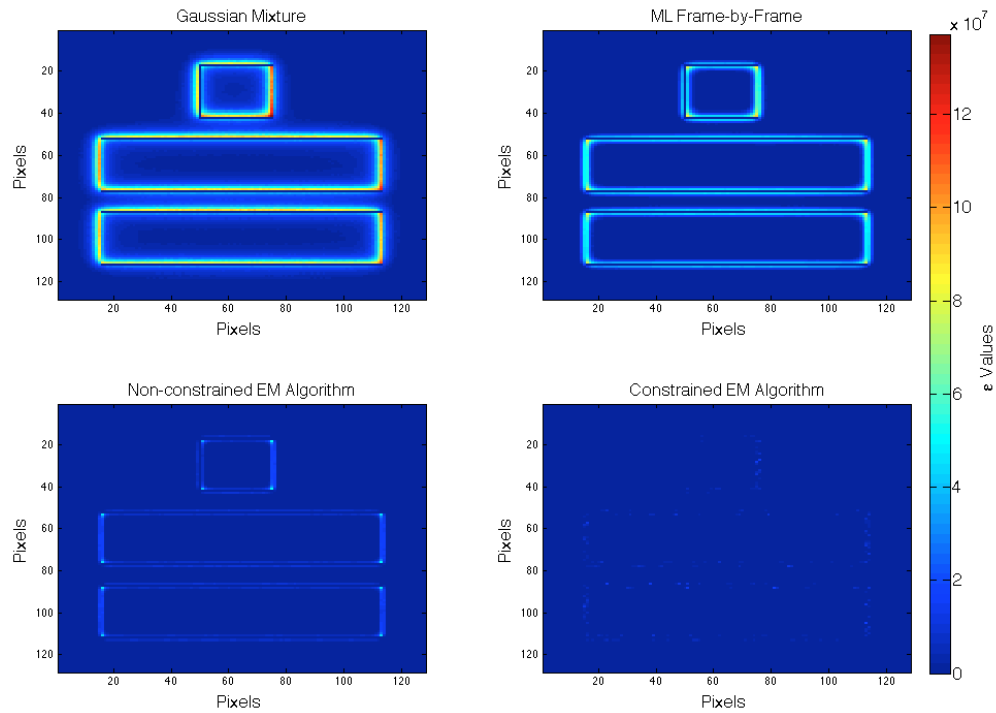
Figure 4.12:   3-Bar target range error by pixel comparison (meters^2).
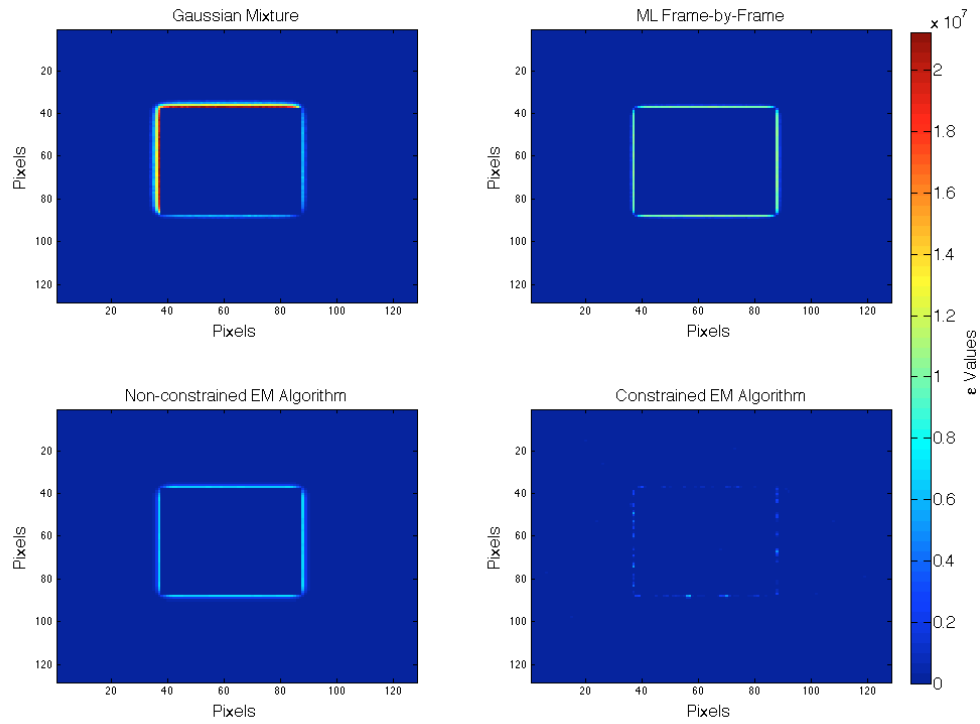
Figure 4.13: Obscured target range error by pixel comparison (meters^2).
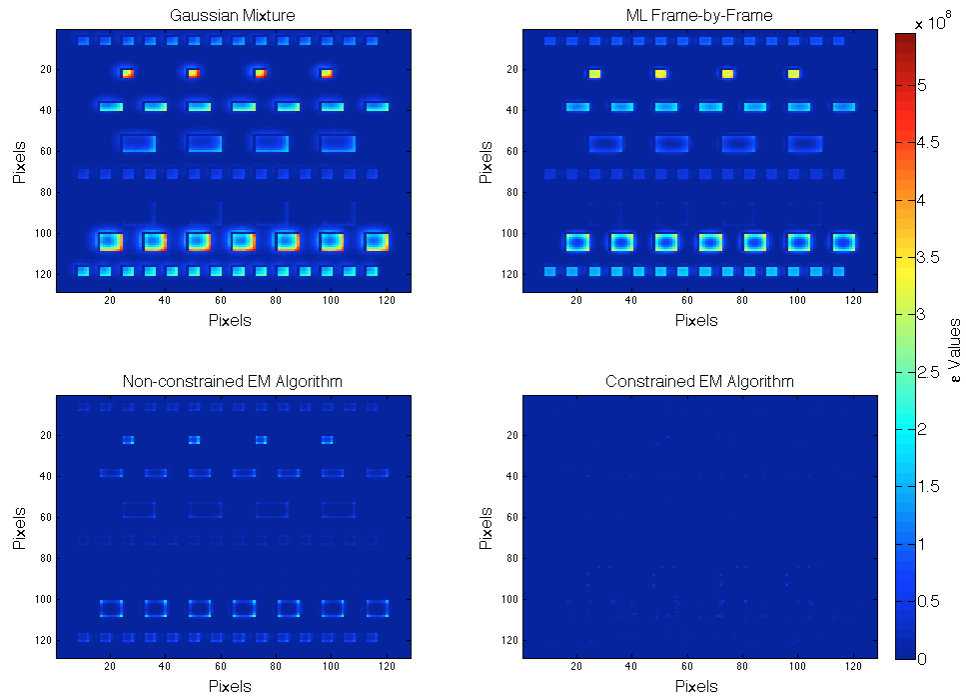
Figure 4.14: Multi-void target range error by pixel comparison (meters^2).

4.6 Chapter Summary

By incorporating the effects of diffraction, the MSID algorithm developed through this research allows for significant enhancement to the multi-surface estimation problem when properly sampled images are taken through atmospheric turbulence. Two variations of the MSID algorithm were developed. First, direct solutions for the pulse return parameters and pixel bias were derived. Second, a constraint on the amplitude was applied which allowed for much more refined pulse return estimates. Rather than employ deconvolution techniques that are tailored for 2-D images, both approaches incorporate the effects of diffraction into the Gaussian mixture model. Additionally, the MSID algorithm simultaneously solves for range, pulse width and amplitude for multiple surfaces per detector while enhancing pulse returns that may have been diminished due to the diffractive effects of the atmosphere.

Through the incorporation of the effects of diffraction into the algorithm, the ill effects of temporal and spatial distortion were simultaneously reduced. The results obtained from the MSID algorithm were superior to those obtained through more traditional techniques. Simulation examples show that the MSID algorithm derived in this work improves range estimation over standard Gaussian mixture modeling and frame-by-frame deconvolution on average by 89% and 85% respectively based on range RMSE calculations. Current limitations on the technology limit the ill effects when imaging through turbulence, but as technology improves and resolution of the detectors increases, the ill effects will become significantly more pronounced.

Given the technical challenges associated with the manufacturing of these sensors, the issue of proper sampling appears to be a considerable hurdle to overcome for many applications. However, the goal of this research was to demonstrate the promise of the novel technique presented in this chapter on multiple surface ranging in the presence of atmospheric aberrations. Additionally, the MSID algorithm would have current

applicability where sensors with very long focal lengths are employed. For instance, employing a 3-D FLASH LADAR in conjunction with an astronomical telescope could facilitate the sampling required. An optical system of this nature could yield benefits in SSA.

V. 3-D FLASH LADAR Parameterized Blind Deconvolution

This chapter focuses on the development of a novel blind deconvolution algorithm employed on properly sampled 3-D FLASH LADAR images. This research will build upon the MSID algorithm previously developed to minimize the effects of diffraction on 3-D FLASH LADAR while producing accurate ranging to multiple surfaces [52]. Using an enhanced version of this algorithm and considering the range diversity inherent in 3-D images allows for simultaneous estimation of the parameterized PSF and spatial / temporal enhancement of the image. Simulation results will be presented to demonstrate the utility of this algorithm in controlled cases where the true PSF is known [51]. Experimental results will also be presented where the PSF can be measured.

As previously mentioned, parameterized blind deconvolution for 2-D images is an ill-posed problem. While solutions have been developed that can overcome this hurdle, additional assumptions or approximations are often required. Using a likelihood maximization approach, this research will show that by adding range diversity through 3-D imaging, parameterized blind deconvolution is no longer an ill-posed problem.

This chapter is organized as follows: Section 5.1 details the system of equations that leads to an over-determined problem when dealing with properly sampled FLASH 3-D images. In Section 5.2 the strategy for finding the parameterized OTF is provided. Section 5.3 presents the parameters and target profiles used for simulation and Section 5.4 presents the findings when using actual experimentally collected images impacted by atmospheric turbulence.

5.1 Joint Estimation of Image and Atmospheric Seeing - System of Equations

Previous work presented in Chapter IV assumed that the PSF was known, and simultaneously provided iterative solutions for pulse amplitude, range, width and bias. Using the MSID algorithm we will now show that through the simultaneous estimation of all of the visible surfaces for each detector, we can also accurately identify the PSF parameterized by r_0. Both the constrained and non-constrained MSID algorithm have been tested with success. However, the advantage with using the non-constrained algorithm for this application is that we do not need to first perform a deconvolution on the 2-D representation of the received image. A potential employment strategy would be to first use the non-constrained MSID algorithm to find the optimal parameterized PSF. We could then use this optimal parameterized PSF in conjunction with the constrained MSID algorithm to further refine the estimate.

It is through this joint estimation that we are able to fully demonstrate the utility of this multiple surface ranging capability for minimizing the spatial and temporal blurring in a tactical environment. Using the average atmospheric models in (2.10) and (2.11) the OTF is reduced to a single unknown, r_0. The ability to find this single unknown for the OTF, and its Fourier relationship to the PSF can be considered a solution to the parameterized blind deconvolution problem.

While the problem of parameterized blind deconvolution is ill-posed for 2-D images, for 3-D images it is possible that the problem may be over-determined. The over-determined nature of the problem is derived from the fact that we are using 3-D images where the total image is collected in an extremely short time span. The laser pulse is of such a short duration, that the atmosphere can be considered static and a single PSF is applied to all range slices in the image [21]. The 2-D system of

equations is

$$I(u, v) = \sum_{x,y=1}^{M} o(x, y) h(u - x, v - y | r_0) \qquad (5.1)$$

where i is the image estimate, o is the object we are trying to estimate and our PSF, h, is parameterized by r_0. Here we have a total of M^2 equations, but we have $(M^2 + 1)$ unknowns, since for every image we have both an object sampled by M^2 pixels and a unique PSF. The 3-D system of equations is

$$I(u, v, r_k) = \sum_{n=1}^{N} \sum_{x,y=1}^{M} P^{(n)}(x, y, r_k) h(u - x, v - y | r_0) + B(u, v) \text{ for } k = \{1 : K\}$$

$$(5.2)$$

where K is the total number of range samples or frames in the image. For 3-D images we therefore have KM^2 equations but only $(3N + 1)M^2 + 1$ unknowns, since we want to estimate amplitude, range and pulse width for each return, bias for the detector and r_0 for the PSF. Therefore, we now have the possibility for an over-determined problem if the condition

$$K \geq 3N + 2 \qquad (5.3)$$

is satisfied, since K must be an integer. In addition to the condition in (5.3), the targeted scene must also have range diversity in order to prevent an ill-posed problem.

5.2   Maximum Likelihood Solution for Atmospheric Seeing

The goal of this work is to show that likelihood can be maximized through joint estimation of range, amplitude, pulse width, bias and atmospheric seeing. Given the joint probability of the received data as shown in (2.6) the log-likelihood, L, can be computed as

$$L = \sum_{u,v=1}^{M} \sum_{k=1}^{K} [d(u, v, r_k) \ln(I_{tot}(u, v, r_k)) - I_{tot}(u, v, r_k) - \ln(d(u, v, r_k)!)]. \qquad (5.4)$$

In (5.4), the final term, $d(u, v, r_k)!$ is a constant that does not vary as we search for the correct value of r_0 to maximize likelihood. Therefore, we simply seek to maximize this adjusted likelihood function, L_φ,

$$L_\varphi = \sum_{u,v=1}^{M} \sum_{k=1}^{K} \left[d\left(u, v, r_k\right) \ln \left(I_{tot}\left(u, v, r_k\right)\right) - I_{tot}\left(u, v, r_k\right) \right]. \tag{5.5}$$

5.3   Simulation

This work will report results from simulated 3-D FLASH LADAR data that was again designed to mimic an ASC Tigereye camera. For this reason, simulation parameters were set to those published for the system as shown in Table 4.1. This section will be broken down into three main parts. First we will present the target profiles considered. Second, we will show how range diversity is critical to the ability to jointly estimate the pulse, bias and atmospheric seeing. Finally, we will show that joint estimation of multiple surfaces is required in order to solve this problem.

5.3.1   Simulated Target Profiles.

Each simulated 3-D image will consist of 20 individual data frames. With a sample rate of 420 MHz, each 128×128 pixel data frame will represent a range delta of approximately 0.357 m for a total range gate of 7.14 m. All targets for this simulation were designed such that the surfaces would produce returns within the range gate. Target profiles were selected to illustrate the dependence on range diversity. This paper will consider three unique target profiles shown in Fig. 5.1. With the exception of the flat target in Fig. 5.1(a), the target profiles were designed to ensure that there was range diversity throughout the scene. The flat target was designed to show that likelihood cannot be maximized using the techniques described in this paper without range diversity in the scene.
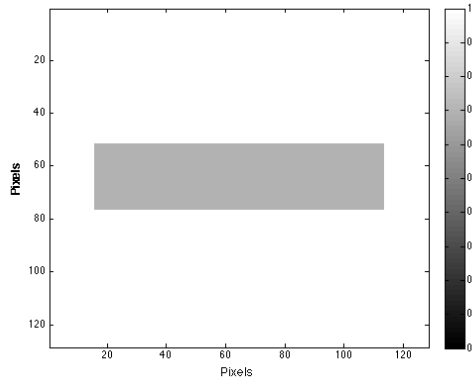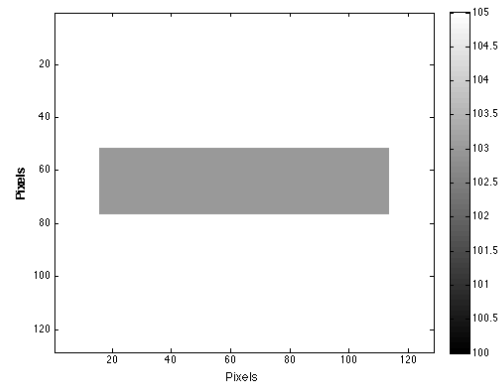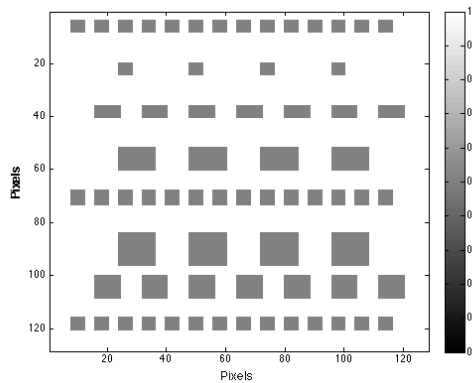
(a) Flat target - reflectivity
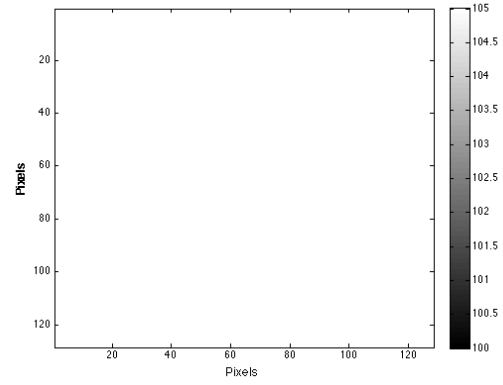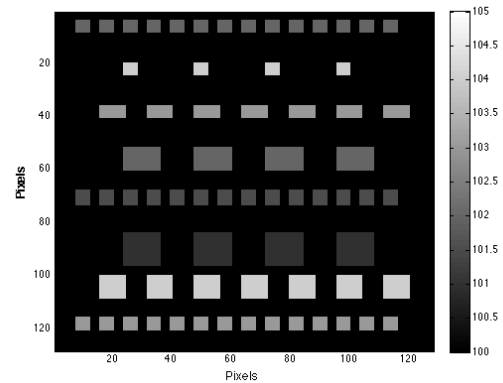
(b) Flat target - range
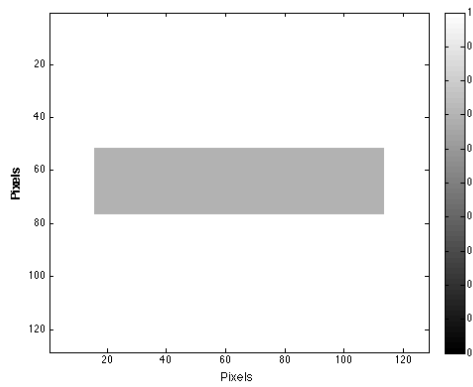
(c) Single bar target - reflectivity

(d) Single bar target - range

(e) Multi void target - reflectivity

(f) Multi void target - range

Figure 5.1: **(a) The flat target has a single bar in the center with lower reflectivity. (b) The flat target is at a range of 105 meters across the entire sensor field of view. (c) The single bar target again has a single bar in the center with lower reflectivity. (d) Additionally, the single bar target has range diversity since the background is at 105 meters, and the single raised bar in the center is at 103 meters. (e) The multiple void target has numerous voids with lower reflectivity. (f) The multi void target has the entire foreground at 100 meters and various size voids at ranges between 101 and 104 meters.**

5.3.2 Range Diversity and Likelihood Maximization.

The simulation results were obtained by first executing the multi-surface ranging algorithm on an image ensemble consisting of an average of 30 individual 3-D images across a range of r_0 values from 0.001 m to 0.025 m. Image averaging was used to improve SNR and the frames were properly registered making the employment of the average short exposure OTF (2.10) valid. The adjusted likelihood was then computed according to (5.5), and the optimal solution was chosen as the one that maximized likelihood. The results below will focus on the ability to accurately estimate the value for r_0, since the results in Chapter IV demonstrated the capability of the MSID algorithm given a known value for r_0.

Figure 5.2 shows the adjusted likelihood with respect to r_0 for each of the targets identified in Figure 5.1. In each case, the simulated image for the target was developed using 1 cm for the true value of r_0. As expected, the flat target did not allow for maximization of r_0 at the correct value. Rather, likelihood continued to increase with increasing r_0. On the other hand, both the single bar target and the multi void target allowed for maximization of likelihood at the correct value of 1 cm.
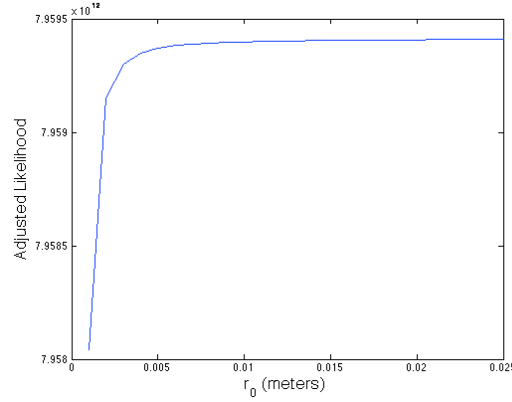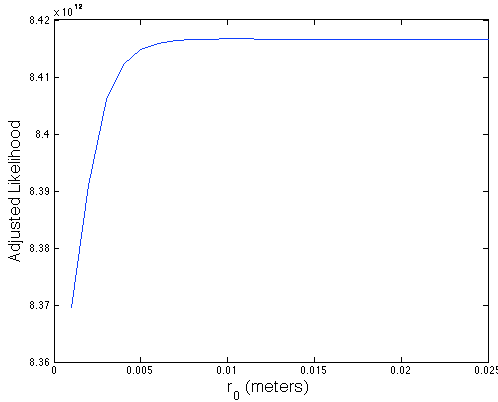
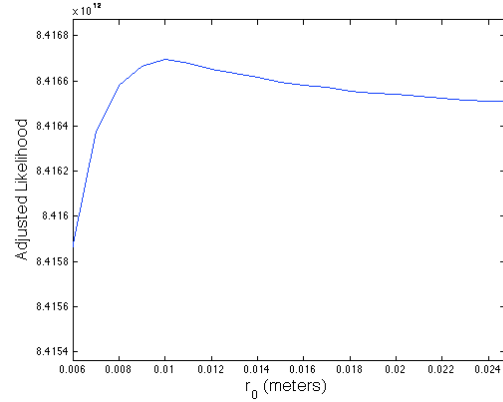(a) Flat target - Likelihood vs r_0
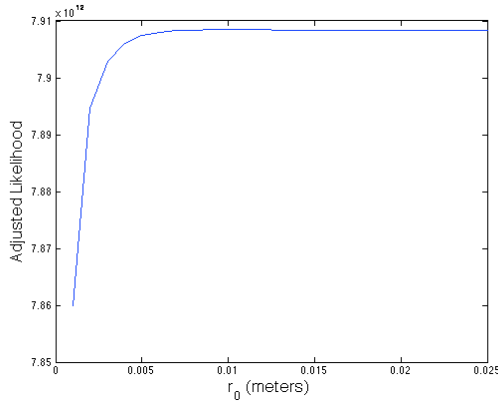
(b) Single bar target - Likelihood vs r_0
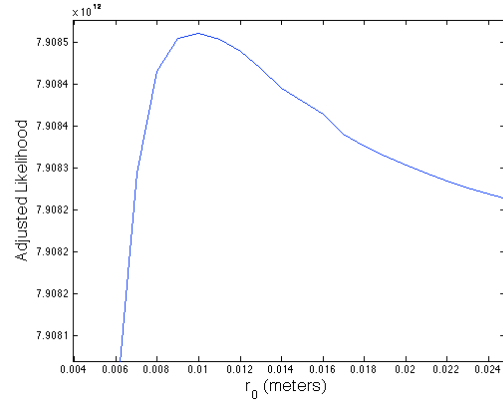
(c) Single bar target - zoom view


(d) Multi void target - Likelihood vs r_0

(e) Multi void target - zoom view

Figure 5.2: **(a) The flat target has a continuously increasing likelihood with respect to increasing levels of r_0 (b) The single bar target has a small amount of range variance throughout the image, yet likelihood is maximized. (c) Upon zooming in, likelihood is clearly maximized at the correct value of 1 cm for the single bar target. (d) The multi void target has far more range diversity, and likelihood is again maximized. (e) Upon zooming in, likelihood is clearly maximized at the correct value of 1 cm for the multi void target.**

135

5.3.3 Joint Estimation of Multiple Surfaces.

It should be noted that accurate results are far more likely for this joint estimation problem if simultaneous estimation of all surfaces is accomplished. Since blurring occurs both temporally and spatially, we must account for both if we want to identify the correct blurring function using this algorithm. The single bar target was designed such that each pixel would have at most two surfaces in its FOV. Additionally, only the pixels with an FOV that contained the edges of the bar would have more than a single surface if diffraction effects were not present. By constraining the algorithm so that we solve for at most one surface per pixel, the ability to predict an accurate level for r_0 is significantly degraded. This is likely due to the fact that the system of equations in (5.2) no longer applies. Figure 5.3 shows that the maximum likelihood value does not occur at the correct value of $r_0 = 1$ cm when we only estimate a single surface per pixel. Instead, likelihood is maximized at $r_0 = 0.5$ cm.
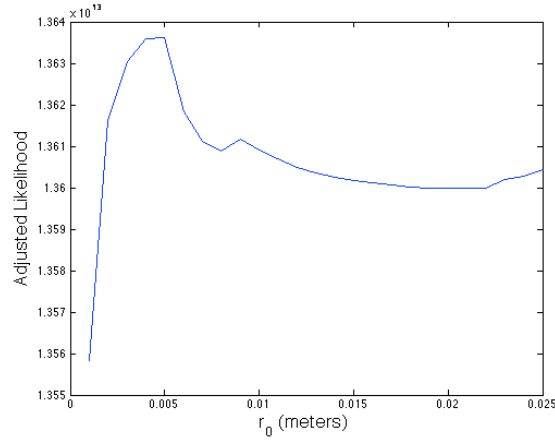
Figure 5.3: When only considering a single surface per detector for the single bar target, likelihood maximization produces a low estimate for the value of r_0.

136

5.4 Experimental

The simulation results discussed in the previous section demonstrated high levels of precision in the ability to estimate the multiple surface model in conjunction with the atmospheric seeing parameter. While the simulation was designed to closely replicate the results from an actual 3-D FLASH LADAR sensor, the complexity of the problem was reduced based on the target geometry. For the simulations, all targets were oriented normal to the sensor. Therefore, any pulse width expansion could be considered associated with the effects of diffraction. However, experimental conditions considered targets with various orientations. In this case, the received pulse width could vary due to the angle at which the outgoing pulse strikes the surface. The experimental results demonstrate that the algorithm is capable of separating the cause of pulse width variation.

5.4.1 Sensor Parameters.

The sensor used for this research was a modified ASC Portable 3-D FLASH LADAR Camera Kit$^{\text{TM}}$. The sensor used all of the standard components in this commercially available sensor; however, they were oriented into a different configuration for the USAF TPS as shown in Figure 2.4. The only significant differences between the specifications listed in Table 4.1 used for simulation and the sensor used for this experiment is with the optics. The optics parameters for the experiment are listed in Table 2.2. Given the sampling requirements in (4.40) and the optical specifications in Table 2.2, the maximum pixel size for proper sampling should be 2 μm×2 μm. However, the actual sensor detector had a much greater pixel size at 100 μm×100 μm.

Previous efforts with similar FLASH LADAR systems addressed the sampling requirement by significantly restricting the aperture diameter with a mask [16], [**?**].
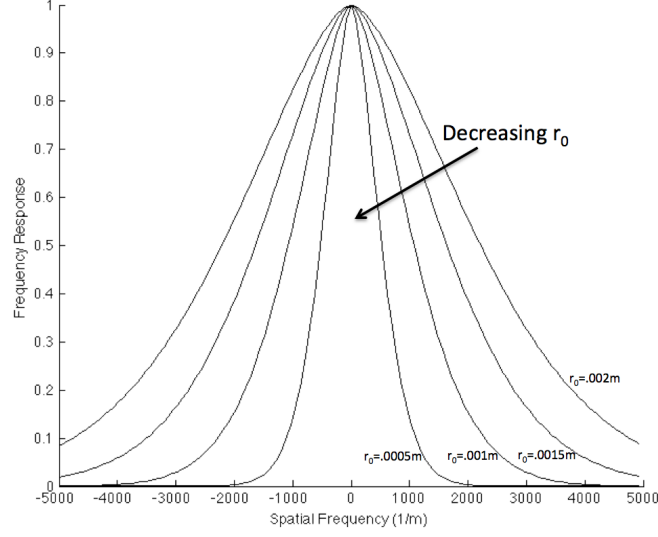
Figure 5.4: Frequency response as a function of spatial frequency for r_0 levels between 0.0005m and 0.002m.

For the size of the individual detectors in this sensor, the aperture would have needed to be approximately 2 mm for proper sampling with this technique. By restricting the aperture that far we would have greatly reduced the amount of light gathered thus negatively impacting the SNR. As an alternative, we chose to use a highly turbulent atmosphere to reduce the sampling requirement.

The atmosphere can essentially be treated as a low pass filter. The more turbulent the atmosphere becomes, the lower the sampling requirement will become as well. Considering the relationships in (2.9) and (2.10) we can show how the maximally observed spatial frequency is decreased as turbulence is increased or in other words as r_0 is decreased. Given the pixel pitch of the ASC sensor, the maximum spatial frequency satisfying Nyquist criteria is $5,000$ (1/m). Yet the optical specifications in Table 2.2 in conjunction with the relationship in (2.7) yield a sampling requirement of 305.7×10^3 (1/m). Therefore, the goal was to find an r_0 value that produced a cutoff frequency below $5,000$ (1/m). As shown in Figure 5.4, the frequency cutoff is reduced in conjunction with a reduction in r_0.

138

Based on the available sensor parameters, r_0 levels of approximately 0.0015m will yield proper sampling. Atmospheric seeing levels of this nature would be difficult to find naturally. Therefore, an extremely turbulent atmosphere was generated in front of the aperture using a 60,000 British Thermal Unit (BTU) heat source. This heat source consistently created r_0 levels between 0.001m and 0.002m. We have found that the MSID algorithm has some capability to deal with slightly undersampled data. However, the extent to which the data can be undersampled with this technique remains to be proven as a future research topic.

Placing this source of turbulence in front of the aperture had another benefit for this experiment. Since this sensor was originally designed to be placed in a pod on an aircraft, the lens was focused at infinity. With the ranges used for this experiment, the lens being focused at infinity resulted in a blurring of the images. The focus error OTF is similar to the atmospheric OTF at lower frequencies [22]. However, there are additional high frequency components in the focus error OTF. By imaging through the turbulent atmosphere, the added high frequency components were filtered out. The resultant OTF was measured to be very close to the theoretical short exposure OTF as shown in the following results.

5.4.2 Experimental Target Profiles.

The images collected for this research consist of two separate target configurations. Figure 5.5 displays the first configuration and its associated range profile. This configuration was designed such that ideally only the edge pixels where the two sheets overlap would have multiple surfaces. The second target configuration shown in Figure 5.6 is similar to the obscured target simulated in Chapter IV. With this target configuration the front sheet of plywood had the center section removed. An aluminum screen was then placed over this opening to allow a portion of the light

to pass through and a portion to be reflected. A second sheet of plywood was then placed behind the first sheet to provide a second return.
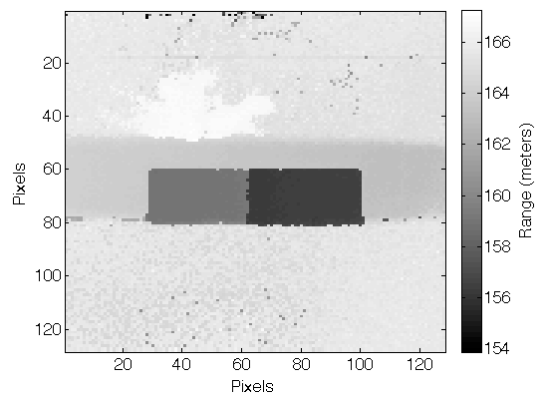
For target configuration 1, the two sheets of plywood were separated in range by approximately 2.6 m. The sheets were each oriented perpendicular from the sensor. Additionally, the sheets were positioned such that there would be some overlap at the center. Given the 3° FOV for the sensor and the range to the target, each pixel will correspond with a spatial area of approximately 6.5×6.5 cm^2. Therefore, we would expect only the column of pixels in the detector array corresponding with the overlap to have more than one surface in its FOV in an ideal environment. However, the following results show that this is not the case.

For target configuration 2, the two sheets of plywood were separated in range by approximately 3.4m. The sheet in the foreground had an opening in the center that was covered with an aluminum mesh screen. A second sheet of plywood was oriented behind and parallel to the first sheet. This configuration allows us to demonstrate the ability to detect an object through an obscuration. Given the range to this target and the 3° FOV of the sensor, each image pixel will correspond with an area of approximately 6×6 cm^2.
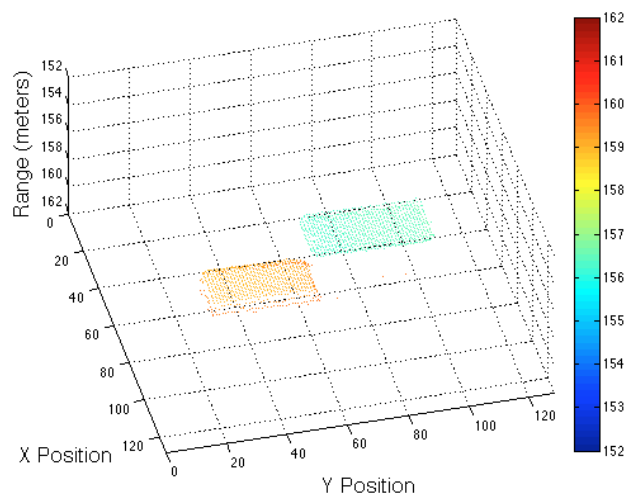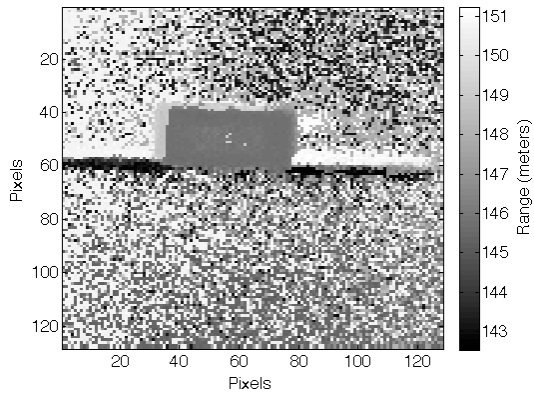
(a) Target Configuration 1

(b) Range Profile

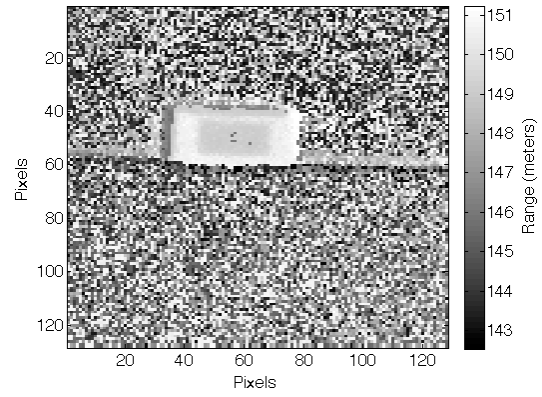(c) 3-D View of Target Configuration 1

Figure 5.5: **(a) Plywood in foreground at approximately 156.4m overlaps a second sheet of plywood placed at approximately 159m. (b) Range profile for target configuration 1. (c) 3-D representation of target configuration.**
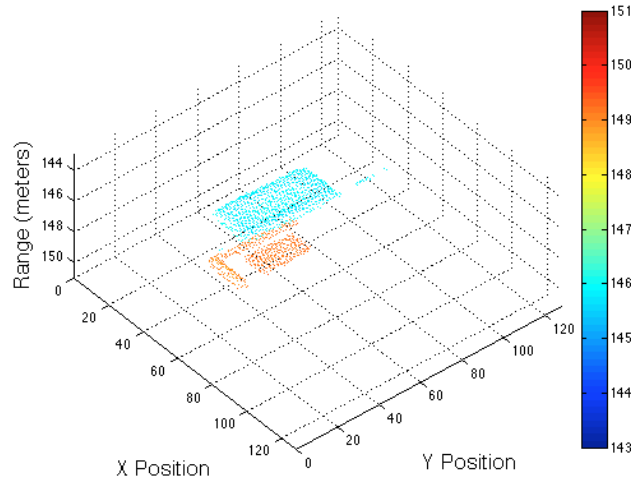
(a) Target Configuration 2

(b) Range to Surface 1

(c) Range to Surface 2

(d) 3-D View of Target Configuration 2

Figure 5.6: **(a) Plywood in foreground at approximately 145.8m contains a mesh screen in the center to allow ranging to the second sheet of plywood placed at approximately 149.2m. (b) Range to the most dominant surface in each pixel. (c) Range to second most dominant surface in each pixel. (d) 3-D representation of target configuration.**
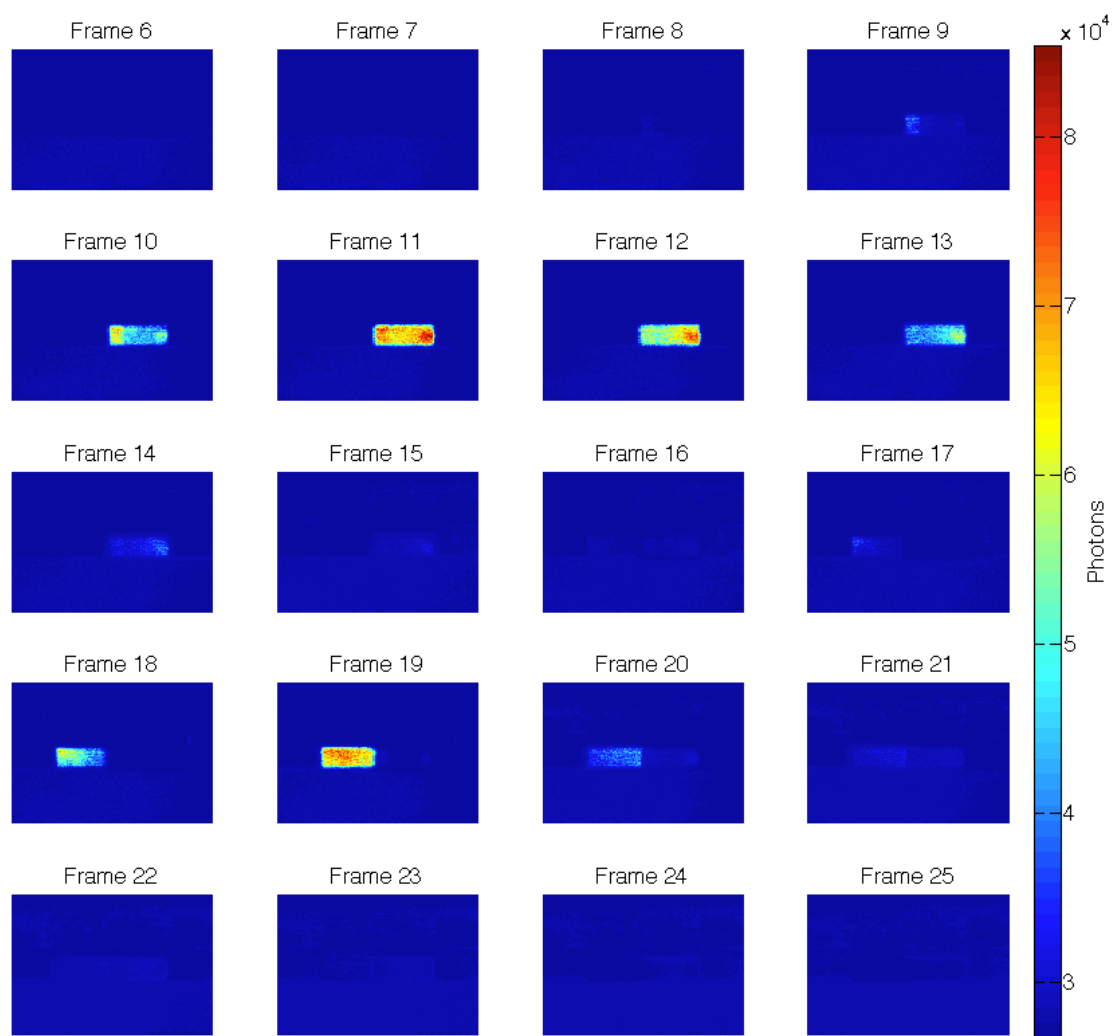
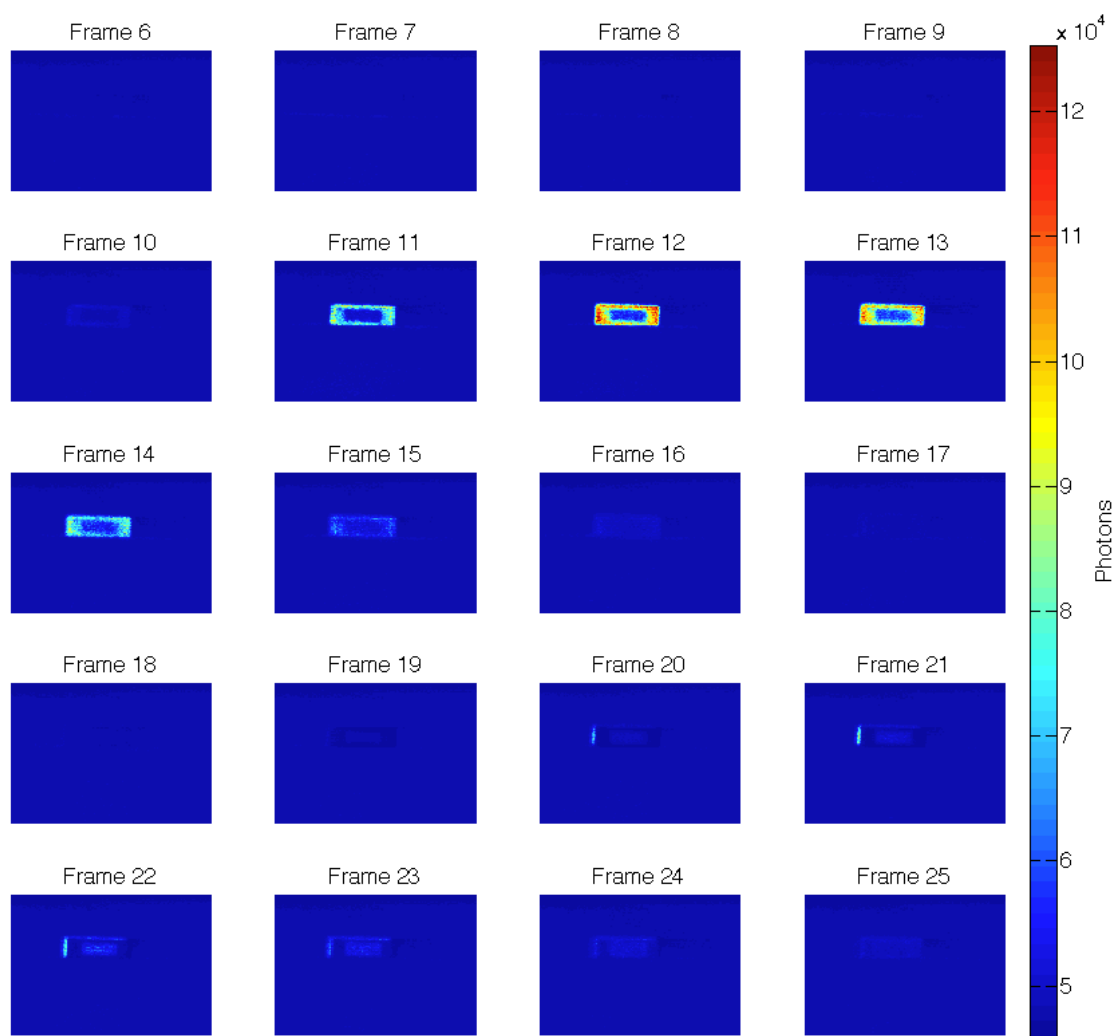**Figure 5.7: Individual 2-D frames for target configuration #1.**

Figure 5.8: Individual 2-D frames for target configuration #2.

### 5.4.3 Atmospheric Seeing - Truth Measurement Technique.

Both configurations were designed such that the true level of r_0 could be measured and compared with the estimates obtained using the MSID algorithm. The true seeing parameter is measured using the technique identified in Section 2.5. To implement this measurement technique, we can consider a range slice that only has one sheet of plywood in view. From this 2-D slice, we can calculate the step response by measuring the change from background to illuminated surface. For example, when only considering the intensity image corresponding with a range of 159m in the first target configuration, we get the 2-D image and measured frequency response as shown in Figure 5.9. Candidate OTFs across a suitable range of r_0 values can then be compared against this measured OTF to find the one that produces the MMSE. Notice that the measured frequency response contains high frequency components that are absent from the theoretical candidate OTFs. This is likely due to the noise present in the measured step response.
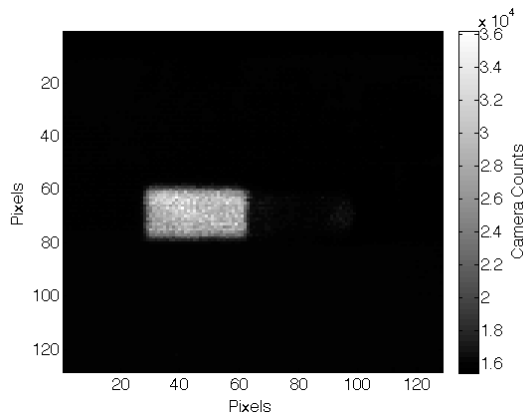
(a) Measured Step Target
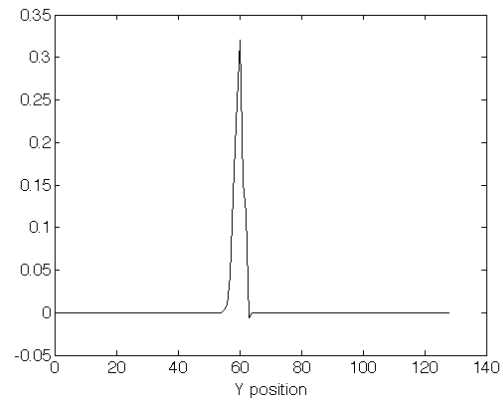
(b) Impulse Response
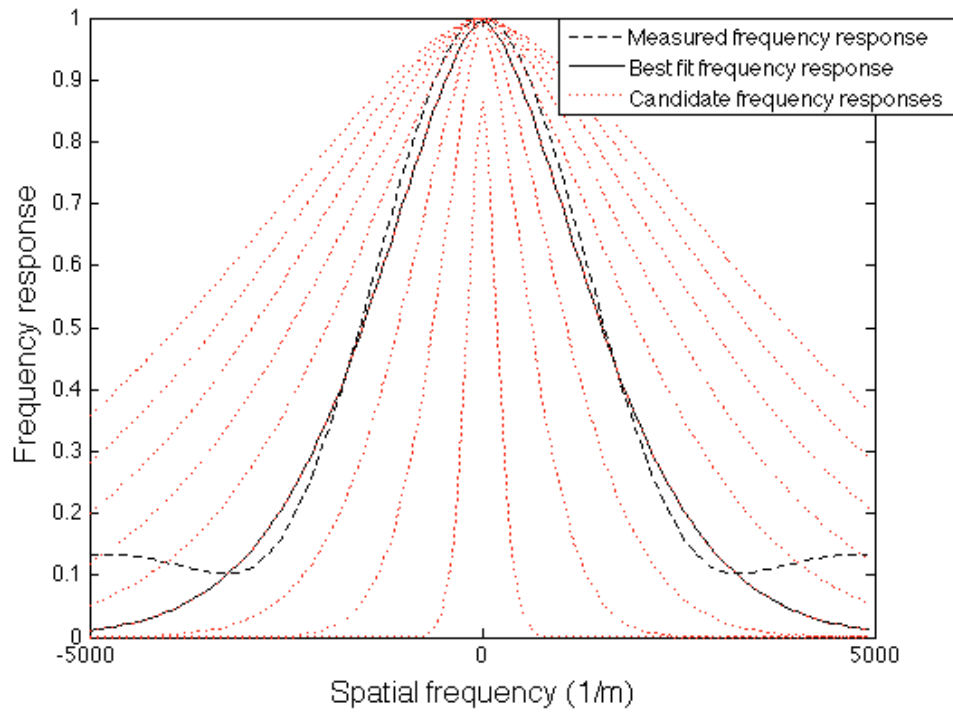
(c) Measured Frequency Response

Figure 5.9: **(a) Step target obtained by only considering the image intensity at a range of 159m. (b) Impulse response computed by first finding the step response or vertical change in intensity and then taking the first derivative of the step response. (c) Measured frequency response with an overlay of the best fit short exposure OTF (r_0=0.0012m), and a range of candidate OTFs.**

146

5.4.4 Experimental Results.

Using the previously mentioned target configurations, we now execute the MSID algorithm for a range of r_0 values. The search window for r_0 will consist of levels from 0.0001m to 0.01m with an increment of 0.0001m. One of the key advantages with this algorithm is that execution of the MSID algorithm for each level of r_0 is independent. This allows for easy parallelization or efficient search patterns such as the pattern described in Figure 3.4. Using the estimated parameters, we can compute the adjusted likelihood according to (5.5). As an example, Figure 5.10 shows the adjusted likelihood for each level of r_0 within this search window for Trial #1.

(a) Adjusted Likelihood vs r_0 (b) Zoom View of Adjusted Likelihood
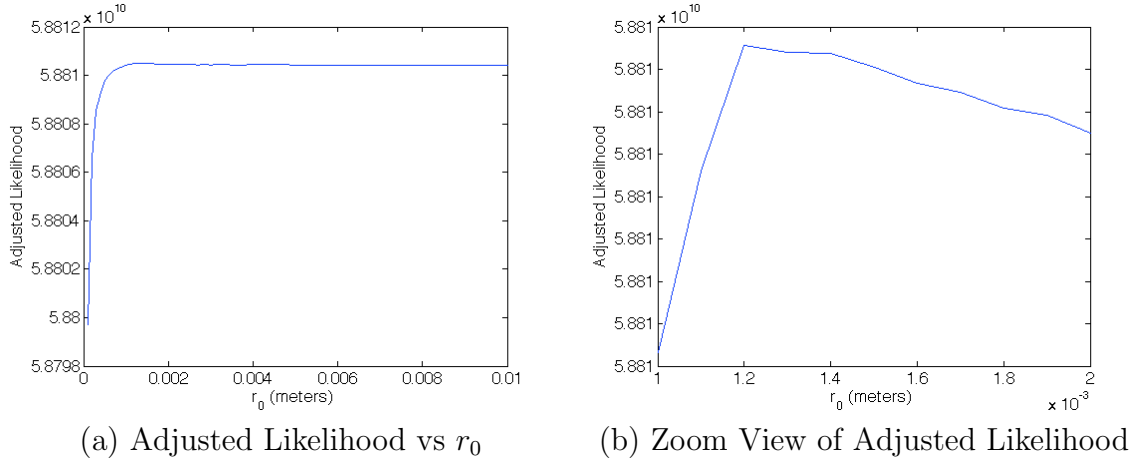
Figure 5.10: (a) **Adjusted likelihood for a range of r_0 values from 0.0001m to 0.01m.** (b) **Maximization of likelihood occurs at 0.0012m.**

Figure 5.10 shows that maximization of the adjusted likelihood occurs at $r_0 = 0.0012$m, which was what was expected based on the measured level of r_0. Of the four experiments conducted, each were accurate to within 0.0002 meters as shown in Table 5.1. More importantly, the results of the experiments were consistent with the results from simulations where we had significantly more control over the target geometry, simulated turbulence and optical specifications. The spatial and temporal blurring for target configuration #2 had less of an impact than what was observed

147

Table 5.1: Comparison of Measured and Estimated r_0 Values.

Target Profile #1 r_0 Values (meters)				
Trial	Measured	MSID - Estimated	CoV - Estimated	
			Frame 11	Frame 19
1	0.0012	0.0012	0.0012	0.0013
2	0.0013	0.0014	0.0013	0.0013
Target Profile #2 r_0 Values (meters)				
Trial	Measured	MSID - Estimated	CoV - Estimated	
			Frame 12	Frame 22
3	0.0019	0.0018	0.0017	0.0018
4	0.0019	0.0017	0.0016	0.0017

for target configuration #1 as indicated by the levels of r_0 shown in Table 5.1. The experiments for target configuration #1 were conducted on 6 February 2012 when the ambient air temperature was below 40°F. The experiments for target configuration #2 were conducted on 3 October 2012 when the ambient air temperature was above 70°F. Given the lower temperature difference between the ambient air and the output of the $60,000$ BTU heat source, we expect the values of r_0 to be higher when the outside air is warmer as indicated. The next section will visually show the improvement in estimation capability using the MSID algorithm.

The results from the CoV method detailed in Chapter III are also listed in Table 5.1. Based on the results from simulation, shown in Section 3.4, we hand selected two frames from each 3-D image to perform the CoV method. Recalling that simulations show improved accuracy in higher contrast images, we chose frames 11 and 19 for target configuration #1, and frames 12 and 22 for target configuration #2. The results from the CoV method are similar to the estimates obtained through maximization of likelihood in conjunction with the MSID algorithm. This highlights that the CoV technique is a viable backup in cases where abnormalities in pulse shape may make maximization of likelihood in conjunction with the MSID algorithm unreliable.

5.4.5 Observed Performance Enhancement.

The overall goal of this technique is to simultaneously find the pulse parameters and value of r_0 that maximizes likelihood as demonstrated in Section 5.3. For comparison purposes we will also consider an EM solution that does not account for the effects of diffraction and only seeks to fit the best possible Gaussian mixture to the received data. Range RMSE measurements are not possible since we do not have truth range information to each point in the scene. However, we can assess the algorithm's ability to accurately predict the correct number of surfaces for each point in the scene based on target geometry as well as the ability to accurately predict r_0.

The MSID algorithm relies on the CaR technique to identify the true number of surfaces per pixel [52]. The target configurations and the sensor range gate were set up such that a maximum of two returns should be visible in each detector. Therefore, the MSID algorithm will estimate a Gaussian mixture with two returns for each pixel. In cases where a pixel has fewer returns than the pre-defined cap, the algorithm should ideally drive those amplitudes towards zero. As previously demonstrated, once the algorithm's termination criteria is achieved, we then execute the full-waveform detection strategy to determine if the individual pulse amplitudes warrant a detection [58]. Given the target geometry in configuration #1, we would only expect the single column of pixels corresponding with the overlap of the two sheets of plywood to have multiple returns when the effects of diffraction are removed. For target configuration #2, we expect the center region of the plywood and the edge of the front sheet of plywood to have multiple returns.

Figure 5.11 shows that the overlap region between the two sheets of plywood is as many as four pixels wide. At a range of approximately 157 m, this would mean that the overlap region is up to 26 cm wide, providing a significant amount of ambiguity to the true overlap point. In Figure 5.12 each of the received pulses and pulse estimates
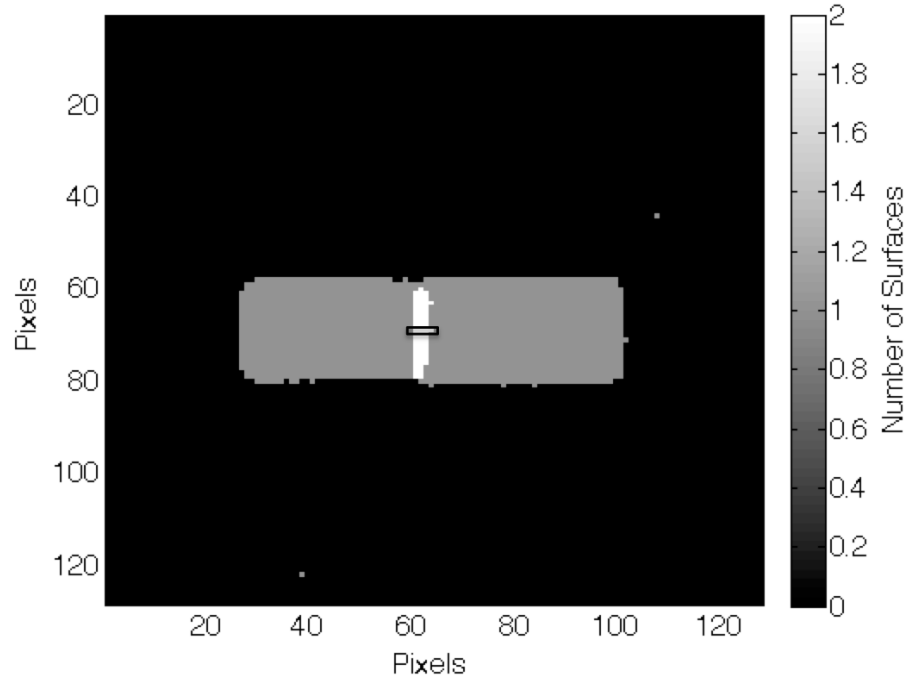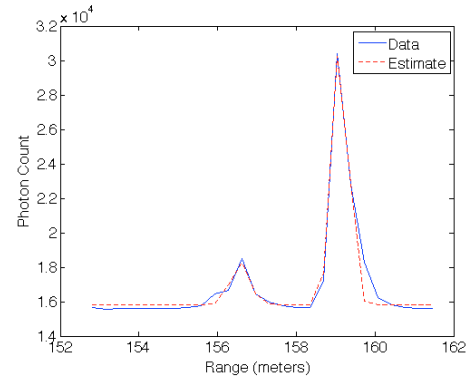
Figure 5.11: **Target Configuration #1 - Number of surfaces detected for each pixel without accounting for the effects of diffraction.**
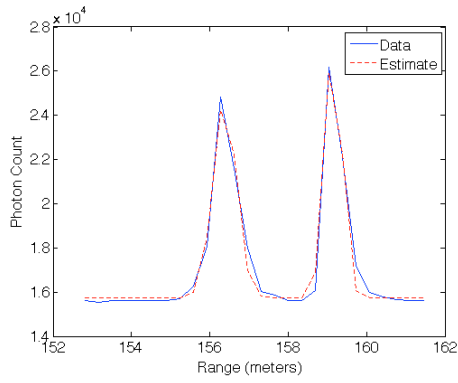
are compared for the highlighted region from Figure 5.11. With the exception of pixels (60,69) and (65,69), each of the received pulses have two returns corresponding with the surface prediction. However, based on target geometry, we would only expect one of the received pulses to contain multiple surface returns in the absence of diffraction effects.
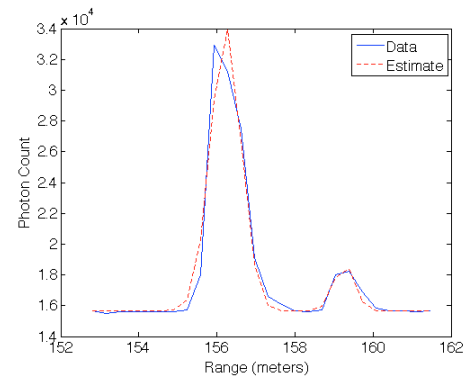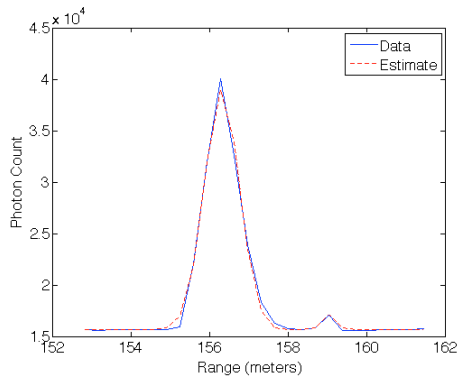
150
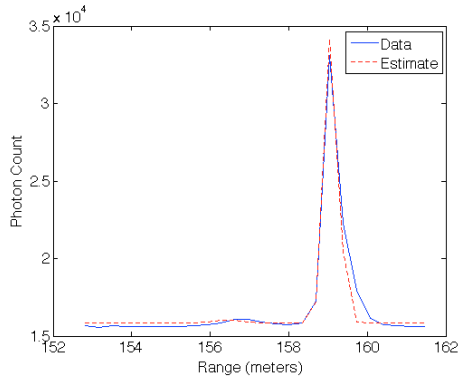
(a) Pixel (60,69)

(b) Pixel (61,69)

(c) Pixel (62,69)

(a) Pixel (63,69)

(b) Pixel (64,69)

(c) Pixel (65,69)

Figure 5.12: Individual pulse reconstructions compared with received pulses for the highlighted region from Figure 5.11 without accounting for the effects of diffraction.

By incorporating the effects of diffraction, we can more accurately estimate the number of surfaces per pixel. Figure 5.13 shows the number of surfaces that are detected per pixel when the value of r_0 which maximized the likelihood ($r_0 = 0.0012$m) is used. By accounting for the effects of diffraction, the region of overlap is reduced to a single column in most places. In Figure 5.14 each of the received pulses and

Figure 5.13: **Target Configuration #1 - Number of surfaces detected for each pixel when accounting for the effects of diffraction.**

pulse estimates are compared for the highlighted region from Figure 5.13. Through the use of the MSID algorithm, the amplitude for the second surface is driven below the detection threshold for all but pixel (62,69).
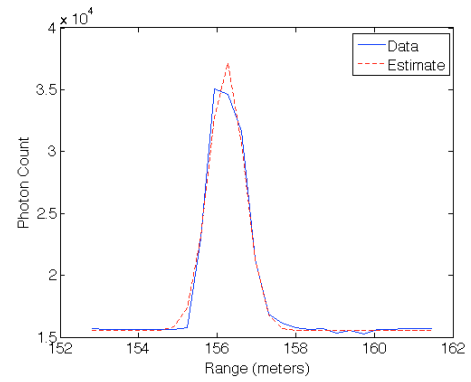
(a) Pixel (60,69)
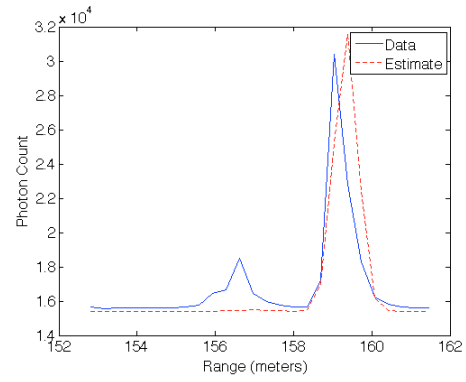
(b) Pixel (61,69)
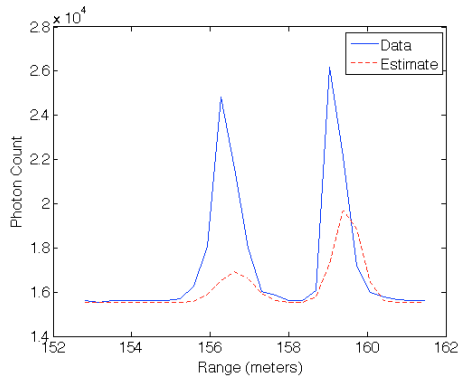
(c) Pixel (62,69)
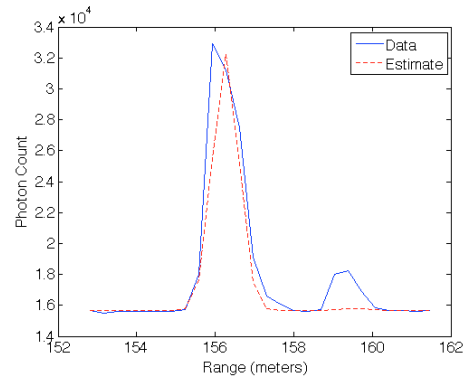
(a) Pixel (63,69)
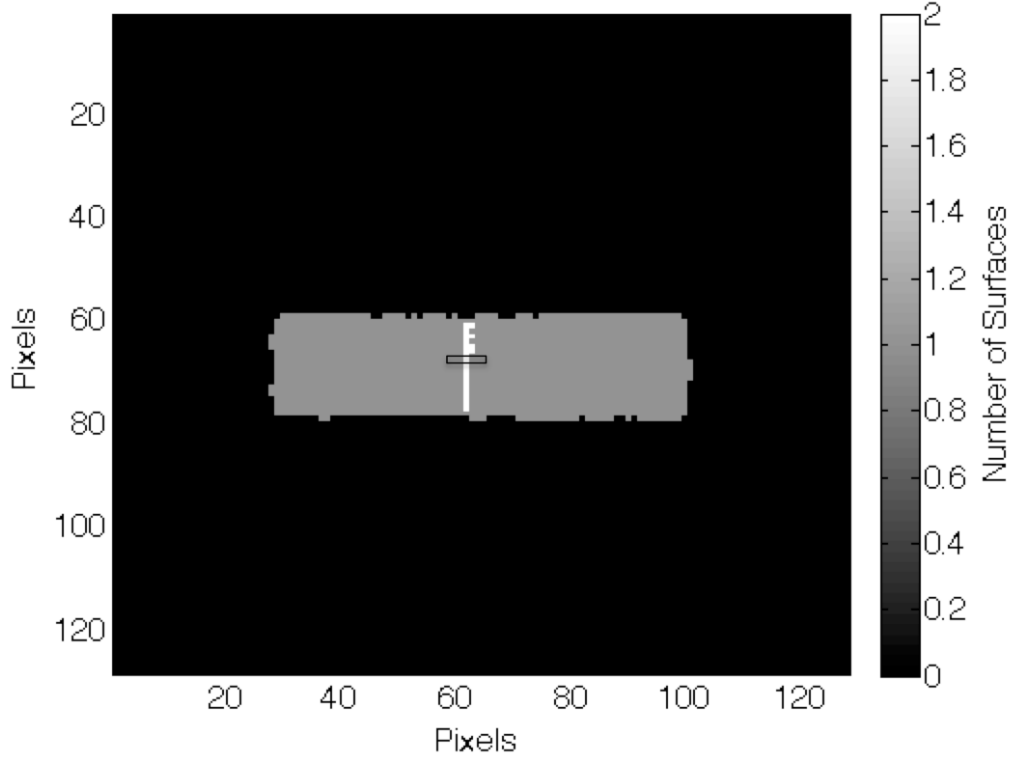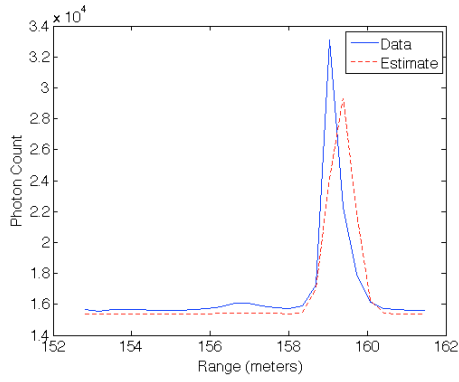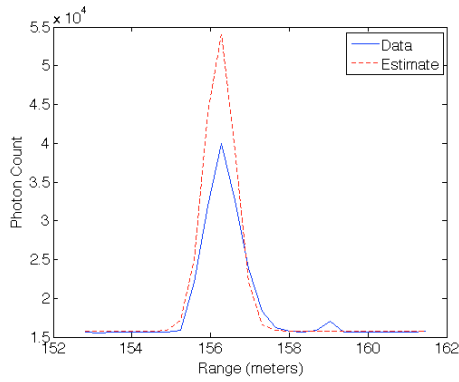

(b) Pixel (64,69)
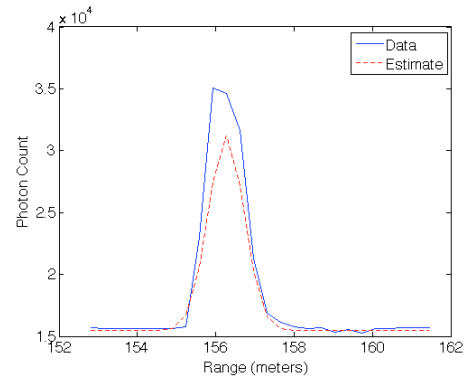
(c) Pixel (65,69)

Figure 5.14: Individual pulse reconstructions compared with received pulses for the highlighted region from Figure 5.13 when accounting for the effects of diffraction.

An additional metric for comparison is based on the known target height. The sheet of plywood on the right is 1.22 m tall, and the range to this sheet of plywood is approximately 157 m. Given this geometry and the sensor parameters we would expect the sheet to only require a vertical range of 19 - 20 pixels in the detector FOV. However, when the straight Gaussian mixture model is applied to the received data, the target is measured at 22 - 23 pixels tall. Once the MSID algorithm is applied, the target only requires a vertical range of 19 - 21 pixels in the detector FOV. This reduction in blurring around the edges of the target can be observed by looking at the difference between Figures 5.11 and 5.13 as shown in Figure 5.15.
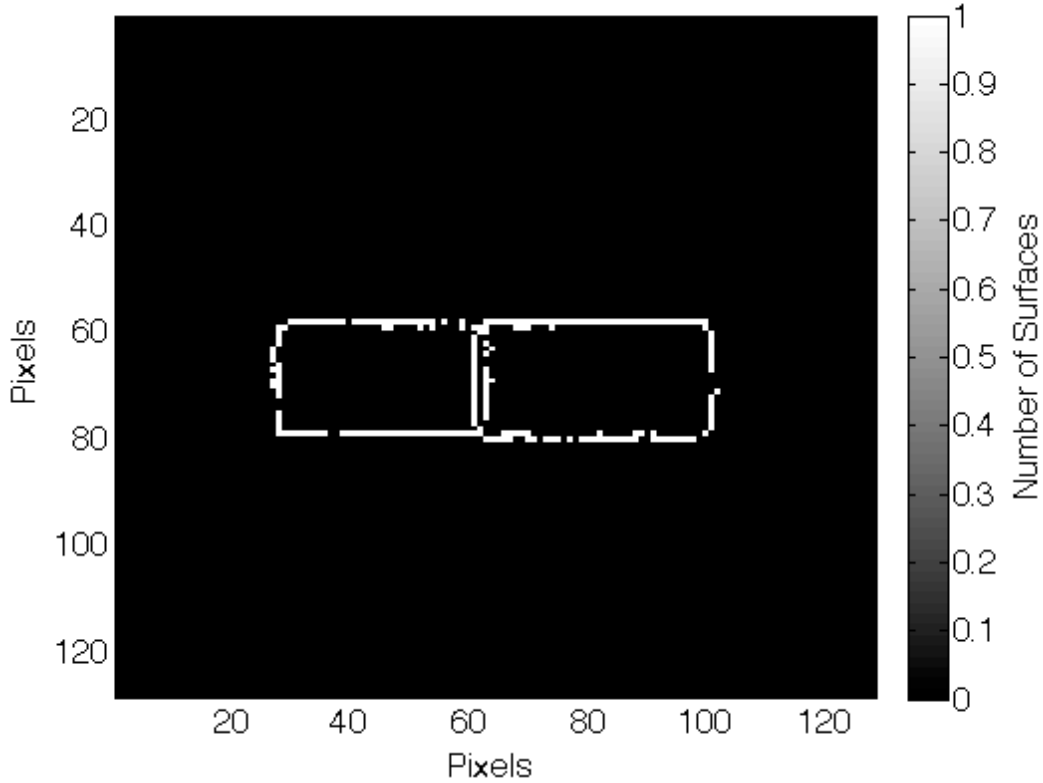
**Figure 5.15: Target Configuration #1 - Difference in the number of surfaces detected for each pixel when not accounting for the effects of diffraction minus the results from the MSID algorithm.**

We now demonstrate similar results for target configuration #2. When a Gaussian mixture model is applied to the received data without accounting for the effects of

154

diffraction, the CaR technique reveals multiple surfaces in many pixels where only a single surface should exist. In an ideal environment, a single row / column of pixels should have multiple surfaces visible corresponding with the top / left sides of the target respectively. Additionally, the center section of the target should also have multiple surfaces visible. However, when we fail to account for the effects of diffraction, we again see that the spatial and temporal blurring around the edges of the target results in numerous false detections as shown in Figure 5.16.
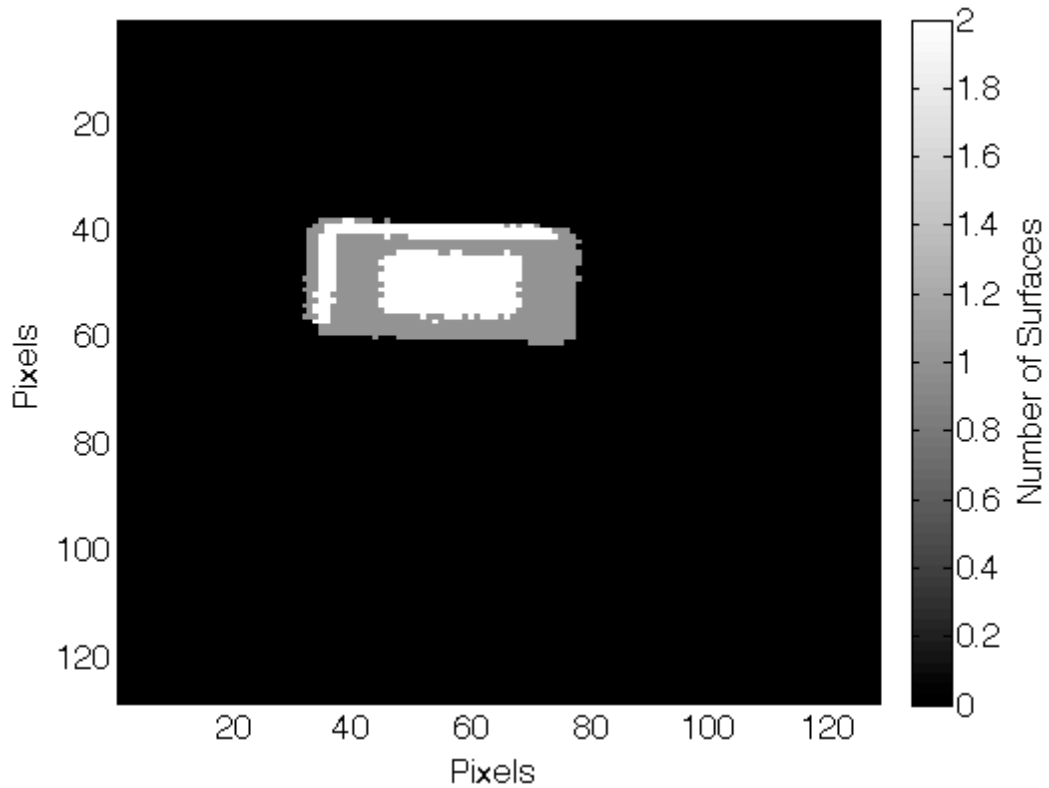
Figure 5.16:   Target Configuration #2 - Number of surfaces detected for each pixel without accounting for the effects of diffraction.

By incorporating the effects of diffraction, the estimated number of surfaces per pixel can again be brought more in line with the expectation based on target geometry. Figure 5.17 shows the number of surfaces that are detected per pixel when the value of r_0 which maximized likelihood ($r_0 = 0.0019$m) is used. By accounting for the

155

effects of diffraction, the overlap regions on the left and top of the target are reduced in most places. Additionally, there is a reduction in blurring around the edges of the
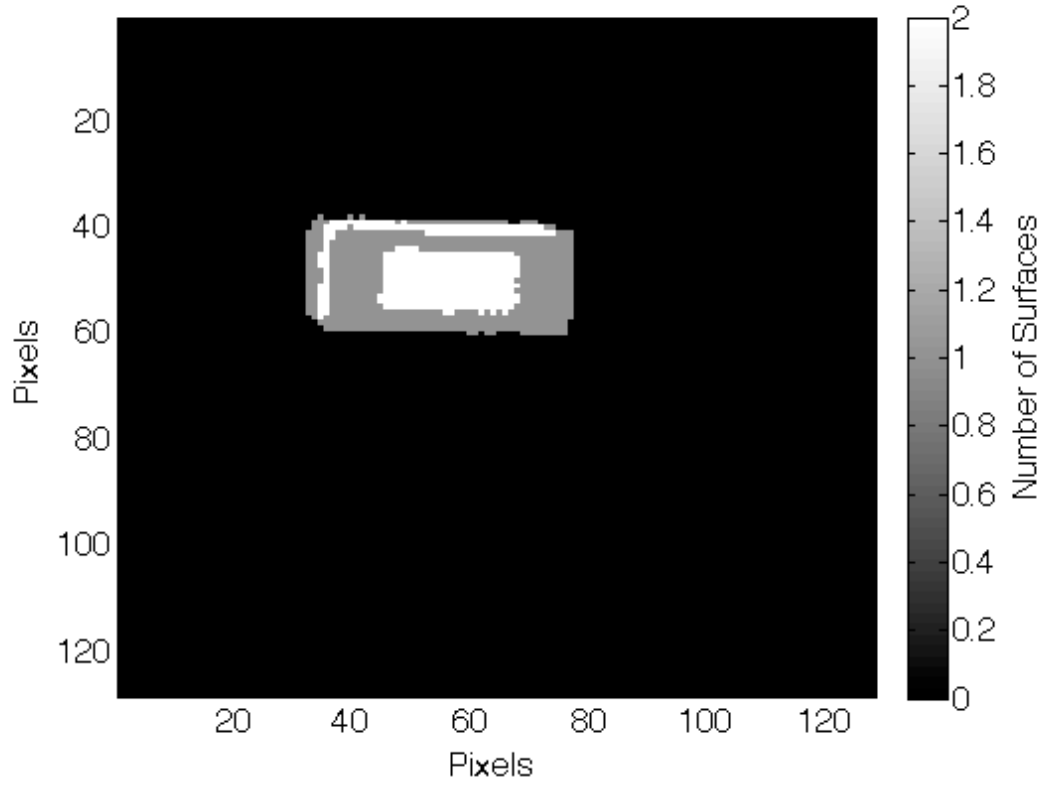
Figure 5.17: **Target Configuration #2 - Number of surfaces detected for each pixel when accounting for the effects of diffraction.**

target as observed by comparing the difference in Figures 5.16 and 5.17 as shown in Figure 5.18.

156
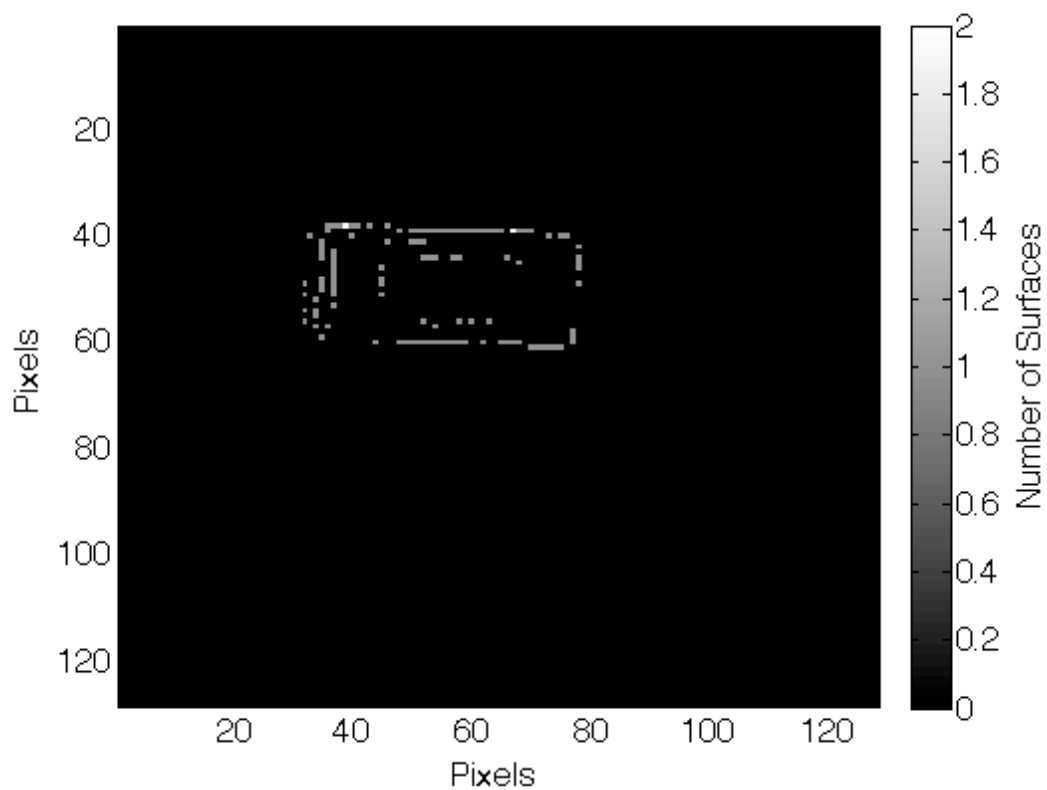
Figure 5.18: Target Configuration #2 - Difference in the number of surfaces detected for each pixel when not accounting for the effects of diffraction minus the results from the MSID algorithm.

5.4.6   Joint Estimation Requirement.

The previous results demonstrated that a likelihood maximization approach to the parameterized blind deconvolution problem is possible with properly sampled 3-D images. As a final consideration, the requirement to fully account for all surfaces visible in the received data will be demonstrated. Through simulation, we found that the ability to accurately estimate the value of r_0 was significantly degraded by failing to account for the temporal and spatial interaction of all surfaces. When only accounting for a single surface per detector, we found that likelihood was maximized for a low estimate of r_0. When working with experimentally collected data, the ability to accurately estimate r_0 was again degraded. For both target configurations, the maximization of likelihood with respect to r_0 occurred at a value higher than previously estimated or measured as demonstrated in Figures 5.19 and 5.20.

(a) Adjusted Likelihood vs r_0 (b) Zoom View of Adjusted Likelihood
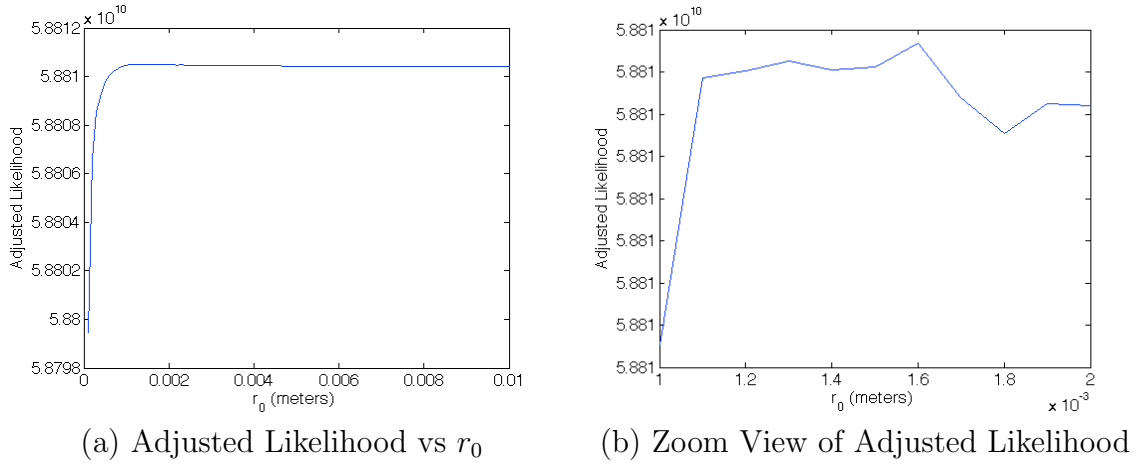
Figure 5.19:   Target configuration #1 single surface estimation. (a) Adjusted likelihood for a range of r_0 values from 0.0001m to 0.01m. (b) Maximization of likelihood occurs at 0.0016m where the measured value was 0.0012m.

5.5   Chapter Summary

Enhancements in the capability gained through 3-D imaging are significant. Current sensors may have limited military utility due to the maturity of the technology.

(a) Adjusted Likelihood vs r_0 (b) Zoom View of Adjusted Likelihood
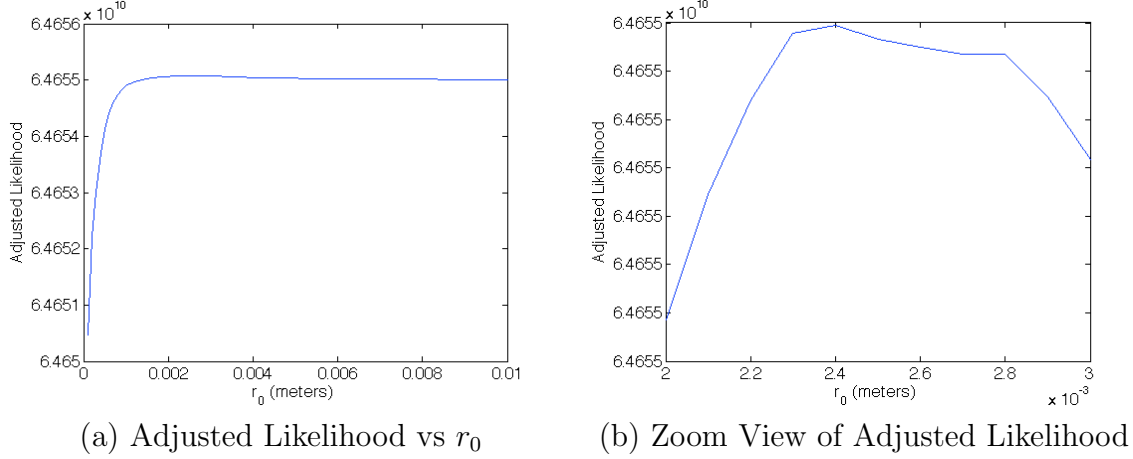
Figure 5.20: **Target configuration #2 single surface estimation. (a) Adjusted likelihood for a range of r_0 values from 0.0001m to 0.01m. (b) Maximization of likelihood occurs at 0.0024m where the measured value was 0.0018m.**

However, it is expected that this technology may eventually fully coexist with passive type sensors due to a myriad of associated advantages. The algorithm developed for this research demonstrates that parameterized blind deconvolution is an over-determined problem for range diverse scenes, with a direct solution that maximizes likelihood. When coupled with the MSID algorithm, we can simultaneously discriminate the range to multiple surfaces per pixel, while also improving spatial resolution and temporal accuracy. This algorithm will further enhance the ability to detect targets behind an obscuration. Improvements such as these are critical for the migration of this technology to the next generation of imaging sensors.

This algorithm is novel in its approach to the parameterized blind deconvolution problem in that it uses the added information available with 3-D imaging. Given the following conditions:

- Exposure time is short enough that the atmosphere can be considered static

- Range diversity exists in the targeted scene

- Relationship in (5.3) is satisfied

the problem appears to have a direct solution. All work to this point has been conducted with the assumption that the images are properly sampled. This requirement was a driving factor for using such high levels of turbulence in the experiments. It is possible that similar techniques could be used for images that are not properly sampled or slightly under sampled and this possibility poses an interesting topic for future experimentation. Finally, while this technique was only demonstrated with the short exposure OTF parameterized by r_0, it is likely that the technique would work for other blurring functions that can be reduced to functions of a few parameters such as focus error.

VI. Conclusion

Contributions from this research enhance the ability to accurately extract pulse information with a three dimensional FLASH LAser Detection and Ranging (3-D FLASH LADAR) sensor where multiple returns per image pixel are possible. The algorithms and techniques developed significantly enhance ranging accuracy and target modeling where the received image is degraded by the effects of imaging through a turbid medium. Additionally, the algorithms were designed with computational efficiency in mind such that they could be employed in a tactical environment where processing time and power may be limited.

Active illumination sensors such as 3-D FLASH LADAR have recently garnered a significant amount of interest for defense and civilian applications. Due to the employment of active flood illumination, 3-D FLASH LADAR sensors can gather ranging information for every point within a targeted scene nearly simultaneously. Furthermore, depending on the detection methodology employed, the possibility of imaging through obscurations becomes a reality. Potential benefits from this technology are currently constrained by manufacturing challenges as well as the difficulty in extracting the parameters of interest out of the received data. This research focuses on the latter constraint of parameter extraction and enhancement. As an aside, the research concludes that unique solutions exist to some problems that were previously deemed mathematically ill-posed for traditional optical sensors.

This chapter provides a summary of each of the primary chapters in this dissertation, reviews the key contributions to this research discipline and offers numerous ideas for future research that could yield even further enhancement.

6.1   Chapter Summaries

Chapter II reviewed key theoretical concepts that were employed throughout this research effort. The focus of this review was on 3-D FLASH LADAR operation, statistical modeling of noise in collected images, estimation techniques with iterative algorithms and the effects of atmospheric turbulence on collected imagery. An overview of the sensors employed for collection of experimental data was provided. Finally, previous research on blind deconvolution, multi-surface ranging and 3-D FLASH LADAR image enhancement was summarized and compared with this work.

Chapter III revisited parameterized blind deconvolution techniques that were developed by MacDonald and MacManus for two dimensional (2-D) imagery [41], [45]. MacDonald employed a noise based stopping criteria in conjunction with an *a priori* assumption for the distribution of the atmospheric seeing parameter, r_0. This allowed him to simultaneously find a maximum likelihood solution for the parameterized Optical Transfer Function (OTF) and the deblurred image. MacManus later demonstrated that the *a priori* assumption was not required. Rather, employment of the noise based stopping criteria was sufficient to solve the parameterized blind deconvolution problem. Numerous experiments with fully illuminated and partially illuminated scenes were conducted to validate the results obtained through simulation. Additionally, the algorithm was employed against scenes illuminated with both incoherent and partially coherent light. Finally, this technique was applied to simulated 3-D FLASH LADAR images to demonstrate its effectiveness.

Chapter IV details the development of the novel multiple surface ranging algorithm that accounts for the effects of diffraction. This algorithm takes the somewhat common approach of applying a Gaussian mixture model to the received 3-D FLASH LADAR data. However, the pulse model is expanded to simultaneously incorporate the effects of diffraction on the received pulse. Solutions for pulse amplitude, range

162

and width are developed for each return in the received data. Additionally a solution for the detector bias is developed for situations where it is impractical to measure separately. A novel approach to determining the optimal mixture or number of returns per pixel is presented. Finally, a constraint on the pulse amplitude estimates is derived to prevent improper convergence of the algorithm. Simulated 3-D FLASH LADAR data was used to compare the performance of the various ranging techniques. Traditional Gaussian mixture modeling without considering the effects of diffraction, frame-by-frame 2-D deconvolution techniques and the constrained / non-constrained multi-surface ranging algorithms were each employed on the simulated data.

Chapter V provides the capstone for the research effort. In this chapter the set of equations are developed that demonstrate that parameterized blind deconvolution is often an overdetermined problem when working with range diverse 3-D FLASH LADAR data. A maximum likelihood solution is employed to determine the optimal level of atmospheric seeing to deblur the collected images. The technique is first employed on simulated data where the target geometry, orientation and atmospheric seeing are precisely controlled. An actual 3-D FLASH LADAR sensor is then employed to validate the results from simulation.

6.2 Summary of Key Contributions

6.2.1 Multi-surface Ranging Algorithm.

Perhaps the most significant contribution of this work was the derivation of a multi-surface ranging algorithm that incorporates the effects of diffraction. This algorithm simultaneously estimates pulse parameters from the received data for multiple surfaces per image pixel. Through a survey of relevant literature, no other multi-surface ranging algorithm that removes the effects of diffraction could be identified. Depending on the application of the 3-D FLASH LADAR sensor, the effects

163

of diffraction can have significant negative impact on the received images.

Multiple enhancements were observed in the processed images with this algorithm. First, the accuracy of this multi-surface estimation is improved through the reduction of diffraction effects caused by imaging through a turbulent atmosphere. With 2-D images, diffraction effects manifest as a spatial blur. However, in 3-D imaging, diffraction effects simultaneously manifest as a spatial and temporal blur. The temporal blurring can cause the realization of false surface returns in the received data. The algorithm developed for this research significantly reduces temporal blurring. Traditional multi-surface ranging algorithms would treat the surfaces that arise from temporal blurring as additional returns, while the MSID algorithm attempts to remove them. Second, the employment strategy for the algorithm discussed within this dissertation addresses common challenges associated with Expectation Maximization (EM) for Gaussian mixture modeling such as parameter initialization and more importantly determining the number of components that exist in the mixture. This research employs a Cap and Refine (CaR) strategy, where the presence of false returns are initially accounted for but then eliminated through iteration of the EM algorithm. Third, the algorithm also improves the spatial representation of the image that is commonly associated with 2-D blind deconvolution techniques.

6.2.2 Amplitude Constraint to Prevent Early Convergence of Variance.

Convergence of variance is a useful stopping criteria for algorithms such as the one developed in this dissertation. However, through the course of testing this algorithm, it was uncovered that the algorithm commonly terminates before the optimal solution is found. This is due to the simultaneous estimation of pulse amplitude and bias parameters. A constraint was derived through the use of a Lagrange multiplier

164

that significantly reduced the chances for improper convergence. By applying a constraint on the amplitude that is based on the deblurred 2-D image representation, we minimize the chances of hitting the stopping criteria for the iterative algorithm before the optimal solution is found. Of notable importance, this amplitude constraint has application even in cases where the image is not impacted by the effects of diffraction.

6.2.3 Maximum Likelihood Solution to Parameterized Blind Deconvolution Problem.

Through consideration of range diversity available with 3-D FLASH LADAR, the problem of parameterized blind deconvolution often becomes over-determined. Using the multi-surface ranging algorithm, this research shows that likelihood is maximized for the correct value of atmospheric seeing. Due to the ill-posed nature of the problem with 2-D images, similar attempts at a solution require additional assumptions and/or *a priori* information to allow for a likelihood maximization approach. Of additional importance, the capability to produce a solution to this previously ill-posed problem by taking advantage of range diversity highlights potential opportunities for other challenging problems commonly encountered with 2-D imaging.

6.2.4 Employment of CoV Technique on 3-D FLASH LADAR Images.

The results presented in this dissertation demonstrate that the Convergence of Variance (CoV) technique originally developed by MacManus has application in determining the parameterized blurring function in 3-D FLASH LADAR imaging. However, this research also points to the relationship between accuracy of the r_0 estimates and the Signal to Noise Ratio (SNR) in the collected images. Due to the manner in which 3-D FLASH LADAR images are recorded, the user may be required to derive an optimal method for selection of a 2-D frame on which the CoV technique will be

performed.

6.3 Future Research

During the execution of this research program, numerous topics were uncovered which may yield further enhancement in the field of imaging with 3-D FLASH LADAR sensors.

6.3.1 2-D and 3-D Data Fusion.

The algorithms developed in this research effort and the results they produced relied on properly sampled imaging data. However, the current state of sensor technology presents numerous challenges to the collection of properly sampled data. This research effort obtained properly sampled data by using an extremely turbulent atmosphere to act as a low-pass filter. Alternatively, given the current state of the technology, properly sampled data could only be achieved with optical configurations with high focal ratios. Through the fusion of properly sampled 2-D imagery and under sampled 3-D imagery, it may be possible to reduce the sampling requirement for 3-D sensors while yielding similar performance gains summarized in this work. We found that the multi-surface ranging algorithm had some capability to deal with slightly undersampled data. However, the extent to which the data can be undersampled with this technique also remains to be proven as a future research topic.

6.3.2 Applicability to Other Parameterized Blurring Functions.

For purposes of this research, we substituted the average short exposure transfer function, $\bar{H}_{SE}$, as our model for the atmospheric Optical Transfer Function (OTF), H_{atm}. However, the techniques developed should be directly applicable to other cases where the blurring function can be reduced to relatively few unknowns. One inter-

esting topic would be to extend this research to remove the effects of focus blur. This particular extension may be useful for deblurring 3-D FLASH LADAR images with long range gates at relatively short ranges. Additionally, a potential extension for this future research would be the relationship between the seeing parameter and focus interaction for varying levels of focus error and atmospheric turbulence. In Chapter III we noticed an interaction between focus and atmospheric blur which resulted in low estimates for atmospheric seeing. It would be interesting to see if the two could be separated.

6.3.3 Direct Solution for Parameterized OTF.

This research employed a maximization of likelihood approach to find the optimal parameterized OTF. However, it may be possible to directly solve for the parameterized OTF in conjunction with the deblurred pulse model. An attempt was made to approximate the Point Spread Function (PSF) as a Gaussian and directly solve for the width parameter in an iterative fashion. However, this technique did not yield accurate results.

6.3.4 Alternative Stopping Criteria.

The iterative algorithms presented in this research rely on the CoV technique to establish the stopping criteria. However, due to the Gaussian approximation for the returned pulse, this technique may be problematic in non-uniform data. An exploration / comparison of other stopping criteria is warranted such as those presented by Arioli [3].

Bibliography

[1] "Imaging drives \$17 billion remote-sensing satellite market". *SPIE Professional*, 7(3):21, July 2012.

[2] Almeida, M. and M. Figueiredo. "New stopping criteria for iterative blind image deblurring based on residual whiteness measures". *Statistical Signal Processing Workshop (SSP), 2011 IEEE*, 337 –340. June 2011.

[3] Arioli, M., I. Duff, and D. Ruiz. "Stopping criteria for iterative solvers". *SIAM J. Matrix Anal. Appl.*, 13(1):138–144, January 1992. ISSN 0895-4798.

[4] Ayers, G. R. and J. C. Dainty. "Iterative blind deconvolution method and its applications". *Opt. Lett.*, 13(7):547–549, July 1988.

[5] Biggs, D. and M. Andrews. "Asymmetric iterative blind deconvolution of multi-frame images". *Advanced Signal Processing Algorithms, Architectures, and Implementations VIII*, volume 3641, 328–338. Oct 1998.

[6] Bretar, F., A. Chauve, C. Mallet, and B. Jutzi. "Managing full waveform LIDAR data: A challenging task for the forthcoming years". *International Archives of Photogrammetry, Remote Sensing and Spatial Information Sciences*, 37:415–420, 2008.

[7] Cain, S., R. Richmond, and E. Armstrong. "Flash light detection and ranging range accuracy limits for returns from single opaque surfaces via Cramer-Rao bounds". *Appl. Opt.*, 45(24):6154–6162, Aug 2006.

[8] Carasso, A. "APEX blind deconvolution of color Hubble space telescope imagery and other astronomical data". *Optical Engineering*, 45(10):107004, Oct 2006.

[9] Carasso, A., D. Bright, and A. Vladar. "APEX method and real-time blind deconvolution of scanning electron microscope imagery". *Optical Engineering*, 41(10):2499–2514, Oct 2002.

[10] Carvalho, L., L. Fonseca, E. Novo, and G. Boggione. "Comparison of image restoration methods applied to inland aquatic systems images aquired by HR CBERS 2B sensor". *Geoscience and Remote Sensing Symposium (IGARSS), 2010 IEEE International*, 523 –526. July 2010. ISSN 2153-6996.

[11] Chan, T. and C. Wong. "Total variation blind deconvolution". *IEEE Transactions on Image Processing*, 7(3):370 –375, Mar 1998. ISSN 1057-7149.

[12] Chantas, G., N. Galatsanos, R. Molina, and A. Katsaggelos. "Variational Bayesian Image Restoration With a Product of Spatially Weighted Total Variation Image Priors". *IEEE Transactions on Image Processing*, 19(2):351 –362, Feb 2010. ISSN 1057-7149.

[13] Chen, C. and R. Stettner. "Drogue tracking using 3D FLASH LIDAR for autonomous aerial refueling". volume 8037, 80370Q. SPIE, June 2011.

[14] Dempster, A., N. Laird, and D. Rubin. "Maximum Likelihood from Incomplete Data via the EM Algorithm". *Journal of the Royal Statistical Society, Series B*, 39(1):1–38, 1977.

[15] Dey, N., L. Blanc-Feraud, C. Zimmer, Z. Kam, J.-C. Olivo-Marin, and J. Zerubia. "A deconvolution method for confocal microscopy with total variation regularization". *IEEE International Symposium on Biomedical Imaging: Nano to Macro*, 1223 – 1226 Vol. 2. Apr 2004.

[16] Dolce, P. and S. Cain. "Three-dimensional LADAR range estimation using expectation maximization". *Journal of Applied Remote Sensing*, 5:053513, Mar 2011.

[17] Fish, D., A. Brinicombe, and E. Pike. "Blind Deconvolution by Means of the Richardson-Lucy Algorithm". *Journal of the Optical Society of America*, 12:5865, Jan 1995.

[18] Gelbart, A., C. Weber, S. Bybee-Driscoll, J. Freeman, G. Fetzer, T. Seales, K. McCarley, and J. Wright. "FLASH LIDAR data collections in terrestrial and ocean environments". volume 5086, 27–38. SPIE, Aug 2003.

[19] Giryes, R., M. Elad, and Y. Eldar. "The Projected GSURE for Automatic Parameter Tuning in Iterative Shrinkage Methods". *CoRR*, abs/1003.3985, 2010.

[20] Gonzalez, R. and R. Woods. *Digital Image Processing*, 354. Pearson/Prentice Hall, 2007.

[21] Goodman, J. *Statistical Optics*. Wiley Classics Library. John Wiley and Sons, 605 Third Avenue, New York, NY 10158, 2000.

[22] Goodman, J. *Fourier Optics*. Roberts and Company, Greenwood Village, CO, 3rd edition, 2005.

[23] Halmos, M. "Eyesafe 3D FLASH LADAR for targets under obscuration". volume 5086, 70–83. SPIE, Aug 2003.

[24] Hernandez-Marin, S., A. Wallace, and G. Gibson. "Bayesian Analysis of LIDAR Signals with Multiple Returns". *IEEE Transactions on Pattern Analysis and Machine Intelligence*, 29(12):2170 –2180, Dec. 2007. ISSN 0162-8828.

[25] Jefferies, S., K. Schulze, C. Matson, E. Hege, and K. Stoltenberg. "Imaging through turbid media: post processing using blind deconvolution". *Multifrequency Electronic/Photonic Devices and Systems for Dual-Use Applications*, volume 4490, 282–289. Dec 2001.

[26] Johnson, S. "Effect of target surface orientation on the range precision of laser detection and ranging systems". *Journal of Applied Remote Sensing*, 3:033564, Nov 2009.

[27] Jung, J. and M. Crawford. "A two-stage approach for decomposition of ICESat waveforms". *Proceedings of IEEE International Geoscience and Remote Sensing Symposium*, volume 3, 680–683. July 2008.

[28] Jutzi, B. and U. Stilla. "Range determination with waveform recording laser systems using a Wiener Filter". *ISPRS Journal of Photogrammetry and Remote Sensing*, 61(2):95 – 107, Nov 2006. ISSN 0924-2716.

[29] Karayiannis, N. and A. Venetsanopoulos. "Regularization Theory In Image Restoration: The Regularizing Operator Approach". *Optical Engineering*, 28(7):761–780, July 1989.

[30] Kay, S. *Fundamentals of Statistical Signal Processing: Estimation Theory*, volume 1. Prentice Hall, Upper Saddle River, New Jersey 07458, Jan 2010.

[31] Khoury, J., C. Woods, J. Lorenzo, J. Kierstead, D. Pyburn, and S. Sengupta. "Resolution limits in imaging ladar systems". *Appl. Opt.*, 45(4):697–704, Feb 2006.

[32] Kirchhof, M., B. Jutzi, and U. Stilla. "Iterative processing of laser scanning data by full waveform analysis". *ISPRS Journal of Photogrammetry and Remote Sensing*, 63(1):99 – 114, Jan 2008. ISSN 0924-2716.

[33] Kundur, D. and D. Hatzinakos. "Blind image deconvolution". *Signal Processing Magazine, IEEE*, 13(3):43 –64, May 1996. ISSN 1053-5888.

[34] Kundur, D. and D. Hatzinakos. "Blind image deconvolution revisited". *Signal Processing Magazine, IEEE*, 13(6):61 –63, Nov 1996. ISSN 1053-5888.

[35] Kundur, D. and D. Hatzinakos. "A novel blind deconvolution scheme for image restoration using recursive filtering". *IEEE Transactions on Signal Processing*, 46(2):375 –390, Feb 1998. ISSN 1053-587X.

[36] Kutner, M., C. Nachtsheim, J. Neter, and W. Li. *Applied Linear Statistical Models*. McGraw-Hill Irwin, New York, NY, USA, 5th edition, 2004.

[37] Lam, E. and J. Goodman. "Iterative statistical approach to blind image deconvolution". *J. Opt. Soc. Am. A*, 17(7):1177–1184, July 2000.

[38] Lane, R. and R. Bates. "Automatic multidimensional deconvolution". *J. Opt. Soc. Am. A*, 4(1):180–188, Jan 1987.

[39] Lucy, L. "An iterative technique for the rectification of observed distributions". *The Astronomical Journal*, 79:745+, June 1974. ISSN 00046256.

[40] Ludwig, D., A. Kongable, S. Krywick, H. Albrecht, G. Kamrath, J. Milam, D. Brown, G. Fetzer, and K. Hanna. "Identifying targets under trees: jigsaw 3D LADAR test results". volume 5086, 16–26. SPIE, Aug 2003.

[41] MacDonald, A. *Blind Deconvolution of Anisoplantic Images Collected By A Partially Coherent Imaging System*. Ph.D. thesis, Air Force Institute of Technology, Wright Patterson Air Force Base, June 2006.

[42] MacDonald, A. "Weighted frame averaging for motion compensation of laser radar image data". *Aerospace Conference, 2006 IEEE*, 9 pp. July 2006.

[43] MacDonald, A. and S. Cain. "Parameterized blind deconvolution of laser radar imagery using an anisoplanatic optical transfer function". *Optical Engineering*, 45(11):116001, Nov 2006.

[44] MacDonald, A., S. Cain, and E. Armstrong. "Image restoration techniques for partially coherent 2-D ladar imaging systems". volume 5562, 10–18. SPIE, Oct 2004.

[45] MacManus, Q. *Blind Deconvolution Method of Image Deblurring Using Convergence of Variance*. Master's thesis, Air Force Institute of Technology, Wright Patterson Air Force Base, Mar 2011.

[46] Mallet, C. and F. Bretar. "Full-waveform topographic lidar: State-of-the-art". *ISPRS Journal of Photogrammetry and Remote Sensing*, 64(1):1 – 16, Jan 2009. ISSN 0924-2716.

[47] McMahon, J. *Improving Range Estimation of a 3-Dimensional FLASH LADAR via Blind Deconvolution*. Ph.D. thesis, Air Force Institute of Technology, Wright Patterson Air Force Base, Sep 2010.

[48] McMahon, J., R. Martin, and S. Cain. "Three-dimensional FLASH laser radar range estimation via blind deconvolution". *Journal of Applied Remote Sensing*, 4, Mar 2010.

[49] Millane, R., P. Bones, and H. Jiang. "Blind deconvolution for multidimensional images". *Acoustics, Speech, and Signal Processing, 1994. ICASSP-94., 1994 IEEE International Conference on*, volume v, V/445 –V/448 vol.5. Apr 1994.

[50] Murray, J., S. Moran, N. Roddier, R. Vercillo, R. Bridges, and W. Austin. "Advanced 3D polarimetric flash ladar imaging through foliage." *Proceedings of the SPIE - The International Society for Optical Engineering*, volume 5086, 84 – 95. Lite Cycles Inc., Tucson, AZ, USA, 2003.

[51] Neff, B. and S. Cain. "Image restoration technique for motion-compensated frame averaged data collected by 3D FLASH LADAR imaging system". *Unconventional Imaging and Wavefront Sensing*, volume 8520, 85200L–85200L–9. SPIE, Oct 2012.

[52] Neff, B. and S. Cain. "Multiple surface discrimination in three-dimensional FLASH laser radar while minimizing the effects of diffraction". *Optical Engineering*, 51(5):056201, May 2012.

[53] Neff, B., S. Cain, and R. Martin. "Discrimination of multiple ranges per pixel in 3D FLASH LADAR while minimizing the effects of diffraction". volume 8165, 81650J. SPIE, Sept 2011.

[54] Neilsen, Kevin D. *Signal processing on digitized LADAR waveforms for enhanced resolution on surface edges*. Master's thesis, Utah State University, Logan, Utah, 2011.

[55] Neuenschwander, A., L. Magruder, and R. Gutierrez. "Signal Processing Techniques for Feature Extraction and Classification using Small-Footprint Full-Waveform Airborne LIDAR". *Geoscience and Remote Sensing Symposium, 2008. IGARSS 2008. IEEE International*, volume 3, III –676 –III –679. July 2008.

[56] Oliveira, J., J. Bioucas-Dias, and M. Figueiredo. "Review: Adaptive total variation image deblurring: A majorization-minimization approach". *Signal Process.*, 89(9):1683–1693, Sep 2009. ISSN 0165-1684.

[57] Richardson, W. "Bayesian-Based Iterative Method of Image Restoration". *Journal of the Optical Society of America*, 62(1):55–59, Jan 1972.

[58] Richmond, R. and S. Cain. *Direct-Detection LADAR Systems*, volume TT85. SPIE, 2010.

[59] Roggeman, M. and B. Welsh. *Imaging Through Turbulence*. CRC Press, Boca Raton, Florida 33431, 1996.

[60] Schulz, T. "Multiframe blind deconvolution of astronomical images". *J. Opt. Soc. Am. A*, 10(5):1064–1073, May 1993.

[61] Schulz, T., B. Stribling, and J. Miller. "Multiframe blind deconvolution with real data:imagery of the Hubble Space Telescope". *Opt. Express*, 1(11):355–362, Nov 1997.

[62] Shepp, L. and Y. Vardi. "Maximum Likelihood Reconstruction for Emission Tomography". *IEEE Transactions on Medical Imaging*, 1(2):113 –122, Oct 1982. ISSN 0278-0062.

[63] Stilla, U., W. Yao, and B Jutzi. "Detection of Weak Laser Pulses by Full Waveform Stacking". *Remote Sensing and Spatial Information Sciences*, 36:25–30, Sep 2007.

[64] Stockham, Jr., T., T. Cannon, and R. Ingebretsen. "Blind deconvolution through digital signal processing". *Proceedings of the IEEE*, 63(4):678 – 692, Apr 1975. ISSN 0018-9219.

[65] Thompson, J. and R. Tapia. *Nonparametric Function Estimation, Modeling, and Simulation.* Society for Industrial and Applied Mathematics, Philadelphia, PA, 1990.

[66] Vlassis, N. and A. Likas. "A Greedy EM Algorithm for Gaussian Mixture Learning". *Neural Processing Letters (1370-4621)*, volume 15, 77–87. Feb 2002.

[67] Wolfgang, W., A. Ullrich, V. Ducic, T. Melzer, and N. Studnicka. "Gaussian Decomposition and Calibration of a Novel Small-Footprint Full-Waveform Digitising Airborne Laser Scanner". *ISPRS Journal of Photogrammetry and Remote Sensing (0924-2716)*, volume 60, 100–112. Apr 2006.

[68] Zhang, J., Q. Zhang, and G. He. "Multiframe blind image restoration based on a multiplicative iterative algorithm". *Optical Engineering*, 48(2):027004–027004–4, Feb 2009.

[69] Zhuang, Xinhua, P. Yan Huang, and Yunxin Zhao. "Gaussian mixture density modeling, decomposition, and applications". *IEEE Transactions on Image Processing*, 5(9):1293 –1302, Sep 1996. ISSN 1057-7149.

[70] Zingarelli, J., T. Blake, and S. Cain. "Improving Ground Based Telescope Focus through Joint Parameter Estimation". *Advanced Maui Optical and Space Surveillance Technologies Conference.* AMOSTECH, Sept 2012.

REPORT DOCUMENTATION PAGE

Form Approved
OMB No. 0704–0188

1. REPORT DATE (DD–MM–YYYY)	2. REPORT TYPE	3. DATES COVERED (From — To)
13-06-2013	Doctoral Dissertation	September 2010 – June 2013

4. TITLE AND SUBTITLE

Improving Multiple Surface Range Estimation of a 3-Dimensional FLASH LADAR in the Presence of Atmospheric Turbulence

5a. CONTRACT NUMBER

5b. GRANT NUMBER

5c. PROGRAM ELEMENT NUMBER

6. AUTHOR(S)

Neff, Brian, J., Major, USAF

5d. PROJECT NUMBER

5e. TASK NUMBER

5f. WORK UNIT NUMBER

7. PERFORMING ORGANIZATION NAME(S) AND ADDRESS(ES)

Air Force Institute of Technology
Graduate School of Engineering and Management (AFIT/ENY)
2950 Hobson Way
WPAFB OH 45433-7765

8. PERFORMING ORGANIZATION REPORT NUMBER

AFIT-ENG-DS-13-J-01

9. SPONSORING / MONITORING AGENCY NAME(S) AND ADDRESS(ES)

The Air Force Office of Scientific Research
ATTN: Dr. Kent Miller
875 N Randolph St, Suite 3112
Arlington, VA 22203
Kent.miller@afosr.af.mil

10. SPONSOR/MONITOR'S ACRONYM(S)

AFOSR/NE

11. SPONSOR/MONITOR'S REPORT NUMBER(S)

12. DISTRIBUTION / AVAILABILITY STATEMENT

DISTRIBUTION STATEMENT A: APPROVED FOR PUBLIC RELEASE; DISTRIBUTION UNLIMITED

13. SUPPLEMENTARY NOTES   This material is declared a work of the U.S. Government and is not subject to copyright protection in the United States.

14. ABSTRACT

Laser Radar sensors can be designed to provide two-dimensional and three- dimensional (3-D) images of a scene from a single laser pulse. Currently, there are various data recording and presentation techniques being developed for 3-D sensors. While the technology is still being proven, many applications are being explored and suggested. As technological advancements are coupled with enhanced signal processing algorithms, it is possible that this technology will present exciting new military capabilities for sensor users.

The goal of this work is to develop an algorithm to enhance the utility of 3-D Laser Radar sensors through accurate ranging to multiple surfaces per image pixel while minimizing the effects of diffraction. Via a new 3-D blind deconvolution algorithm, it will be possible to realize numerous enhancements over both traditional Gaussian mixture modeling and single surface range estimation. While traditional Gaussian mixture modeling can effectively model the received pulse, we know that its shape is likely altered due to optical aberrations from the imaging system and the medium through which it is imaging. Simulation examples show that the multi-surface ranging algorithm derived in this work improves range estimation over standard Gaussian mixture modeling and frame-by-frame deconvolution by up to 89% and 85% respectively.

15. SUBJECT TERMS

Laser radar, LADAR, range estimation, image processing, blind deconvolution

16. SECURITY CLASSIFICATION OF:			17. LIMITATION OF ABSTRACT	18. NUMBER OF PAGES	19a. NAME OF RESPONSIBLE PERSON
a. REPORT U	b. ABSTRACT U	c. THIS PAGE U	UU	190	Dr. Stephen C. Cain
					19b. TELEPHONE NUMBER (Include Area Code) (937)255-3636, ext 4716 email: stephen.cain@afit.edu

Standard Form 298 (Rev. 8–98)
Prescribed by ANSI Std. Z39.18